# Efficiency-Limiting Recombination Mechanisms in High-Quality Crystalline Silicon for Solar Cells

by

Simone Bernardini

A Dissertation Presented in Partial Fulfillment
of the Requirements for the Degree
Doctor of Philosophy

Approved August 2018 by the
Graduate Supervisory Committee:

Mariana Bertoni, Chair
Terry Alford
Stuart Bowden
Gianluca Coletti

ARIZONA STATE UNIVERSITY

December 2018

# ABSTRACT

Recent technology advancements in photovoltaics have enabled crystalline silicon (c-Si) solar cells to establish outstanding photoconversion efficiency records. Remarkable progresses in research and development have been made both on the silicon feedstock quality as well as the technology required for surface passivation, the two dominant sources of performance loss via recombination of photo-generated charge carriers within advanced solar cell architectures.

As these two aspects of the solar cell framework improve, the need for a thorough analysis of their respective contribution under varying operation conditions has emerged along with challenges related to the lack of sensitivity of available characterization techniques. The main objective of my thesis work has been to establish a deep understanding of both "intrinsic" and "extrinsic" recombination processes that govern performance in high-quality silicon absorbers. By studying each recombination mechanism as a function of illumination and temperature, I strive to identify the lifetime limiting defects and propose a path to engineer the ultimate silicon solar cell.

This dissertation presents a detailed description of the experimental procedure required to deconvolute surface recombination contributions from bulk recombination contributions when performing lifetime spectroscopy analysis. This work proves that temperature- and injection-dependent lifetime spectroscopy (TIDLS) sensitivity can be extended to impurities concentrations down to $10^9$ $cm^{-3}$, orders of magnitude below any other characterization technique available today. A new method for the analysis of TIDLS data denominated Defect Parameters Contour Mapping (DPCM) is presented with the aim of providing a visual and

intuitive tool to identify the lifetime limiting impurities in silicon material. Surface recombination velocity results are modelled by applying appropriate approaches from literature to our experimentally evaluated data, demonstrating for the first time their capability to interpret temperature-dependent data. In this way, several new results are obtained which solve long disputed aspects of surface passivation mechanisms. Finally, we experimentally evaluate the temperature-dependence of Auger lifetime and its impact on a theoretical intrinsically limited solar cell. These results decisively point to the need for a new Auger lifetime parameterization accounting for its temperature-dependence, which would in turn help understand the ultimate theoretical efficiency limit for a solar cell under real operation conditions.

Questa tesi, così come tutto il lavoro, il tempo ed i sacrifici che mi ci sono voluti per arrivare fino a qui, è dedicata alla mia famiglia: ai miei nonni materni, a mia madre, mio padre, mio fratello, mia sorella e il piccolo Simone.

Si deve perdere tutto per poter ritrovare tutto. Grazie per esserci sempre stati.

ACKNOWLEDGMENTS

First of all, my deepest gratitude goes to my advisor Mariana Bertoni. Not only she has been an extraordinary mentor and an inexhaustible source of ideas for my research throughout my entire PhD, she has also been an inspirational role model and, maybe more importantly than anything else, a friend. There has never been a moment in these five years where I felt I could not rely on her for some guidance and that meant a lot to me, and if any good will ever come out of this work of mine, most of the credit goes to her.

Secondly, I would like to thank all the people at QESST and in particular Christiana Honsberg who started the ASU Solar Power Lab and made it a recognized PV research center worldwide. A huge thank you goes to Bill Dauksher who takes care of the SPL pilot line, without exaggeration almost none of my work would have been possible without him and his infinite patience.

A special thanks goes to my committee and in particular to my former advisor at ECN Gianluca Coletti who not only introduced me to my future boss but also followed me throughout this adventure, his guidance and friendship first showed me what it means to be part of the PV community and made me want to be part of it.

I would also like to thank the people I did not happen to spend a lot of time working with, but whose contribution was fundamental to my research. These are Barry Lai from Argonne National Lab, Steve Johnston from NREL, Ron Sinton and Adrienne Blum from Sinton Instruments.

Finally, I want to thank all my friends I've been so lucky to make in this crazy, illogical, beautiful trip to Arizona I decided to take on a distant day of more than six years ago. Thank

you for all the lunches together, the $5 pitchers of beer, the Tuesday burgers, the stupid nights on Mill, the soccer games, the trips to San Diego and San Francisco. A special shout-out to my European bromigos Aymeric, Pablo, and Andre, you guys are family to me.

And then there is you Mara, I can't even start to say how important you're to me, since the moment we met you simply turned my life upside-down. Because of you, I've been trying to be the best man I could and I'll keep trying every day, this I can promise you.

TABLE OF CONTENTS

Page

CHAPTER Page

CHAPTER Page

LIST OF TABLES

LIST OF FIGURES

Figure Page

Figure Page

Figure Page

Figure Page

Figure Page

Figure Page

Figure Page

Figure Page

Figure Page

Figure Page

Figure Page

Figure Page

Figure Page

# 1 INTRODUCTION

## 1.1 Status of PV in 2018

At the moment this thesis is being written, there are some 7.8 billion people living on Earth [20], with predictions estimating a growth of almost 25% by 2050, when there will be some 9.7 billion people on it [21]. Each human being needs food, water, a shelter, and ultimately, energy. Currently, most of the energy generated to satisfy humankind needs comes from non-renewable sources like coal, nuclear, oil, and natural gas, which are available in limited supplies. Moreover, it has been widely proven, and is now commonly accepted not only by the scientific community, that the consumption of these resources is the main cause of the intense climate changes reported since the mid-20$^{th}$ century, mainly due to the emission of greenhouse gases (see for example Ref. [1]). These conclusions led to the recent Paris conference agreement [22] where most of the governments of the world agreed on achieving a global greenhouse gas emissions reductions before 2030 in order to limit global warming to 2 °C.

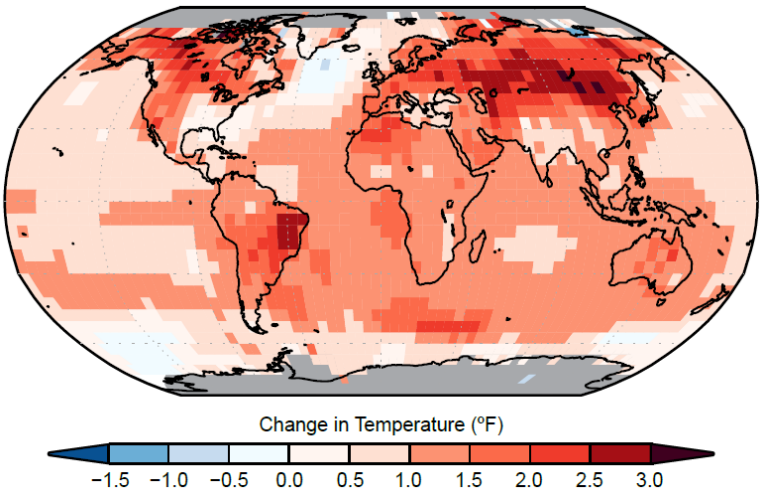


Fig. 1.1 Figure from [1]. Surface temperature change (in °F) for the period 1986-2016 relative to 1901-1930. Grey indicates missing data.

The chances for this goal to be met relies largely on the adoption of renewable sources of energy such as hydro-electric, wind, biomass, geothermal, and others as an alternative to the consumption of non-renewable ones. Among these many options, solar energy represents by far the most abundant and reliable source of energy. The average solar irradiance that reaches the Earth's top atmosphere is 1366W/m$^2$ and provides more than 23000 TW of solar power every year. By comparison, the world annual power consumption is only 16 TW, which gives the scale of this technology potential to satisfy all humankind needs if even just a tiny fraction of this energy can be harvested. A summary of these data, along with the annual power capability of other renewable energy sources, and the overall reserves of non-renewable options is shown in Fig. 1.2.

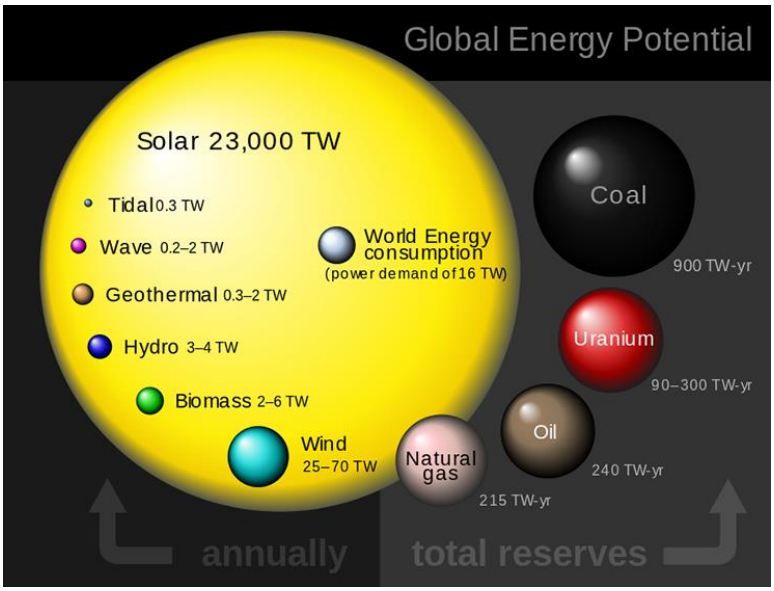


Fig. 1.2 Figure from [2]. The annual power potential of renewable sources of energy along with the world power demand and the overall energy reserve of non-renewable options.

For the last 10 years, the PV industry has shown more than 40% cumulative annual growth rate with more than three times cost reduction. This allowed to reach grid parity in many parts of the world, in particular in regions with a high solar irradiation and high electricity prices. This trend is commonly represented by referring to the Swanson's law which shows that to every doubling of cumulative PV production corresponds a drop of solar photovoltaic modules price by 20% [3]. Fig. 1.3 shows the Swanson's law trend in the last 36 years. However, in the past a significant contribution to this growth has come from state subsidies initially put into PV demand in a number of European countries and later put into PV supply, mainly in China. As these initiatives were only temporary, and considering that the economic and political landscapes are subjected to large fluctuations, the PV industry needs to reach grid parity in most electricity markets in order to sustain a similar growth in the next ten years without relying on state stimuli.

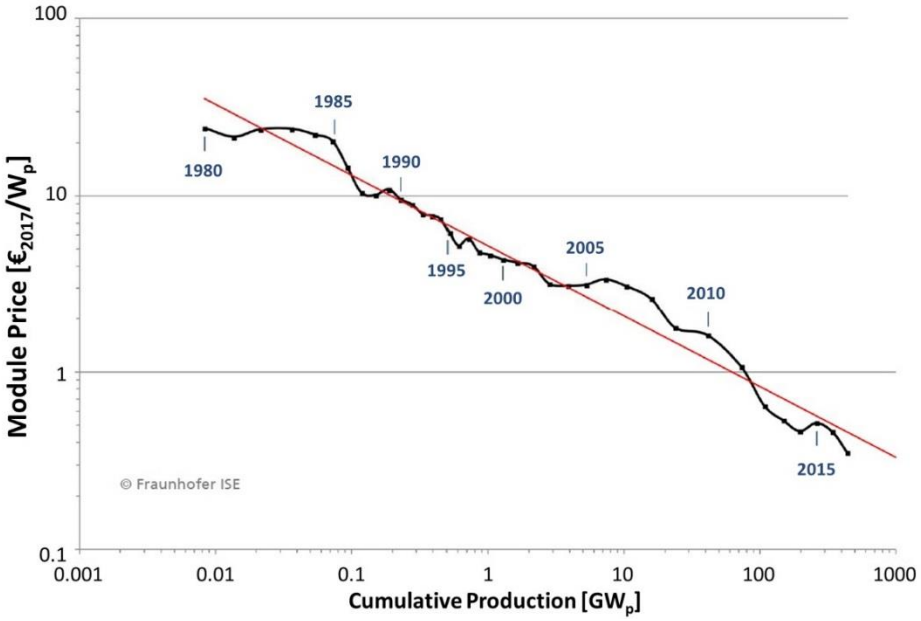


Fig. 1.3 Figure from [3]. Drop of solar photovoltaic modules price with increasing cumulative production up to 2017.

To help understand how this can be achieved, let's look into a parameter called Levelized Cost of Electricity (LCOE), which helps estimate the cost of PV electricity through the entire lifetime of a module and compare it to the cost of electricity generated by other technologies. LCOE is calculated using the following equation

$$LCOE = \frac{(\$/m_{PV}^2 + \$/m_{BOS}^2)}{\eta \cdot S} x\ FinancingCost \quad (1)$$

where $\eta$ is the module efficiency through time and $S$ is the annual incident solar radiation. From Eq. 1 it is clear that the competitiveness of PV energy can be achieved directly in two different ways: reducing the PV module costs or increasing its photoconversion efficiency.

The price of a PV system includes much more than just the raw materials and energy costs to produce the module. Typically, about 50% of a system cost is related to component

and installation requirements such as inverters, cabling, mounting structures, and labor, whereas the PV module accounts for ~ 20 – 40% of the system cost, depending on the scale of the installation. Figure 1.4 shows the average cost in US$/$W_{dc}$ of PV systems between July and September 2015 for residential, commercial, and utility-scale PV systems taken from Ref. [4]. These prices are also separated by the cost of each system component. Because the cost of the PV module does not vary depending on the size of the installed system, advances in cell/module efficiency and decreases in production costs, lead to lower balance of system cost, which normally scales with area.

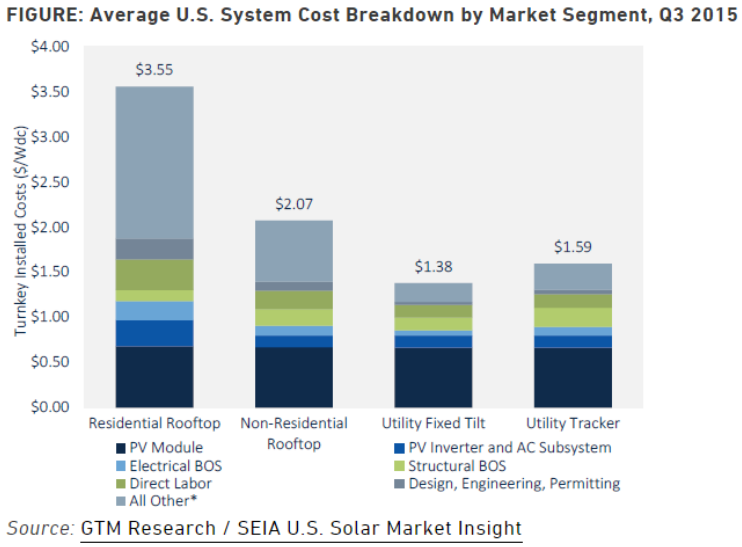


Fig. 1.4 The turn-key installed cost of rooftop, commercial, and utility-scale PV systems, normalized to the rated power ($W_{dc}$) of the system from [4]. The height of each bar is normalized system cost, with each sub-bar corresponding to a system component.

For this reason it has been shown that increasing the module efficiency has the largest impact on reducing system cost ($/$W_p$) as a higher cell efficiency directly translates into a smaller and therefore less expensive PV system [23].

Nowadays, Si-wafer based technology accounts for about 94% of the total PV annual production with multi-crystalline Si being by far the most common technology with a 70% share of the total production [24]. There are many technological reasons why silicon is still such a good alternative for PV applications. Among others, silicon is the second most abundant element in the Earth's crust, it is non-toxic, it has a nearly optimum bandgap for sunlight absorption, it can be doped both *n*- and *p*-type, and it forms a naturally passivating and chemically robust surface oxide inhibiting bulk material degradation. Silicon PV's also benefit from a long development history and sustained improvement that started over 60 years ago with the first modern c-Si solar cell [25]. While Si-based solar cells technology has been so far dominated by an aluminum back surface field (Al-BSF) architecture, the latest international technology roadmap for photovoltaic (ITRPV) report suggests that Passivated Emitter and Rear Cell (PERC) is becoming the new standard (see Fig. 1.5). Thus, shifting the mainstream architecture to a high-efficiency solar cell technologies driven by the need to reduce the LCOE for PV-generated electricity.

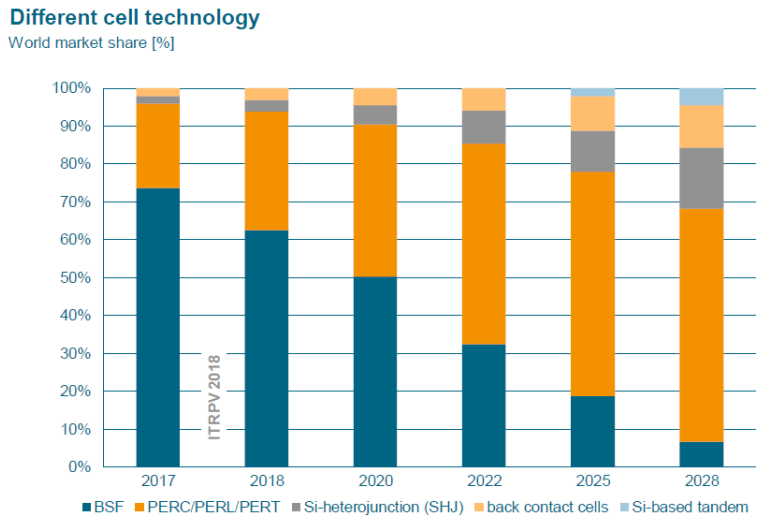


Fig. 1.5 From [5]. Cell technologies market share trend over the next 10 years. The report predicts an increase of PERC/PERL/PERT solar cells world market share and their establishment as the new standard architecture.

The same report highlights how the shift towards high-performance solar cell architectures will be accompanied by the increment of high-quality material such as *p*-type high-performance (HP) mc-Si and *p*- and *n*-type mono-Si market share (see Fig. 1.6).

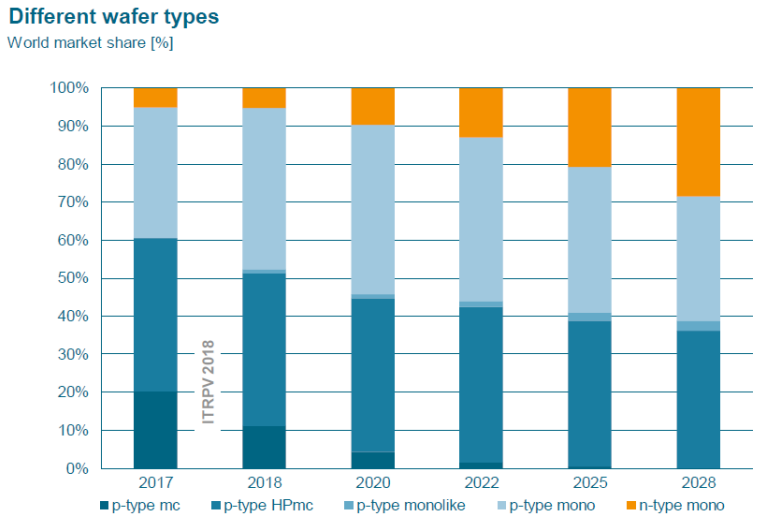


Fig. 1.6 From [5]. Wafer types market share trend over the next 10 years. The report predicts an increment of high-quality *n*-type mono crystalline Si world market share in the next decade with at the same time the disappearing of *p*-type mc-Si technology.

Remarkably, the report does not foresee a strong shift towards *n*-type material up to 2028 but rather the coexistence of high-quality *p*- and *n*-type monocrystalline silicon mainly due to the tremendous progress in stabilizing *p*-type mono against the well-known light induced degradation (LID) mechanism [26].

As seen in Fig. 1.5, PERC architecture is not the only high-performance cell technology expected to gain relevance in the market share over the next 10 years; heterojunction (HIT) cells are expected to hit a market size of 10% in 2024 and 15% in 2028. Surprisingly, the market trends show silicon as an important player beyond single-junction technology with Si-

based tandem cells expected to appear in mass production after 2019. Interestingly, the report does not account for the possible merging of different advanced technologies such as the efficiency record HIT/IBC c-Si solar cell recently developed by Kaneka, which hit an astonishing photoconversion efficiency of 26.6% [27], very close to the estimated practical limit value of 27.1% [28].

In the last few years the solar community has witnessed a significant number of records being established and then swiftly surpassed, from photoconversion efficiency to annual installed capacity and electricity generation. The reductions of LCOE registered in the last decade make the U.S. DOE targets for 2030 of US$0.03/kW·h for fix tilt utility-scale PV seem reachable [29]. For these reasons, despite the many challenges still to be addressed in the future, photovoltaic technology is today the most promising alternative to revamp the aging energy system and provide clean and sustainable power to future generations.

## 1.2 Solar Cell Structure

A solar cell is an electronic device which directly converts the sunlight hitting its surface into electricity, a process denominated photoconversion. Light shining on the solar cell produces both a current and a voltage to generate electric power. The fundamental operation of a solar cell relies on the material absorbing the incoming photons of different energy and raising an electron to a higher energy state across the band gap. This process happens in the "base" or "absorber layer" of the solar cell which, in most cases, is made of silicon (Si). After absorption of light, the key is to collect this electron ($e^-$) - along with the hole ($h^+$) left behind - through electric contacts placed at opposite surfaces of the device. Here, the electron and

the hole, from now on referred to as the excess charge carriers, can enter an external circuit where they dissipate their energy on an external load before returning to the solar cell. Figure 1.7 shows the fundamental components of the most common *p-n* junction solar cell.

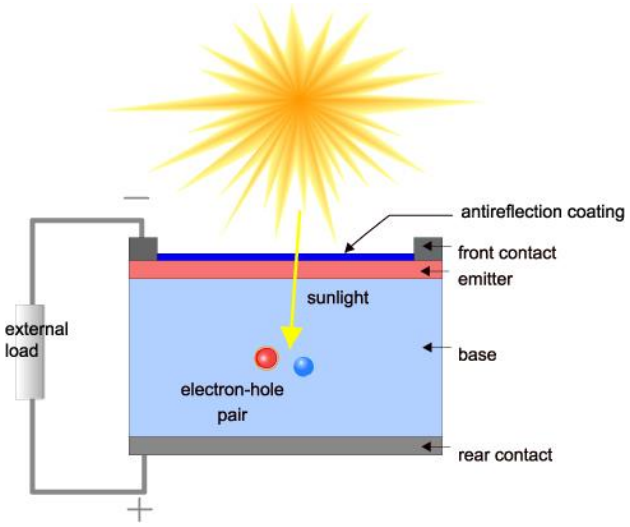


Fig. 1.7 Image from [6]. Schematic representation of a solar cell with its fundamental components. Sunlight hits the device surface generating an electron-hole pair in the base of the solar cell. The two charge carriers are then collected at the opposite sides of the device and move through an external circuit where they dissipate their energy before returning to the solar cell.

These components are:

- An absorber layer;
- An emitter layer;
- Passivation/antireflection layer;
- Front/rear contacts.

As mentioned before, the key to high efficiency relies on collecting the excess charge carriers before a process of recombination occurs. In this case, in fact, the energy is dissipated in the device and does not contribute to the generation of power. According to the region of the solar cell where the recombination occurs, the process can be classified as

surface recombination, bulk recombination, or depletion region recombination. In all cases, the result is a loss of the photogenerated charge carriers and a reduced device photoconversion performance. In order to avoid these recombination losses to occur, several strategies can be adopted which are specifically tailored to the affected regions of the device. More details about the different recombination mechanisms occurring in a solar cell and how they can be mitigated are provided in the Chapter 2.

## 1.3 Motivation and Impact

### 1.3.1 Assessing Recombination in Operando

As previously discussed in Section 1.1, the PV industry needs to further improve the module efficiency as this has the largest impact on reducing system cost ($/$W_p$), and a higher cell efficiency directly translates into a smaller and therefore less expensive PV system. In a market as competitive as the market of energy, where solar power has to compete with a set of well-established competitors, is thus fundamental to rigorously assess the performance of a solar system once it is deployed on the field as environmental conditions such as illumination and temperature can be significantly different from the controlled environment of a research lab [30]. In fact, it is important to notice that all the solar cells' and modules' efficiency reported in literature refer to devices certified under standard testing conditions (STC, 1000 W/m$^2$, 25 ºC, AM1.5 g spectrum).

Photovoltaic devices are known to show significant performance losses with increasing *T* due to a number of different processes, some known to be reversible whereas others found to be irreversible. The reversible processes are generally described by the temperature

coefficient of the conversion efficiency ($TC_\eta$), which represents an important figure-of-merit for the energy yield of a given PV system under different operation temperatures [31]. In particular, some cell technologies are significantly more sensitive than others: silicon heterojunction (SHJ) solar cells are, for example, have a $TC_\eta$ in the range of -0.23 – -0.1%/ ºC [32], [33] which means they are much less sensitive to increasing operation temperatures than conventional crystalline silicon homojunction ($TC_\eta$ = -0.45%/ ºC for standard homojunction and $TC_\eta$ = -0.35%/ ºC for homojunctions with passivating contacts [34]). Furthermore, the solar spectrum and intensity change during the day and vary greatly with the time of the year. As a result, solar cells rarely operate under conditions comparable to the STC. Exposure to high temperatures also results into some irreversible degradation processes both at the module level, such as encapsulant delamination and discoloration [35], and at the solar cell level, such as the recently reported degradation affecting SHJ technology: such mechanism is found to mostly affect the $V_{OC}$ of the system in the first two years of open-field operation and is likely correlated to a degradation of the passivation quality provided by the intrinsic amorphous silicon layer. For all these reasons, a thorough understanding of the temperature- and injection-dependence of the mechanisms limiting the photoconversion efficiency of a solar cell is required.

The goal of this dissertation is to present a framework and thoroughly understand the most relevant recombination mechanisms, both intrinsic and extrinsic, happening in the bulk, interface, and surface of a high-efficiency solar cell and evaluate their impact throughout a broad range of temperatures and injection levels. It's important to notice, in fact, that the interplay among different recombination paths is usually overlooked in literature as the

quality of the surface passivation is considered good enough to validate the simple assumption $\tau_{eff} = \tau_{bulk}$. However, as exemplified in Fig. 1.8, for high quality Si material with bulk lifetime above 1 ms, the error in making this assumption rapidly approaches 50% of the initial lifetime value even for a good surface recombination velocity below 10 cm/s.

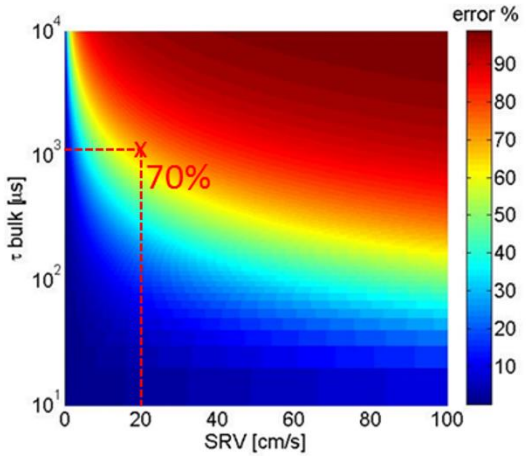


Fig. 1.8 Error percentage obtained when assuming $\tau_{eff}$ equivalent to $\tau_{bulk}$ as a function of the surface recombination velocity and bulk lifetime. The red cross indicates the case for $\tau_{bulk}$ = 1 ms and SRV = 20 cm/s for which the error in making the $\tau_{eff} = \tau_{bulk}$ assumption is 70%.

As an example, in Fig. 1.8 we highlighted the case for a Si substrate with $\tau_{bulk}$ = 1 ms. As indicated by the cross placed on the picture, with a SRV of only 20 cm/s the error in making the $\tau_{eff} = \tau_{bulk}$ is already up to 70%.

This analysis will not just provide in-depth knowledge about the limits imposed by these recombination paths on the final device performance, but will also give access to critical information not easily accessed by the most common characterization techniques, such as the variation with temperature of the surface passivation quality, or the defect concentration for high-quality float-zone (FZ) Si material.

### 1.3.2 Impact

This dissertation demonstrates how to accurately discriminate among the recombination mechanisms happening in the bulk and at the surface of silicon samples. The analysis is carried out for the first time in a broad range of experimental conditions to demonstrate how measuring the samples exclusively at STC is not sufficient for an adequate understanding of the recombination mechanisms' roots. By deconvolution of the surface recombination from the bulk recombination, we prove that temperature- and injection-dependent lifetime spectroscopy (TIDLS) sensitivity can be extended to detect impurities concentrations down to $10^9$ $cm^{-3}$, which is orders of magnitude below any other characterization technique available today. We introduce a new method for the analysis of TIDLS data denominated Defect Parameters Contour Mapping (DPCM) with the aim of providing a visual and intuitive tool to identify the possible lifetime limiting impurities in silicon material. In this work, we also make use of several approaches presented in literature to model the experimentally evaluated SRV and demonstrate for the first time that they successfully apply to temperature-dependent data. In this way, several new results are presented, which help clarifying long disputed aspects of surface passivation mechanisms. Finally, we experimentally evaluate for the first time the temperature-dependence of Auger lifetime and demonstrate that its recombination mechanism is an energy-activated process. These results decisively point at the need for a new Auger lifetime parameterization accounting for its temperature-dependence, which would in turn help understand the ultimate theoretical efficiency limit for a solar cell under real operation conditions.

This thesis is structured in the following way: Chapter 2 describes the different recombination mechanisms occurring in a solar cell. Chapter 3 describes the materials and the processing steps required to generate the solar cell specimens used in the analysis presented in the following chapters. Chapter 4 presents a list of the characterization techniques with a discussion of their basic theory and application. Chapter 5 is devoted to the analysis of the surface passivation obtained with several coating layers. Chapter 6 describes the results related to the bulk of the silicon material and introduces the Defect Parameters Contour Mapping method for analysis of TIDLS data. Chapter 7 presents the experimentally evaluated Auger lifetime temperature-dependence and its impact on a theoretical intrinsic recombination-limited solar cell.

# 2 RECOMBINATION MECHANISMS IN SEMICONDUCTORS

For crystalline silicon, the recombination of excess charge carriers occurs mainly via four recombination paths. It's important to note that all these recombination processes can potentially occur at the same time in the device and simultaneously contribute to the reduction of photogenerated electron-hole pairs. A distinction has to be made among "intrinsic" processes, i.e. Auger and radiative band-to-band recombination mechanisms, which cannot be mitigated by the optimization of the material quality and processing steps, and "extrinsic" processes, i.e. defect-assisted Shockley-Read-Hall (SRH) recombination in the bulk and at the surface. The former, for example, can be greatly reduced by controlling the introduction of impurities in the silicon ingot during the crystallization process or by additional processing steps, such as a gettering step. The latter is generally reduced via the deposition of a surface passivation layer which deactivates the recombination-active defects due to the disruption of the material crystallinity. Reducing the extrinsic recombination rate is one of the major challenges for the engineering of a solar cell.

The different recombination mechanisms are characterized by their average charge carriers' lifetime ($\tau$), which is the average time spent by an electron (hole) in the conduction (valence) band before it is annihilated by recombination. By definition, lifetime is the ratio of excess charge carrier density ($\Delta n$) and the net recombination rate ($R$)

$$\tau = \frac{\Delta n}{R} \tag{2}$$

assuming the density of excess electrons and holes being equal $\Delta p = \Delta n$.

As all the recombination mechanisms happen simultaneously, the experimentally determined lifetime is influenced by all processes at once. This lifetime is referred to as average effective lifetime ($\tau_{eff}$) and is expressed by the sum of the reciprocal of each individual lifetime $\tau_i$

$$\frac{1}{\tau_{eff}} = \sum_i \frac{1}{\tau_i} \tag{3}$$

## 2.1 Radiative Band-to-Band Recombination

Radiative band-to-band recombination is essentially the invers process of photon absorption in which the energy of an electron-hole pair is lost as a photon of the same energy. Since one electron and one hole need to be involved, the recombination rate ($R_{rad}$) is proportional to the density of the free holes times free electrons

$$R_{rad} = B(pn - p_0 n_0) = B(pn - n_i) \tag{4}$$

where $B$ is the coefficient of radiative recombination which depends on the band-to-band transition absorption coefficient, the photon energy, and temperature, $p{\cdot}n = (p_0 + \Delta p){\cdot}(n_0 + \Delta n)$, where $p_0$ and $n_0$ are the hole and electron density in thermal equilibrium, respectively, and $n_i$ is the intrinsic carrier density. The corresponding lifetime is obtained by applying the general Eq. 2 to the radiative recombination rate expressed in Eq. 4 and by assuming $\Delta n = \Delta p$

$$\tau_{rad} = \frac{\Delta n}{R_{rad}} = \frac{\Delta n}{B\big((p_0 + \Delta n) + (n_0 + \Delta n) - p_0 n_0\big)} = \frac{1}{B(p_0 + n_0) + B\,\Delta n} \tag{5}$$

Radiative recombination is usually very low for most terrestrial solar cells as they are made out of silicon, which is an *indirect* bandgap semiconductor ($B_{rad}$ = 4 - 5 x $10^{-15}$ $cm^2/s$). In this case, a phonon needs to be involved in the recombination process which makes it less likely to happen compared to the recombination mechanisms discussed in the following sections. For this reason, irrespective of the injection conditions, for crystalline silicon $\tau_{rad}$ is rather large and does not limit the overall lifetime. On the contrary, for direct bandgap materials such as InAs and GaAs, $B_{rad}$ is orders of magnitudes larger, i.e., $10^{-11}$ $cm^2/s$ and $10^{-10}$ $cm^2/s$ respectively, and leads to significant recombination losses at all injection conditions.

## 2.2 Band-to-Band Auger Recombination

For crystalline silicon, Auger recombination is the most relevant intrinsic recombination mechanism. The process involves three carriers, i.e., two electrons and one hole, or one electron and two holes. When the electron and the hole recombine, the resulting energy rather than being emitted, is transferred to a third particle which then thermalizes back down to the minimum of the related energy band, i.e., conduction band if it is an electron, and valence band if it is a hole. In the first case the recombination rate is indicated as $R_{eeh}$, whereas in the second case it is indicated as $R_{ehh}$. The need for a third particle to be present, makes Auger recombination more likely at high carrier densities, e.g., in highly doped material or high injection conditions.

The net Auger recombination rate ($R_{Auger}$) is the sum of both processes which are proportional to the carrier densities involved

$$R_{Auger} = R_{eeh} + R_{ehh} = C_p(p^2 n - n_i^2 p_0) + C_n(pn^2 - n_i^2 n_0) \quad (6)$$

where $C_n$ and $C_p$ are the electron and hole Auger coefficients, respectively. The Auger lifetime can be approximated for low injection conditions, i.e., assuming $\Delta n << N_{dop}$, as

$$\tau_{Auger,li} = \frac{1}{C_n N_{dop}^2} \tag{7}$$

and for high injection conditions, i.e., assuming $\Delta n >> N_{dop}$, as

$$\tau_{Auger,hi} = \frac{1}{(C_p + C_n)\Delta n^2} \tag{8}$$

It follows that for low injection conditions $\tau_{Auger}$ strongly depends on the doping of the material, and for high injection conditions it depends heavily on the excess carrier density. Figure 2.1 shows that for silicon-based devices, when other recombination paths are reduced, Auger recombination mechanism represents the ultimate limit to solar cell efficiency. In particular, as the effective recombination velocity at the rear of the device (represented on the *x*-axis) is reduced from 1000 cm/s to 1cm/s, the contribution given to the overall recombination current density at maximum power point (represented on the *y*-axis) by Auger recombination reaches almost half of the total, more than any other recombination mechanisms. Thus, as other recombination mechanisms are reduced or eliminated the Auger recombination becomes dominant and represent the ultimate limit for high-efficiency solar cells.

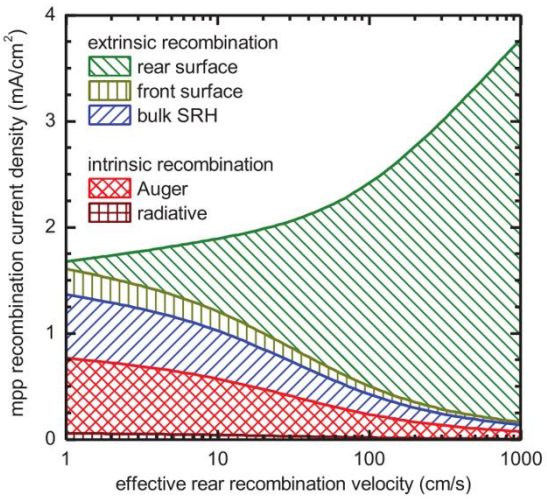


Fig. 2.1 Image from [7]. Recombination current density at the maximum power point (mpp) as a function of the effective rear recombination velocity. The data was simulated using PC1D for an *n*-type silicon solar cell with 150 μm thick, 1 Ωcm *n*-type silicon base and a shallow industrial boron-doped front side emitter.

## 2.3 Defect Recombination in the Bulk

Bulk lifetime is the most immediate and commonly referred to figure of merit for a quick assessment of any silicon material quality used for photovoltaic applications. It is the result of several recombination mechanisms happening simultaneously in the material and can be expressed as a convolution of several terms according to the equation

$$\frac{1}{\tau_{bulk}} = \frac{1}{\tau_{SRH}} + \frac{1}{\tau_{Auger}} + \frac{1}{\tau_{rad}} = \frac{1}{\tau_{SRH}} + \frac{1}{\tau_{int}} \tag{9}$$

where $\tau_{SRH}$ is the Shockley-Read-Hall lifetime, $\tau_{Auger}$ is the Auger lifetime, $\tau_{rad}$ is the radiative lifetime and $\tau_{int}$ is the intrinsic lifetime which is given by the inverse sum of the last two terms.

Equation 9 reveals the different recombination mechanisms that happen within the bulk of the material. As discussed in Chapter 2, a distinction has to be made among “intrinsic” processes, i.e. Auger and radiative recombination mechanisms, which cannot be mitigated by the optimization of the material quality and processing steps, and “extrinsic” processes, i.e. defect-assisted SRH recombination in the bulk and at surfaces, which can be greatly reduced by controlling the introduction of impurities in the silicon ingot during the crystallization process or by additional steps, usually involving high temperature conditions, such as a gettering step. The different recombination mechanisms are represented in Fig. 2.2

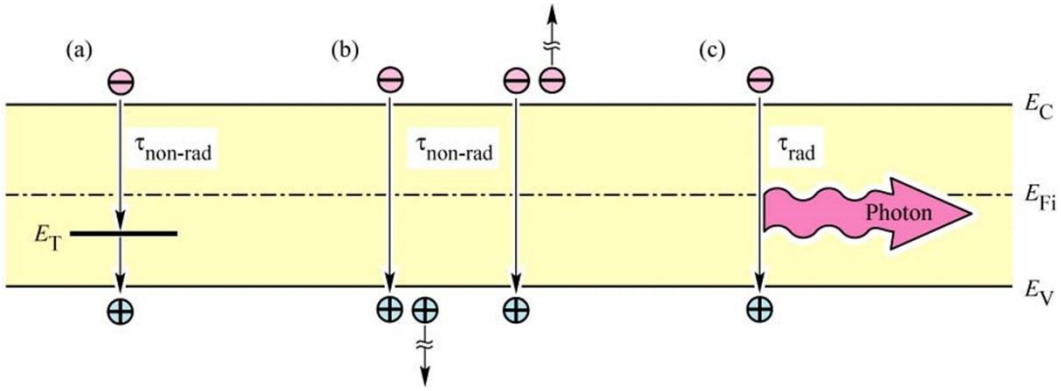


Fig. 2.2 Different recombination mechanisms happening in the bulk of Si material. a) Shockley-Read-Hall recombination; b) Auger recombination; c) radiative recombination.

The impact of each recombination mechanism on the final bulk lifetime can better be seen in Fig. 2.3. It’s immediately apparent that different recombination mechanisms dominate the bulk lifetime in different injection regimes, e.g., SRH in the low injection regime and Auger in the high injection one.

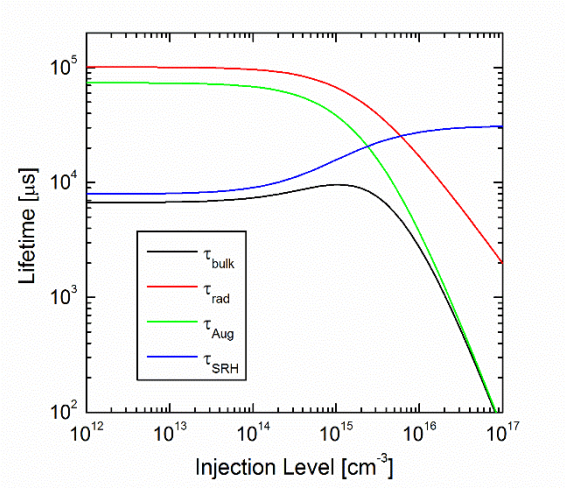


Fig. 2.3 Contribution of all the recombination mechanisms happening in the bulk of the samples to the final $\tau_{bulk}$.

Defect recombination is caused by defects states within the bandgap of the material introduced by impurities or lattice defects. On the contrary of the intrinsic recombination mechanisms presented above, for which several parameterizations have been proposed based solely on the empirical analysis of the many experimental results presented in literature, defect recombination is based on the well-established Shockley-Read-Hall (SRH) theory [36], [37] of carrier generation and recombination at a single defect level with energy $E_t$. The net recombination rate for a single defect is expressed according to the equation

$$R_{SRH} = \frac{pn - n_i^2}{\tau_{n0}(p_0 + p_1 + \Delta n) + \tau_{p0}(n_0 + n_1 + \Delta n)} \tag{10}$$

where $\tau_{n0}$ and $\tau_{p0}$ are the capture time constants and $n_0$ and $p_0$ the equilibrium densities of electrons and holes, respectively. If trapping is assumed to be negligible, the excess carrier densities of electrons and holes can be considered equal ($\Delta n = \Delta p$). Finally, the so-called SRH densities $n_1$ and $p_1$ are given by

$$n_1 = N_C exp\left(-\frac{E_C - E_t}{kT}\right), \quad p_1 = N_V exp\left(-\frac{E_t - E_V}{kT}\right) \tag{11}$$

where $E_t$ is the energy level of the defect, or recombination center, within the material band gap, $E_C$ and $E_V$ are the energies of the conduction and the valence band edge, respectively, and $N_C$ and $N_V$ are the effective densities of states in the conduction and the valence band [38], respectively.

The time constants $\tau_{n0}$ and $\tau_{p0}$ for the capture of electrons and holes in the defect state are proportional to the inverse product of the defect concentration $N_t$ and the capture cross sections $\sigma_n$ and $\sigma_p$ for electrons and holes:

$$\tau_{p0} = \left(N_t \sigma_p v_{th}\right)^{-1}, \quad \tau_{n0} = (N_t \sigma_n v_{th})^{-1} \tag{12}$$

where $v_{th}$ is the thermal velocity for either electrons or holes. The other fundamental parameter of an impurity defect level is the capture cross section ratio $k$ defined by the equation

$$k \equiv \frac{\sigma_n}{\sigma_p} = \frac{\tau_{p0}}{\tau_{n0}} \tag{13}$$

The corresponding SRH lifetime is expressed by the equation

$$\tau_{SRH} = \frac{\tau_{n0}(p_0 + p_1 + \Delta n) + \tau_{p0}(n_0 + n_1 + \Delta n)}{p_0 + n_0 + \Delta n} \tag{14}$$

## 2.4 Defect Recombination at the Surface

The surface of a crystalline silicon wafer represents a region of high recombination as the continuity of the crystal lattice is disrupted and Si atoms are only bonded to two other atoms in the bulk rather than four as shown in Fig. 2.4.

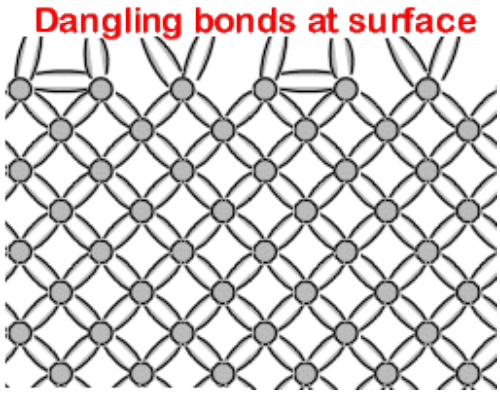


Fig. 2.4 Figure from [8]. Silicon dangling bonds at the surface of crystalline Si. The atoms at the surface are bonded only to two atoms from the bulk instead of four.

This disruption leads to the formation of dangling bonds (DBs) at the surface which introduce a large density of surface states continuously distributed over the band gap. Under these conditions, the annihilation of excess carriers by recombination is very efficient and the surface actively acts as a sink for the excess carriers causing a hole and electron current to flow into this region of the solar cell. As a localized region of low carrier concentration causes carriers to flow into this region from the surrounding, higher concentration regions, the surface recombination rate is limited by the rate at which minority carriers move towards the surface. A parameter called the “surface recombination velocity” and expressed in cm/s is thus used to specify the recombination at a surface.

Similarly to the recombination via a defect level in the bulk, the recombination rate at the surface can be expressed by SRH statistics. However, in this case instead of a localized defect level in the bandgap as for recombination in the bulk, we have a large distribution of defect states spread over the band gap. The recombination rate is then expressed as an integral according to the equation

$$R_S = v_{th}(p_s n_s - n_i^2) \int_{E_v}^{E_c} \frac{D_{it}(E)dE}{\frac{[n_s+n_1(E)]}{\sigma_p} + \frac{[p_s+p_1(E)]}{\sigma_n}} \tag{15}$$

Where $D_{it}$ is the energy dependent interface defect density, $n_i$ is the Si intrinsic carrier density [38], [39], $v_{th}$ is the thermal velocity of both types of carriers, $\sigma_p$ ($\sigma_n$) are the capture cross sections for holes (electrons), $n_s$ and $p_s$ are the carrier concentrations at the surface, respectively.

As previously noted, surface recombination is usually not expressed in terms of lifetime as for the other recombination mechanisms. Instead, it is usually calculated according to the equation

$$SRV \equiv \frac{R_s}{\Delta n} = \frac{1}{\Delta n} \int_{E_v}^{E_c} \frac{(n_s p_s - n_i^2)}{\frac{[n_{tot}(E)]}{S_p} + \frac{[p_{tot}(E)]}{S_n}} dE \tag{16}$$

where $n_{tot}$ ($p_{tot}$) is the total density of electrons (holes) at the interface, and $S_p$ and $S_n$ are the energy dependent SRV for holes and electrons, respectively.

# 3 MATERIAL PROCESSING

The material analyzed in this work was processed either at Arizona State University (ASU) or at the University of New South Wales (UNSW). At ASU, all the processing steps required for the preparation of the samples with the exception of the annealing steps and the $AlO_x$ depositions were carried out in a Class 10,000 clean room located at the ASU Solar Power Laboratory (SPL). The annealing steps were performed in a muffle furnace located in the defect engineering for energy conversion technologies (DEfECT) laboratory whereas the $AlO_x$ depositions were carried out in the ASU Nanofab laboratory, both located in the Engineering Research Building in the ASU campus. The clean room at SPL provides controlled ambient conditions, a temperature value set at 19 °C and a constant humidity level of 42%. The latter is particularly relevant for the samples processing as a variation of humidity could influence the re-oxidation of H-terminated wafers in the time lag between rinsing and drying of the samples after BOE etch and moving them into the deposition chamber.

At UNSW, the material was processed in the solar industrial research facility (SIRF) located on campus, which includes a state-of-the-art silicon solar cell production line and laboratories for developing and demonstrating industrial scale advanced technologies.

## 3.1 Silicon Substrates

All the substrates used in this work were high-quality float zone (FZ) *p*- and *n*-type c-Si Topsil wafers with a resistivity of 2.8 – 3.0 ohm-cm. The wafers were 4 inches round with a <100> surface orientation. In order to create the samples required for this study, each wafer

was cleaved into two tokens of about 2 inches-long. The size and shape of the resulting tokens were chosen to ease the handling during the subsequent wet processing. A schematic of the samples shape resulting from the cleaving of each wafer is shown in Fig. 3.1.

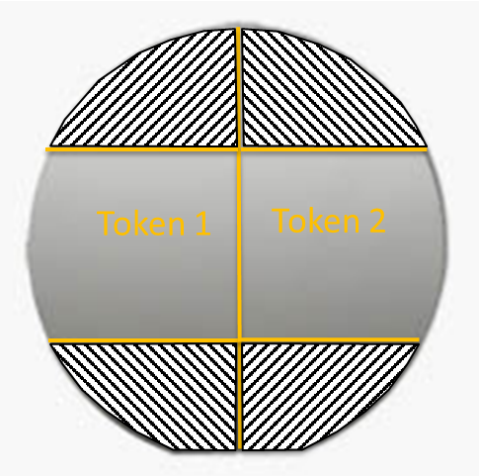


Fig. 3.1 Schematic of the two tokens obtained from each wafer after cleaving. The dimensions and shape of the tokens were chosen in order to facilitate the handling during the subsequent chemical treatments and limit the breakages.

Thanks to their round side, the samples could be easily placed into a 2'' round plastic cassette as shown in Fig. 3.2.

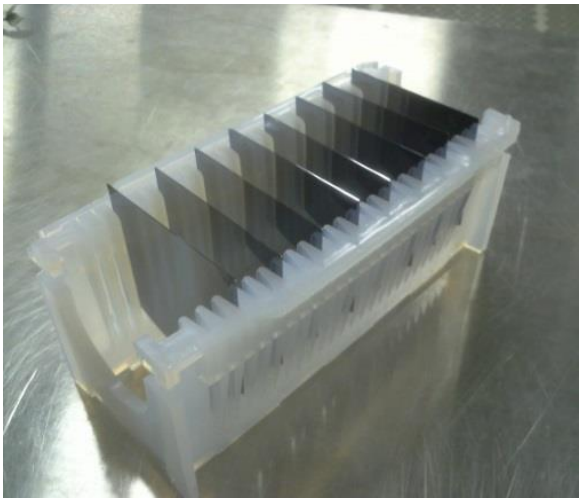

Fig. 3.2 Samples obtained from cleaving of a 4" round wafer positioned in a 2" plastic round cassette.

### 3.2 Samples Cleaning and Etching

Before deposition of dielectric layers, samples were chemically processed following a sequence of wet chemical treatments to both clean the surfaces and reduce the material thickness to the desired values. The chemical solutions used in this work are reported in Table 3.2.

Table 3.2 List of recipes used for wet chemical processing in this work.

| | Purpose | Mixture | Temperature and time |
|---|---|---|---|
| Piranha | Organic clean | 4:1, $H_2SO_4$:$H_2O_2$ | 110 °C, 15 min |
| RCA-b | Ionic clean | 1:1:6, HCl:$H_2O_2$:$H_2O$ | 75 °C, 10 min |
| BOE | Oxide etch, H termination | 10:1, $H_2O_2$:HF with small addition of $NH_4F$ | 19 °C, 1 min |
| Diluted HNA | Etching | 10:75:20, HF:$HNO_3$:$CH_3COOH$ | 19 °C, variable |

The surface cleaning procedure was thoroughly evaluated and optimized in order to consistently provide the highest level of cleanliness. The process flow is displayed in Fig. 3.3.


Fig. 3.3 Process flow performed on samples before deposition of dielectric layer.

During our analysis, we realized that the standard operating procedure commonly followed by the SPL users to maintain the wet baths free of contaminants did not provide the required level of cleanliness necessary for the high sensitivity analysis of surface recombination velocity performed in this work. Thus, we revisited the protocol as follow:

- All chemical hoods with the baths were decontaminated prior to being used at Solar Power Lab.
- Only semiconductor grade chemicals were used. The chemicals were refreshed and the tanks rinsed before every usage with the exception of BOE solution that was replaced every month.
- Piranha and RCA-b were spiked with $H_2O_2$ after few hours from their generation to keep their activity level constant.
- HNA was replaced during the process whenever the solution started to show a decrease of effectiveness reflected by a reduction in etching rate (μm/sec).
- The baths and rinse tanks were dedicated to one particular process or chemical.
- All wet treatments were followed by a 10 min DI water rinse.

Figure 3.4 shows the chemical hoods and process followed.

### 3.3 Dielectric Layers Deposition

Electronic passivation of semiconductor interfaces is of critical importance in the performance of many electronic and photonic devices. For solar cells in particular, surface passivation helps to prevent unwanted recombination of photogenerated electron-hole pairs and is thus a key requirement to achieve high voltages and high conversion efficiencies.

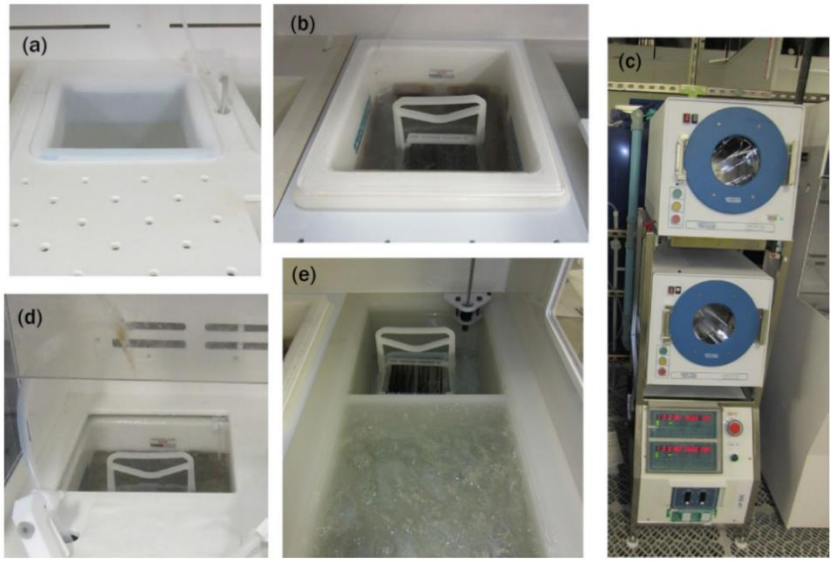


Fig. 3.4 Equipment in the SPL laboratory. a) a Teflon bath for BOE, b) a quartz tank for RCA-b oxidation, c) spin rinse dryers, d) a quartz tank for Piranha clean, e) plastic tanks for DI water rinse.

As it will be shown in the following sections, when the quality of silicon bulk increases or the thickness of the wafer is reduced, the surface passivation of the substrates gains more and more importance. Equation 16 shows that there are two complementary ways of reducing surface recombination. The first one is to reduce the rate by which surface states capture charge carriers, i.e., electrons and holes, either by having fewer states or lower capture probabilities. This can be achieved by using a surface dielectric material which introduces some chemical species – usually hydrogen – to form bonds with the surface silicon atoms. This mechanism is usually referred to as "chemical" passivation. The second method, aims at reducing the presence of one charge carrier species at the surface as a recombination process requires the simultaneous presence of both of them. This reduction can be achieved by using a coating material with some fixed charges in it which establish an electric field that penetrates the semiconductor surface and yields to the bands bending at the interface, thus

modifying the surface charge carriers' concentration. This mechanism is referred to as "field-effect" passivation.

Over the last decades, several passivation technologies have been developed as an alternative to the widely used $SiO_2$; this was an attempt to eliminate the high-temperature step needed for its activation, which is known to degrade the bulk lifetime of silicon samples [40]. Among these technologies the most important are $SiN_x$, $Al_2O_3$ and a-Si:H, with the first two owing their passivation effect to the presence of fixed charges, either positive for $SiN_x$ or negative for $Al_2O_3$ [41], [42], and the last one to the presence of hydrogen atoms which provide an excellent chemical passivation at the interface with c-Si [43]. However, it is important to note that, when a dielectric film is used to passivate the silicon surface, it is likely that both chemical and field-effect mechanisms contribute the overall passivation result. Understanding the influence of each of these mechanisms for different passivation layers could help elucidate ways to make them more effective, and ultimately achieve higher solar cells efficiencies. The ground mark for this type of analysis is presented in this dissertation

### 3.3.1 Amorphous Silicon

Intrinsic amorphous silicon a-Si:H(i) films have been known for some decades to yield good c-Si surface passivation [43]. Sanyo, now owned by Panasonic, first developed the heterojunction silicon solar cell in the 1980-1990s [44] which first combined the reduction of the recombination losses typical of metal-semiconductor contacts with the selective conduction of one type of charge carrier in order to increase the device efficiency. When

used in a cell, however, a stack of intrinsic and doped a-Si films is required in order to allow the charge carriers collection. Apart from its excellent passivation characteristic, a-Si introduces the additional benefit of a low-temperature deposition. From the point of view of solar cell manufacturing, the low thermal budget required makes the cells manufacturing significantly cheaper. Furthermore, avoiding a high-temperature step helps reduce the diffusion of impurities into the silicon material and thus maximize the lifetime after processing.

Experimentally, the most common way to deposit these films is via plasma-enhanced chemical vapor deposition (PECVD) using silane ($SiH_4$) as the precursor gas, usually diluted in hydrogen ($H_2$). The gasses are then dissociated in the deposition chamber by a plasma ignited between the shower head and the sample plate.

In this work, a-Si films were deposited using an industrial standard Applied Materials P-5000 cluster PECVD tool. This multichamber tool is a conventional (direct) plasma-enhanced chemical deposition (PECVD) with a capacitive RF discharge generated at 13.56 MHz. The depositions were carried out in three different chambers dedicated to intrinsic, *p*- and *n*-doped films. As the tool accommodates standard 156 mm square solar wafers, we made use of a carrier to process our 2'' samples, usually placing four of them on the same carrier. Amorphous silicon layers were deposited on both sides of the wafers which were manually flipped between depositions.

In the first part of this work, 50 nm of a-Si:H(i) were deposited on both sides of the *n*-type FZ silicon samples. Some of the samples were then subsequently re-processed by

deposition of either *p*- or *n*-doped 10 nm-thick a-Si layers on top of the intrinsic one. All depositions were performed at 250 °C.

### 3.3.2 Silicon Nitride

Silicon nitride has represented for a long time the most established passivation technology for commercial production of silicon solar cells [45]–[47]. Three main advantages have contributed to make $SiN_x$ very successful. First, its refractive index is such that by tailoring the film thickness, it can serve as an excellent antireflection coating when the cell is encapsulated. Second, during its deposition a large quantity of hydrogen is released, which helps passivate many surface and bulk defects, both during the film deposition and by subsequent redistribution of the H remaining in the film using a post-deposition annealing treatment. Third, its passivation properties come from a contribution of both chemical and field-effect passivation via built-in positive charges, and thus can be balanced to provide the best result possible, for example by varying the silicon/nitride ratio [48], [49].

In this work, different samples were coated with $SiN_x$ passivation layer using two experimental setups located either at ASU or at UNSW.

#### *3.3.2.1 $SiN_x$ Processing at ASU*

For the substrates processed at ASU, the same PECVD chamber used for the deposition of intrinsic amorphous silicon was also used for the deposition of $SiN_x$. In this case the precursor gasses were silane ($SiH_4$) and ammonia ($NH_3$) with a 30/90 ratio, which are fed

into the chamber though a shower head and break down during plasma. Figure 3.5 shows a simplified sketch of a typical CVD reactor.

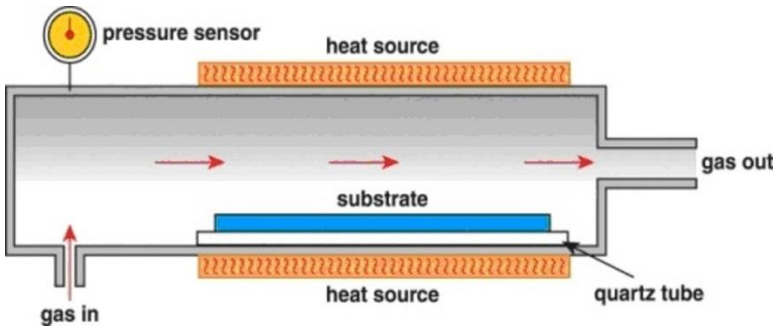


Fig. 3.5 Figure from [9] showing a typical CVD reactor.

As $SiN_x$ usually serves as the passivation layer and the anti-reflective coating (ARC), the thickness of the film is defined to carry out both these functions. We thus deposited the standard 78 nm-thick $SiN_x$ layers on both sides of Si samples at 350 °C.

*3.3.2.2 $SiN_x$ Processing at UNSW*

For the samples processed at UNSW, an industrial scale PECVD system (MAiA, Meyer Burger) was used. The tool is a dynamic high-frequency (2.45 GHz) remote PECVD system. The substrates were then double-side coated with ~110 nm of $SiN_x$ to provide the best possible passivation properties.

### 3.3.3 Aluminum Oxide

Aluminum oxide synthesized via atomic layer deposition (ALD) has been one of the main technology breakthroughs in terms of silicon surface passivation in the recent years [50]. Figure 3.6 shows a simplified sketch of the ALD technique steps [10].

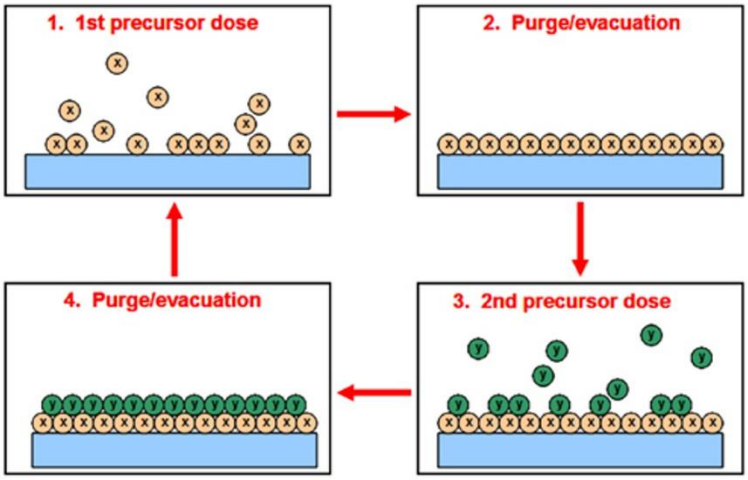


Fig. 3.6 Figure from [10] showing a simplified sketch of the atomic layer deposition (ALD) technique utilizing two distinct precursors sequentially dosed to the substrate producing a chemical reaction.

Its main advantage over other passivation layers such as $SiN_x$ and silicon oxide ($SiO_x$) is the presence of fixed negative charges rather than positive ones. This makes $AlO_x$ particularly suited for the passivation of *p*-type surfaces since the negative charges do not induce an inversion layer which is known to lead to shunting losses at the solar cell level [51], [52]. This is particularly important given that *p*-type silicon surfaces play a key role in some of the most advanced solar cell architectures including *n*-type local-BSF cells with a passivated front boron emitter [53], or *p*-type PERC cells with the rear *p*-surface passivated [54]. However, the deposition conditions can be changed so that small negative charge concentration can be introduced in the material instead of positive ones, which also makes $AlO_x$ films potentially suitable for *n*-type surfaces [50]. As a result, these films have shown surface recombination velocities (SRV) of about 10 cm/s for both *p*- and *n*-type silicon [19], [51], [55].

In this work, we used a Cambridge NanoTech Savannah S100 thermal atomic layer deposition tool. The synthesis of $Al_2O_3$ was carried out at 300 °C via the dissociative chemisorption of trimethylaluminum (TMA) on the substrate surface, which leaves it covered with an $AlCH_3$ layer. The subsequent introduction of $H_2O$ vapor leads to the formation of $CH_4$ as a reaction by-product and results on a hydroxylated $Al_2O_3$ surface. The samples underwent the chemical cleaning and etching procedure described above before deposition and were then double-side coated with 7 nm-thick $Al_2O_3$ layers in one run since ALD is conformal.

### 3.4 Annealing Process

All samples processed at ASU underwent an annealing process after their respective dielectric layer deposition to "activate" the passivation effect. $SiN_x$ and a-Si coated samples were processed in a muffle furnace for 30 minutes at 500 °C and 280 °C, respectively, whereas samples coated with $Al_2O_3$ where subjected to a rapid thermal annealing (RTA) at 425 °C for 5 minutes using a rapid thermal processor located in the SPL laboratory. No annealing treatment was performed on the $SiN_x$-coated samples processed at UNSW.

# 4 MATERIAL CHARACTERIZATION

This chapter describes the characterization techniques used in this work. The three characterization techniques that were used to evaluate the properties of the different samples were: temperature- and injection-dependent lifetime spectroscopy (TIDLS), corona charge capacitance-voltage (C-V), and surface photovoltage spectroscopy (SPS). In addition, the samples were characterized before deposition of the dielectric layers by four point probe (4PP) for resistivity measurements to calculate the doping density value. During the chemical processing, the samples were also systematically weighted before and after every subsequent acid-etching process to determine their thickness variation.

## 4.1 Temperature- and Injection-Dependent Lifetime Spectroscopy

After the deposition of passivation films on the different substrates, the samples were measured via TIDLS. This is a well-established technique in the photovoltaic industry for the characterization of silicon material through the evaluation of the effective minority-carrier lifetime ($\tau_{eff}$), which is one of the most important figure of merit to assess the material's quality, and represents the average time occurring between the generation of an electron-hole pair by mean of an external excitation (such as incident light) and its recombination. TIDLS requires little sample preparation before measurement, it is contactless, and non-destructive, and thus the measured minority carrier lifetime can be monitored along the entire solar cell manufacturing process and help identify the possible harmful processing steps. In the last decade, its capabilities have been extensively exploited to extract information about the lifetime-limiting defects in silicon material. In particular, defects' parameters such as the

defect energy level in the band gap ($E_t$), and the capture cross section ratio ($k$). The $T$-dependence of the hole and electron capture cross section, $\sigma_p(T)$ and $\sigma_n(T)$, respectively, have been confirmed or even assessed for the first time thanks to this technique [16], [17], [56]–[58].

The samples' minority-carrier lifetime was measured using a Sinton Instruments WCT-120TS [59] which is equipped with a heating stage that allows the tool to work in a range of temperatures between 25 to 230 °C. The Sinton lifetime tester is shown in Fig. 4.1.

Fig. 4.1 Sinton lifetime tester WCT-120TS in the DEfECT laboratory.

The instrument uses a filtered xenon flash lamp to inject carriers into the silicon sample, and an eddy-current conductance sensor to measure the photoconductance variation happening in the material over time. At the same time, the illumination intensity is evaluated through a separated reference cell previously calibrated. The lifetime is then obtained thanks to the general equation

$$\tau = \frac{\Delta n}{G - \frac{d\Delta n}{dt}} \tag{17}$$

where $\tau$ is the measured lifetime, $G$ is the generation rate, and $\Delta n$ is the excess carriers concentration.

Given the high values of $\tau_{eff}$ obtained (>> 200 μs) for all the samples, experimental data were acquired in transient mode. Under these conditions, the sample is subjected to a short pulse of light that decays to a much faster rate than the recombination mechanism and thus the generation rate term in Eq. 17 can be neglected, simplifying the equation to

$$\tau = -\frac{\Delta n}{\frac{d\Delta n}{dt}} \tag{18}$$

During this study, every measure was averaged over 20 acquisitions to improve the signal to noise ratio.

On the contrary, when the measured sample's lifetime is lower than 200 μs the tool should be operated in the quasi-steady-state (QSS) mode. Under these conditions, the sample is subjected to a long, slowly-decaying pulse of light with a decay constant at least 10 times slower than the carrier lifetime. In this way the excess carrier populations are always in steady-state indicating that the generation and recombination rates are in balance at all injection densities and the transient term in Eq. 17 can be neglected, which simplify the equation to

$$\tau = \frac{\Delta n}{G} \tag{19}$$

### 4.1.1 Sample Uniformity Temperature Evaluation

Before undertaking TIDLS measurements, we performed a thorough analysis of the temperature uniformity of the sample on the heating stage as this is heated to 230 ºC and subsequently left cooling down to room temperature. This was required because the tool is optimized for 6'' wafers whereas, given the size of our samples (2''), they had a significant portion hanging on top of the coil used for photoconductance measurement, hence not in contact with the heated part of the stage. The analysis was performed by attaching two thermocouples on a 2'' dummy wafer placed in the middle of the heating stage. Figure 4.2 shows the positioning of the first thermocouple in the center of the wafer on top of the measuring coil, and the second one on the edge of the wafer, in a region where the sample is in direct contact with the heating element.

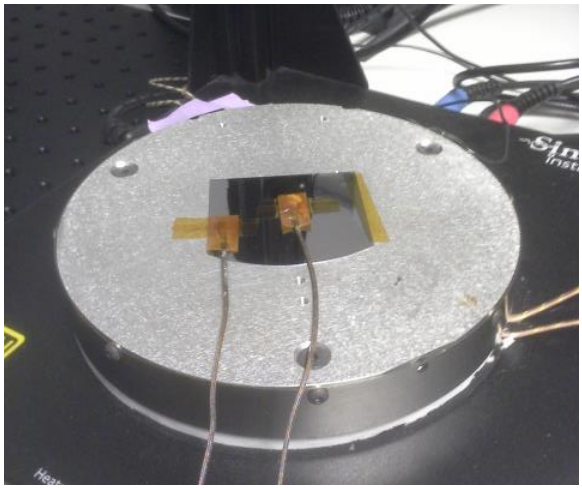

Fig. 4.2 Experimental setup for the evaluation of temperature uniformity during TIDLS measurements.

The measurements were performed across a range of temperature from 25 °C to 230 °C as the temperature was increasing up to the maximum value and then decreasing down to room temperature with a step of 10 °C. The temperatures measured in the center and at the edge of the sample were found to differ substantially with a discrepancy as high as 40 °C for the maximum temperature of 230 °C. Interestingly, we found that the difference in temperature between the center and the edge of the sample was not the same during heating and cooling, with a smaller difference in the latter case. This is due to the higher level of control on the uniformity of the sample's temperature achieved during the cooling part of the measurement. While heating up the stage, in fact, the heat sources are very well localized on a few spots of the stage, and produce a higher discrepancy among different regions of the sample. While cooling down, on the opposite, the sample is not subjected to localized stimulus and the temperature changes more uniformly due exclusively to the contact with air.

Figure 4.3 shows the temperature difference between the center and the edge of the wafer as the temperature is increased (red arrow) and decreased (blue arrow).

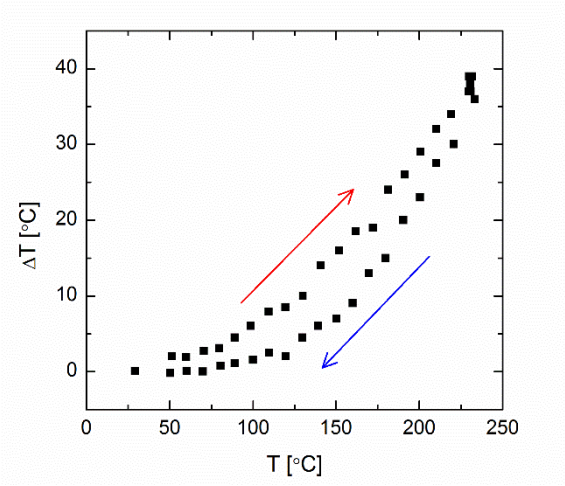


Fig. 4.3 Temperature difference among the center and the edge of the sample as function of the stage's temperature. As the temperature is increased (red arrow), and decreased (blue arrow) the temperature discrepancy on the sample's surface increases. The difference is higher during the heating stage of the measurement.

We will see in the experimental results section that this “hysteresis” loop may have important consequences in the temperature-dependent lifetime measurements.

## 4.2 Modified Sinton Lifetime Tester

Along with the standard version of the Sinton WCT-120TS lifetime tester described in the previous section, in this work we also made use of a modified version of the same instrument developed at the University of New South Wales. Figure 4.4 shows the experimental setup for this modified version of the lifetime tester.

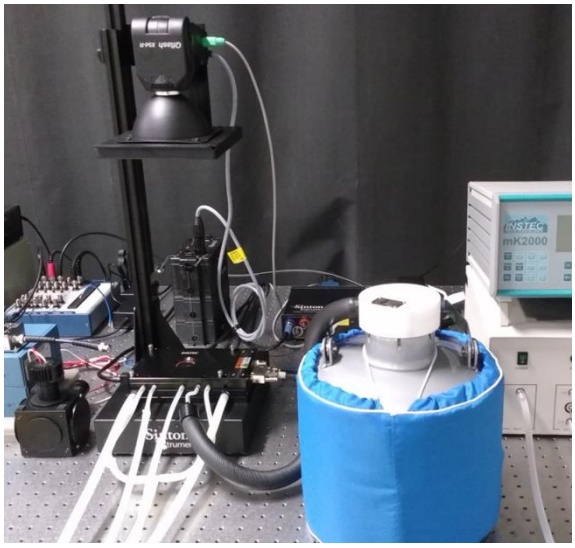


Fig. 4.4 Experimental setup of the modified Sinton WCT-120TS lifetime tester developed at the University of New South Wales.

In particular, the instrument is equipped with two different light sources, a high-power Xenon flash and a 1.5 W array of 810 nm light emitting diodes (LEDs). The control of the light source is accomplished by a digital-analog port of a data acquisition card. The software allows the user to design a wide range of waveforms, to choose the number of repetitions, the

sampling rate and the signal averaging. Furthermore, the temperature-controlled stage was modified to allow measurements to be acquired in an extremely wide range of temperatures, including values well below 0 °C. Thanks to this unique characterization tool, $\tau_{eff}$ can be measured in an injection range of $5\times10^{12}$ $cm^{-3}$ – $5\times10^{16}$ $cm^{-3}$ and a range of temperature of -75 °C – 250 °C.

## 4.3 Corona-Voltage Measurement

Contactless corona-voltage (C-V) measurements were performed using a PV metrology system from Semilab (PV-2000). Figure 4.5 shows the key elements of the experimental apparatus.

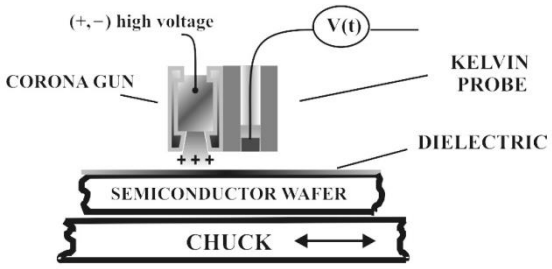


Fig. 4.5 Image from [11]. Sketch of the experimental apparatus used for the contactless corona-voltage measurements. A corona-gun is used to charge a dielectric surface with ions inducing a variation in the electrostatic potential which is then measured by a non-contact Kelvin probe to calculate the density of fixed charges, $Q_f$, and the density of the defect states at the interface, $D_{it}$, as a function of the energetic position in the Si bandgap.

The measurement is based on charge deposited by a corona gun onto the dielectric film. This process is based on the presence of an electric field strong enough so that accelerated electrons colliding with atoms in air leads to their ionization into positive ions. This in turn, generates more electrons which can be accelerated to ionize more atoms in a chain reaction process called an “electron avanlance”. The C-V technique makes use of this process to

charge a dielectric surface with ions created by a corona discharge in air. Subsequently, a vibrating non-contact Kelvin probe senses the change of the electrostatic potential in the dielectric film which is then used to calculate the density of fixed charges in the dielectric, $Q_f$, and the density of defect states at the interface, $D_{it}$, as a function of the energetic position in the Si bandgap [60], [61]. No need for preparation of any test structures results in cost and time saving advantages over the commonly used MOS C-V technique.

## 4.4 Surface Photovoltage Spectroscopy

Surface photovoltage (SPV) has recently emerged as a valuable technique for the analysis of surface and interfaces in photovoltaic devices.

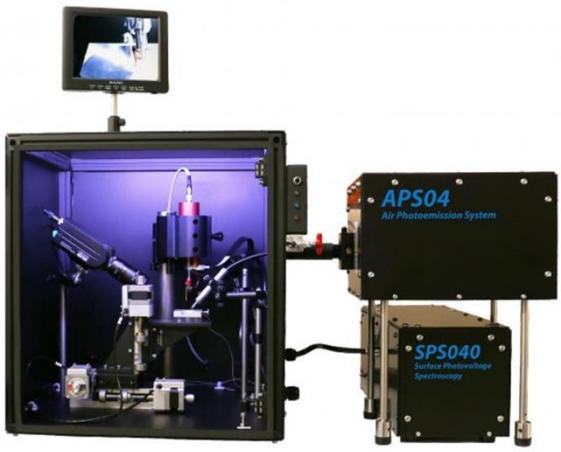


Fig. 4.6 Image from [12]. Surface photovoltage spectroscopy experimental setup.

SPV is a non-contact and non-destructive experimental technique that relies on the measurement of the work function (WF) difference between a Kelvin probe and the sample's surface. This quantity is defined as the contact potential difference (CPD) and carries

fundamental information about the presence of defect states. Figure 4.7 shows a schematic representation of the SPV technique functioning and of the measured parameters.

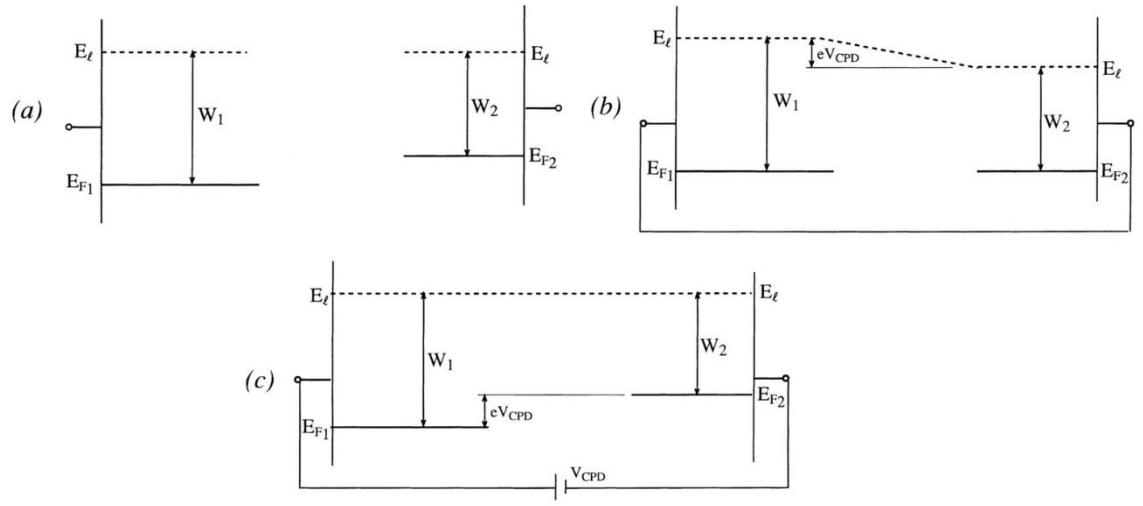


Fig. 4.7 Schematic representation of the SPV technique and of the measured parameters. a) The sample and the tip are not in electrical contact; b) the sample and the tip are put under short-circuit conditions and a potential is formed among them; c) the tool applies a CPD to nullify the current running between sample and tip.

Surface photovoltage spectroscopy (SPS) can be carried out by illuminating the sample with monochromatic light, which allows the identification of band-to-band and intra-gap transitions due to confinement effects and/or defect states following the analysis presented by E. Fefer and Y. Shapira [13]. The fundamental physical picture associated with the application of the surface photovoltage spectroscopy method was presented by E. Fefer and Y. Shapira [13] and relies upon the evaluation of the "band bending" variation due to the semiconductor's near-surface space-charge region under electron depletion conditions. In particular, upon photoelectron excitation to the conduction band, the bands bend downward and a negative photovoltage, *U*, is induced between the semiconductor surface and an external capacitative probe, i.e., the Kelvin probe. On the contrary, the transition of an

electron from the valence band into an empty localized state is equivalent to external reverse (negatively) biasing of the semiconductor space-charge region. As the light wavelength is swept across the 400 nm – 1000 nm range, the $U(hv)$ spectrum is collected and each slope variation indicates the presence of a defect level, thus allowing the identification of their energy distribution in the material bandgap. An example of this analysis is presented in Fig. .

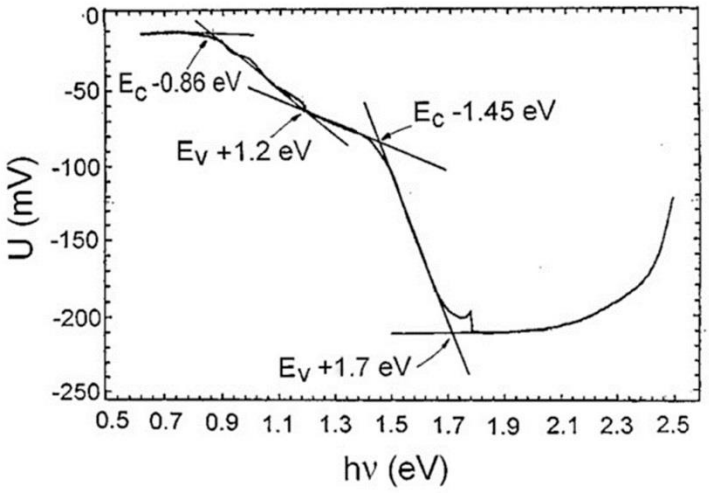


Fig. 4.8 Figure from [13]. Surface photovoltage spectroscopy showing the variation of the CPD between sample and tip as a function of the incoming photon energy. Every slope variation in the signal indicates the presence of a carrier transition between the energy bands and/or a defect state.

Furthermore, it has been suggested that the height of the peaks in the SPS spectrum can be roughly considered proportional to the density of defect states, $N_s$, [62] so that the impact of a processing step can be immediately evaluated.

# 5 SURFACE PASSIVATION ANALYSIS

In this Chapter we will discuss the surface passivation results obtained from the analysis of samples passivated with different dielectrics. The reported SRV values are experimentally obtained by applying the thickness variation method [63] so that no assumptions are made a priori on the quality of the substrate or the passivation level. The method consists in the extrapolation of the surface recombination velocity from effective lifetime measurements thanks to the variation of the samples substrate thickness: in fact, for double-side coated samples with a minority carrier diffusion length greater than the sample width ($W$), and for sufficient low SRV, the effective lifetime can be expressed as [64]

$$\frac{1}{\tau_{eff}(\Delta n, T)} = \frac{1}{\tau_{bulk}(\Delta n, T)} + \frac{2 \cdot SRV(\Delta n, T)}{W} \tag{20}$$

where $\tau_{eff}$ is the effective lifetime, and $\tau_{bulk}$ is the bulk lifetime. Thus, by measuring samples with different thicknesses, the $SRV$ values at every temperature and injection level can be obtained by interpolating $1/\tau_{eff}$ vs $1/W$ with a linear fit and evaluating its slope. From the intersection of the linear fit with the $y$-axis $1/\tau_{bulk}$ can be also be extrapolated. These observations are exemplified in Fig. 5.1 for three different injection density values.

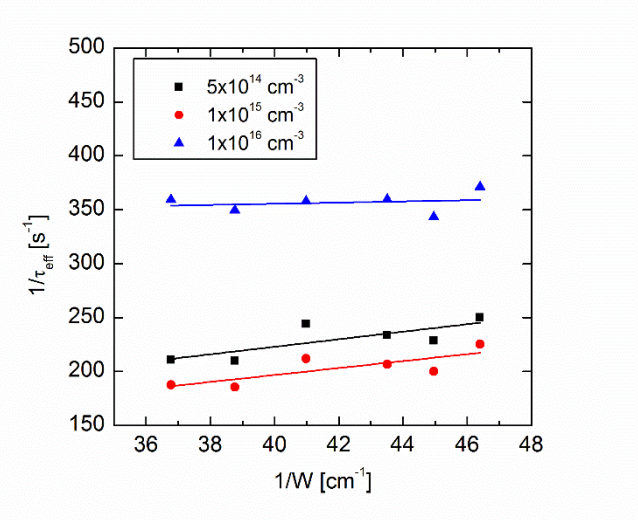


Fig. 5.1 Inverse of the effective lifetime as a function of the inverse of samples' thickness. From the slope of the linear fit, the surface recombination velocity can be obtained at each injection level. The bulk lifetime can be extrapolated from the intercept of the linear fit with the *y*-axis.

## 5.1 Importance of Chemical Processing

As described in Section 3.2, the samples utilized in this work were subjected to a thorough and complex chemical cleaning procedure in order to eliminate both organic and inorganic impurities from the substrates before the deposition of the dielectric layer. Despite this procedure being a well-established one for the treatment of silicon material, the sensitivity of the analysis performed led us to quickly realize that the standard operating procedure commonly followed by the SPL users to maintain the wet baths free of contaminants did not provide the required level of cleanliness. Figure 5.2 shows the inverse of effective lifetime as function of inverse thickness for samples processed using "aged" chemical solutions (encircled in red), or using "fresh" chemical solutions (encircled in blue). All the other processing steps were performed simultaneously for all samples and thus should not introduce any variation.

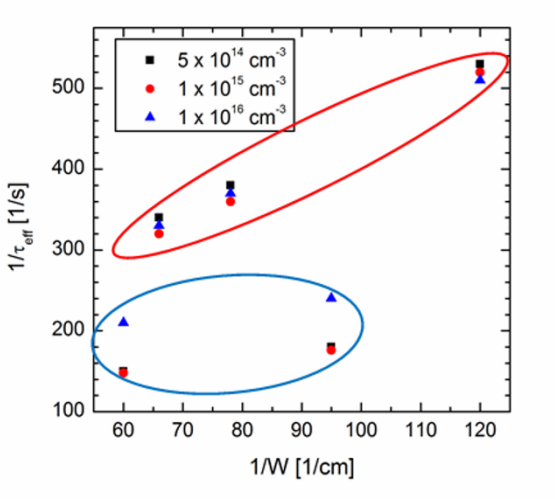


Fig. 5.2 Inverse effective lifetime as function of inverse thickness for samples prepared in different batches. Data for samples circled in red were processed in "aged" chemical solutions and result in a higher SRV than those processed in "fresh" chemicals circled in blue.

From the thickness variation analysis performed on data shown in Fig. 5.2 according to Eq. 20, it is immediately clear that the status of the chemical solutions used to process the samples has a decisive impact on the surface recombination velocity. In fact, for samples processed using "aged" solutions, an SRV as high as 18 cm/s was calculated whereas for samples processed with "fresh" solutions the SRV obtained was below 2 cm/s. Based on this information, we established the process flow described in Section 3.2.

## 5.2 Temperature-Controlled Stage Instability

For the analysis of PECVD-deposited intrinsic amorphous silicon we processed four samples with a thickness varying across the range of 160 µm – 270 µm according to the procedure described in section 3.2. In order to evaluate the possible modification of the samples happening during the temperature scan, we acquired data continuously as the temperature was increased from 25 ºC to 230 ºC and then decreased back to room

temperature. In the case of samples passivated with a-Si:H(i), we encountered some differences among data coming from the increasing and decreasing temperature scans. The lifetime at room temperature before and after the measurements was found to be the same. However, the intermediate values were found to disagree substantially creating a “hysteresis” loop. Figure 5.3 depicts the effective lifetime results for the 160 μm-thick sample as the temperature is increased (red arrows) and then decreased (blue arrows).

After the evaluation of the temperature of samples on the heating stage reported in section 4.1.1, we were able to determine this behavior as due to the difference of temperature between the center and the edge of the sample measured while performing the temperature scan described in Fig. 4.3. As the temperature of the samples was found to be more uniform during the cool down scan, all measurements hereafter will correspond to that portion of the temperature loop.

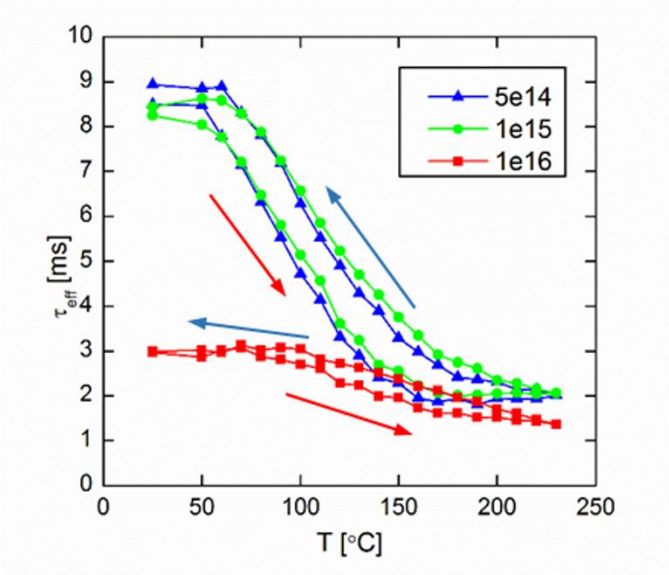


Fig. 5.3 Lifetime measurements at different injection levels taken as the temperature is increased (red arrows) and then decreased (blue arrows) for the 160 μm-thick sample coated with a-Si:H(i) showing the "hysteresis" loop.

## 5.3 Passivation by a-Si:H

In this section, we present the results obtained on high-quality FZ c-Si samples passivated with either a-Si:H(i) alone or a stack of a-Si:H(i)/ a-Si:H($n^+$). First we will report on the experimentally evaluated SRV for samples coated with a-Si:H(i) at different temperatures and injection densities. We will complement the data obtained via TIDLS with the analysis performed via SPS which provides insights about the energy distribution of defect states at the interface and their variation upon high-temperature thermal treatment of the samples. Subsequently, we will analyze the evolution of the SRV temperature- and injection-dependence when an additional layer of *n*-doped a-Si:H is deposited on top of the samples. All these results will then be studied by applying an amphoteric defect model in order to extrapolate the fundamental surface passivation parameters such as defect states density at the interface, $N_S$, and the fixed charge at the interface, $Q_f$. Finally, we will show the degradation occurring on the a-Si:H(i)-coated samples over 28 months of storage in air. By re-evaluating the SRV after the degradation has occurred we are able to demonstrate that the degradation is entirely ascribable to the partial effusion of hydrogen from the passivation layer and not to a variation of the material bulk quality.

Figure 5.4 shows the $\tau_{eff}$ vs. injection level curves at different temperatures for the thickest sample ($W$ = 260 $\mu$m) passivated with a-Si:H(i). Samples with smaller thickness show a slightly lower effective lifetime consistently with Eq. 20, but an overall similar behavior.

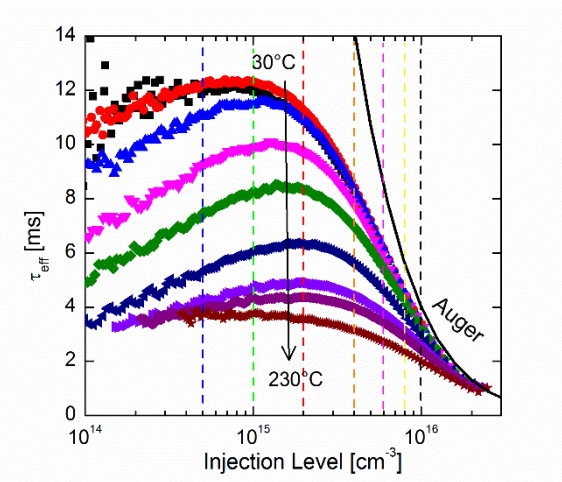


Fig. 5.4 Effective minority-carrier lifetime as function of injection level at temperatures with 20 °C step size for a high-quality Si sample 260 μm thick passivated with 50 nm of a-Si:H(i). Dashed lines values are shown in Fig. 5.5.

The effective lifetime is found to be strongly temperature- and injection-dependent with values at $\Delta n = 10^{15}$ cm$^{-3}$ going from about 12 ms at room temperature to below 4 ms at 230 °C. The effective lifetime is then seen to drop significantly for both low and high injection density, in the latter case as a result of the dominance of Auger recombination mechanism. Additionally, we further notice that the *T*-dependence of $\tau_{eff}$ varies with the carrier injection level. For this reason, we extract *T*-traces for each injection level indicated by a dashed vertical line in Fig. 5.4. Figure 5.5 depicts the effective lifetime *T*-dependence at different injection levels.

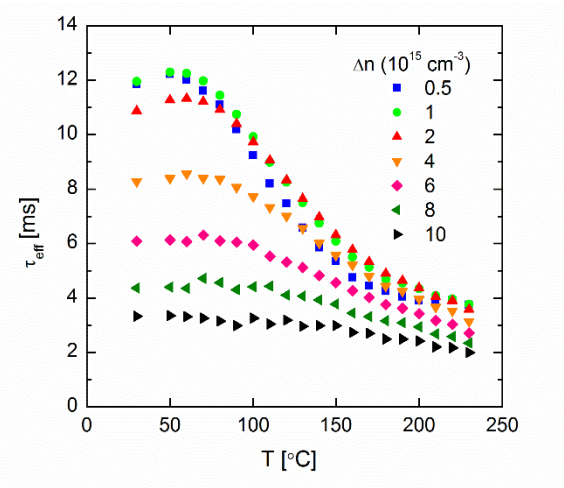


Fig. 5.5 Temperature-dependence of $\tau_{eff}$ at different injection levels for a high-quality Si sample 250 μm-thick passivated with 50 nm of a-Si:H(i).

After an initial increment with temperatures up to 60 °C the effective lifetime is found to decrease monotonically with increasing *T*. This trend tends to disappear with increasing injection level as the effective lifetime starts to be mostly limited by the temperature-independent Auger recombination mechanism. Similar $\tau_{eff}$ trends have been recently reported by J. P. Seif *et al*. [65] and have been linked to the *T*-dependence of recombination mechanisms happening at the c-Si surface rather than in the c-Si bulk. Thanks to the experimental evaluation of SRV carried out according to Eq. 20, we are now able to prove that this assumption is, in fact, correct. Figure 5.6 shows the experimental surface recombination velocity results in the whole temperature range.

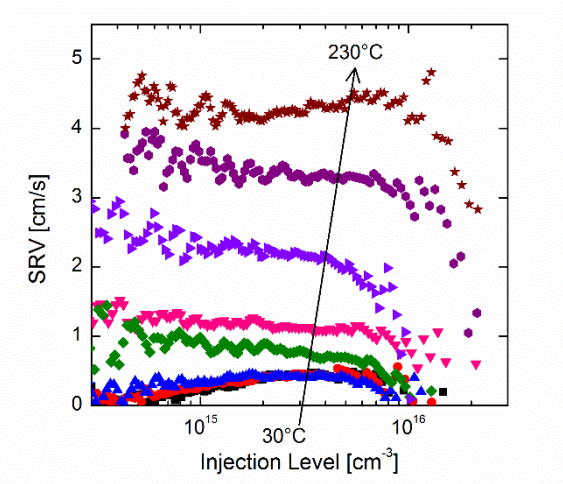


Fig. 5.6 Surface recombination velocity as function of injection level at different temperatures with 20 °C step size for high-quality Si samples coated with 50 nm of a-Si:H(i).

At room temperature an outstanding SRV below 0.5 cm/s at an injection level equal to $10^{15}$ $cm^{-3}$ is obtained – to the authors knowledge this represents the best passivation provided by amorphous silicon alone on *n*-type substrates reported up to date, in line with results by S. Herasimenka *et al.* [66] who reported a record $V_{OC}$ for a device processed with a similar passivation scheme. SRV is then found to increase as the temperature rises above 100 °C although never surpasses 5 cm/s in the temperature and injection level ranges evaluated here. This result constitutes a complete new approach to this type of studies as the SRV injection and temperature dependence has never been experimentally reported before for any passivation scheme. The SRV *T*-dependence accounts for the diminishing $\tau_{eff}$ observed in Fig. 5.4 with the surface recombination contribution becoming more dominant at high temperature. In Section 5.3.3 we will make use of the amphoteric model for dangling bonds to extrapolate meaningful information about the distribution of defects at the interface based on the SRV experimental results. Furthermore, as we will see in the Chapter 6, the herein

evaluated STV *T*-dependence has profound implications in the analysis of impurity defect levels contained in the bulk of the material as the correlation among effective lifetime and bulk lifetime is not as straightforward as generally assumed.

### 5.3.1 SPV Analysis

Figure 5.7 shows the SPS spectrum for an as-deposited high-quality *n*-type sample passivated with intrinsic a-Si:H.

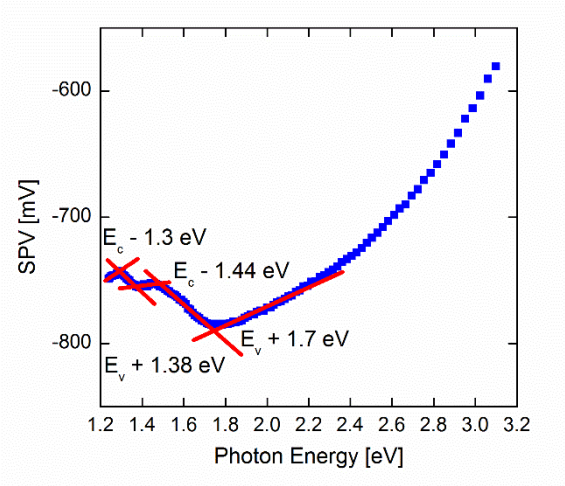


Fig. 5.7 Surface photovoltage spectroscopy result for a high-quality n-type sample passivated with intrinsic a-Si:H with no thermal treatment applied. Each slope variation in the U(hv) signal corresponds to an electronic transition. The transition at $E_v$ + 1.75 eV corresponds to the band-to-band excitation of an electron in the a-Si:H(i) layer whereas any slope variation in the energy range below that value indicates the presence of a defect level.

Several slope variations are easily identified in the *U*(*hv*) spectrum. The one observed at the highest energy value, i.e. $E_v$ + 1.75 eV, corresponds to the band to band transition in a-Si:H(i) layer and is in good agreement with the bandgap values of 1.72 eV previously reported for a-Si:H(i) [62], [67]. At lower energies, three more slope variations are found at $E_c$ - 1.3 eV, $E_v$ + 1.38 eV, $E_c$ - 1.44 eV. The last two defect levels have previously been

reported and have been associated with the presence of dangling bonds at the c-Si/a-Si:H(i) interface [13], [62].

Figure 5.8 shows the results of the SPS measurements on an equivalent sample as the one reported in Fig. 5.7.

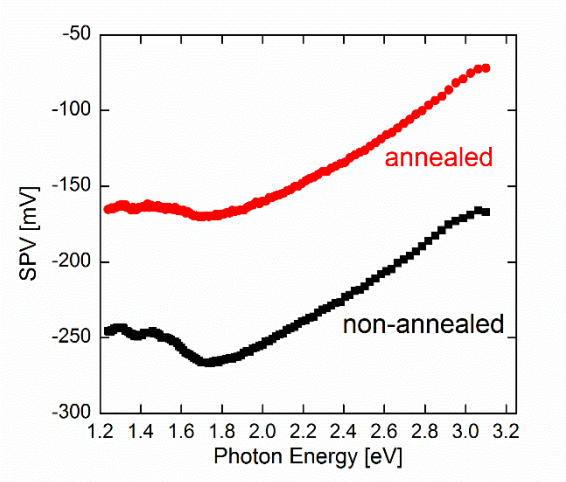


Fig. 5.8 Surface photovoltage spectroscopy results on a high-quality n-type sample passivated with a-Si:H(i) both before and after the thermal treatment at 280 °C had been carried out. After annealing, the SPS signal shows an overall increment which indicates the decrement of defect density of states. Furthermore, the slope variations in the energy region below a-Si:H bandgap have also significantly decreased which corroborates the association of these defect states to dangling bonds effectively passivated after the thermal treatment.

In this case the measurement was performed both before and after the standard annealing treatment at 280 °C for 30 minutes. After annealing the sample, the SPS signal significantly increases in the whole energy range, which indicates an overall reduction of density of defect states. Remarkably, the most significant variation is found for energy values below the a-Si:H(i) bandgap of $E_v$ + 1.75 eV where the strong slope variations previously observed are almost completely eliminated. This finding indicates that the re-distribution of hydrogen in the a-Si:H(i) layer due to the thermal treatment has effectively passivated these defect levels

corroborating their association with the dangling bonds at the c-Si/a-Si interface. These variations have a strong impact on the sample's effective lifetime as shown in Fig. 5.9.

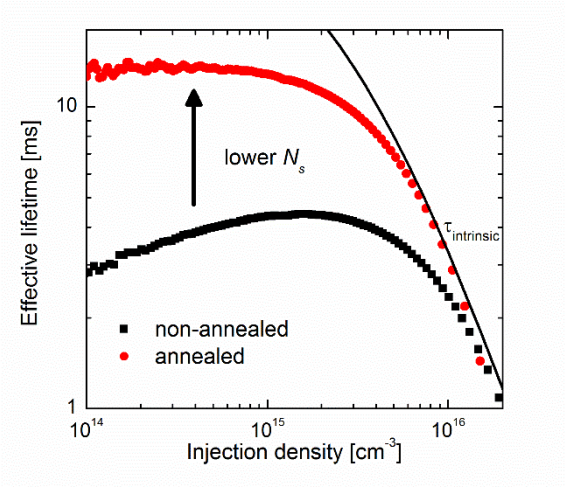


Fig. 5.9 Effective lifetime as a function of excess carrier concentration for high-quality *n*-type sample shown in Fig. 5.8 passivated with intrinsic a-Si:H before and after annealing treatment at 280 °C.

### 5.3.2 a-Si:H(i)/a-Si:H(n$^+$) stack layer

As in real devices such as silicon heterojunction solar cells (SHJ) the intrinsic a-Si:H layer is always coupled to a doped a-Si:H layer working as a carrier-selective contact, we further processed our samples by depositing a 10 nm thick layer of a-Si:H(n$^+$) with an estimated doping concentration of $10^{19}$ cm$^{-3}$ on both sides of the samples already analyzed in the first part of this chapter.

The $\tau_{eff}$ vs. injection level curves at different temperatures for the thickest sample, i.e., 260 μm, passivated with a-Si:H(i)/a-Si:H(n$^+$) stack are shown in Fig. 5.10. As in the previous case, samples with lower thickness show a similar trend and slightly lower absolute values accordingly to Eq. 20.

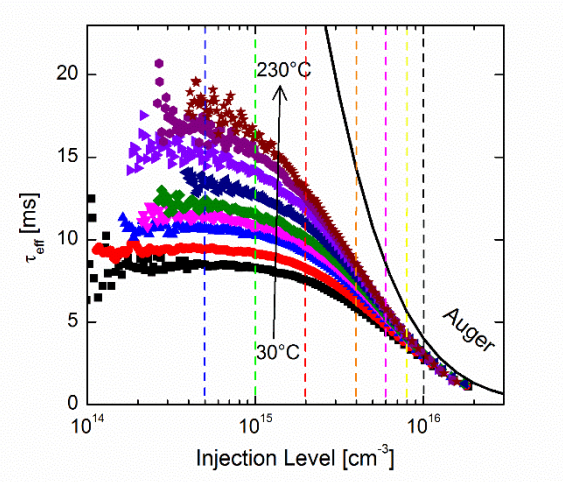


Fig. 5.10 Effective minority-carrier lifetime as function of injection level at different temperatures with 20 °C step size for a high-quality Si sample passivated with a-Si:H(i)/a-Si:H($n^+$). Dashed line values are shown in Fig. 5.11.

Similarly to samples coated only with a-Si:H(i), we notice that the *T*-dependence of $\tau_{eff}$ varies with the carrier injection level and so we extract *T*-traces for each injection level indicated by a dashed line. However, it is worth noting that in the case of samples coated with the a-Si:H(i)/a-Si:H($n^+$) stack the effective lifetime *T*-dependence is completely reversed when compared to the results shown in Fig. 5.4 for samples passivated only with a-Si:H(i). As the bulk of the samples has not changed given that we used the same substrates, it seems reasonable to make the hypothesis that the different lifetime temperature-dependence is due to a different surface passivation provided by the stack of materials in the two cases.

Figure 5.11 shows the resulting *T*-dependence of the effective lifetime at different injection levels. These results are in line with what has been recently reported for similar samples at *T* below [68] and above [65], [69] room temperature.

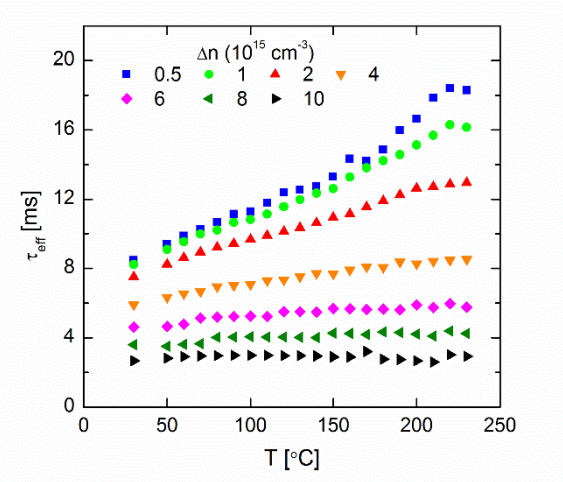


Fig. 5.11 Temperature-dependence of $\tau_{eff}$ at different injection levels for a high-quality Si sample passivated with a-Si:H(i)/a-Si:H($n^+$).

Similarly to the analysis presented in the previous section for a-Si:H(i)-coated samples, we experimentally evaluate the SRV in the whole temperature and injection density ranges by applying Eq. 20. Figure 5.12 presents the SRV results on samples coated with the stack a-Si:H(i)/a-Si:H($n^+$).

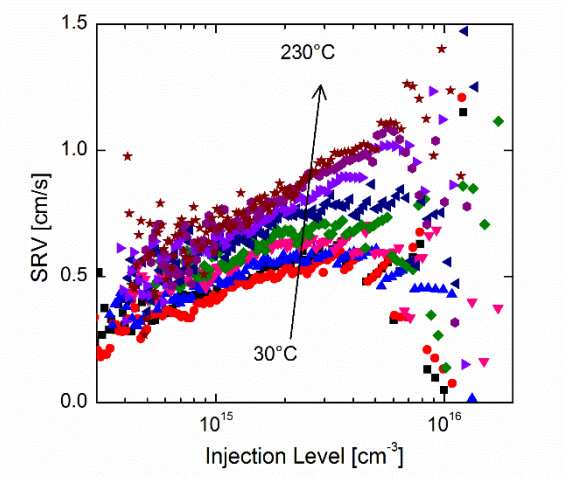


Fig. 5.12 Surface recombination velocity as function of injection level at different temperatures with 20 °C step size for high-quality Si samples coated with a-Si:H(i)/a-Si:H($n^+$).

Similar to the results obtained with intrinsic a-Si:H alone, SRV measured at room temperature is below 0.5 cm/s in the whole injection range. However, a completely different temperature-dependence is observed with SRV remaining below 1.0 cm/s even at high temperatures. An explanation for this different behavior will be provided in the next paragraph by applying the amphoteric model to the experimental results for both passivation schemes.

### 5.3.3 Modeling of Surface Recombination Velocity

In this section, we will adopt the model for a-Si:H/c-Si interface recombination proposed by Olibet *et al*. [14] based on a recombination mechanism via amphoteric defects, i.e., Si dangling bonds existing in three different state of charge, and expand it to evaluate the SRV *T*-dependence.

The typical one-electron representation of the distribution of recombination centers in a-Si:H is shown in Fig. 5.13. The model proposes that when unoccupied, the Si dangling bond (i.e., recombination center) *D* will be positively charged ($D^+$) whereas when occupied by one electron, the recombination center is neutral ($D^0$). These two charge conditions are represented here at the same energy level. When occupied by two electrons, the recombination center is negatively charged ($D^-$), and if the correlation energy *U* is positive, it is represented as upward shifted by *U*. The model has previously been found to be able to correctly quantify the two main parameters influencing the recombination rate at the interface, namely the dangling bond density, $N_s$, and the charge density at the interface, $Q_s$. However, the original purpose of this model was exclusively to describe the SRV injection-

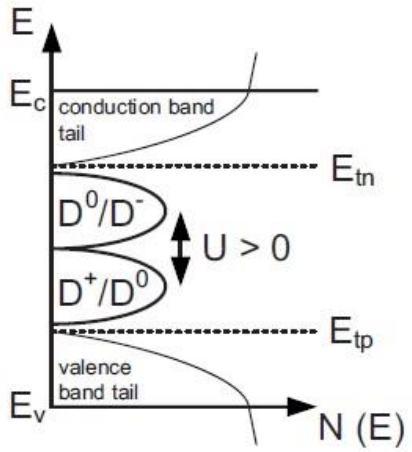


Fig. 5.13 Figure from Ref. [14]. One-electron representation of a continuous distribution of amphoteric recombination centers [density of states $N(E)$]. When unoccupied, the Si dangling bond (i.e., recombination center) $D$ will be positively charged ($D^+$); when occupied by one electron, the recombination center is neutral ($D^0$). These two charge conditions are represented here at the same energy level. When occupied by two electrons, the recombination center is negatively charged ($D^-$), and if the correlation energy $U$ is positive, it is represented as upward shifted by $U$ (as sketched here). $E_{tn}$ and $E_{tp}$ are the demarcation levels, whose position depends on the generation rate $G$.

dependence for room temperature measurements and thus its capability to adapt to a temperature variation has not been evaluated until now.

Under certain conditions, the calculation of the recombination rate at the interface can be reduced to the case of a discrete recombination level with three charge states [70]. When applied to the case of recombination via dangling bond states at the a-Si:H/c-Si interface, the recombination rate, $R_s$, can be written as

$$R_S = \frac{n_s\sigma_n^0 + p_s\sigma_p^0}{\frac{p_s}{n_s}\frac{\sigma_p^0}{\sigma_n^+} + 1 + \frac{n_s}{p_s}\frac{\sigma_n^0}{\sigma_p^-}} v_{th} N_s \tag{21}$$

where $v_{th}$ is the thermal velocity, $n_s$ and $p_s$ are the densities of free electrons and holes at the interface, respectively, $\sigma_n^0$ and $\sigma_p^0$ are the capture cross sections of the neutral states, $\sigma_n^+$ and $\sigma_p^-$ are the capture cross sections of the charged states, and $N_S$ is the two-dimensional

interface state density. To describe the two-dimensional recombination, commonly the interface recombination velocity *S* is introduced [71], defined as

$$S \equiv R_S/\Delta n_s \tag{22}$$

where $\Delta n_s$ is the excess carrier density at the interface.

The interface carrier $n_s$ and $p_s$ are functions of the surface potential $\Psi_S$ that must be numerically calculated and is given by the nonlinear equation for the total image charge density induced in the c-Si ($Q_{Si}$) by the charge $Q_S$ of the dangling bonds in the a-Si:H layer

$$Q_{Si} = \pm\sqrt{\frac{2kTn_i\epsilon_0\epsilon_{Si}}{q^2}\left[e^{\frac{q(\Phi_p-\Psi_S)}{kT}} - e^{\frac{q\Phi_p}{kT}} + e^{\frac{q(\Psi_S-\Phi_n)}{kT}} - e^{-\frac{q\Phi_n}{kT}} + \frac{q\Psi_S(p_0-n_0)}{kTn_i}\right]} \tag{23}$$

where $\Phi_n$ and $\Phi_p$ are the quasi-Fermi levels of electrons and holes at the edge of the space charge region (SCR) [14].

By setting $\sigma_n^+/\sigma_n^0$ equal to $\sigma_p^-/\sigma_p^0$ we can reduce the number of variables in the model, in agreement with most reports published in literature [72]. A reasonable value of $\sigma_p^0$ = $10^{-16}$ $cm^2$ is chosen, which is typical for neutral midgap states [73]. Furthermore, we decided to fix the charged to neutral capture cross-section ratios $\sigma_n^+/\sigma_n^0 = \sigma_p^-/\sigma_p^0$ = 500 in accordance to the results reported in Ref. [14]. Equation 23 is then solved via MATLAB calculations for different $Q_{Si}$ and the best fit of the experimental data is obtained by manually choosing the parameters $\sigma_n^0$, $\sigma_n^+$, and $N_S$. The best fits to the experimental SRV values reported in Fig. 5.6 and Fig. 5.12 for samples coated with a-Si:H(i) and a-Si:H(i)/a-Si($n^+$) at different injection levels are shown in Fig. 5.14 and Fig. 5.15, respectively. The error is estimated to be on the

order of 15% resulting from uncertainties on both effective lifetime and thickness measurements.

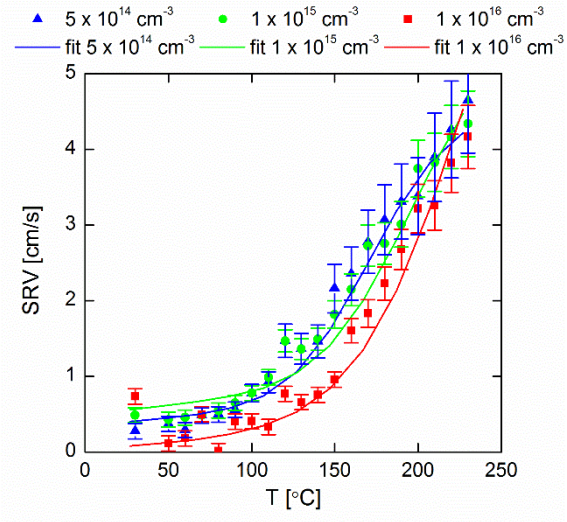


Fig. 5.14 Surface recombination velocity *T*-dependence at different injection levels for a-Si:H(i)-coated samples and corresponding fit obtained from application of Olibet's model [14]. The reported error associated with SRV values is 15%.

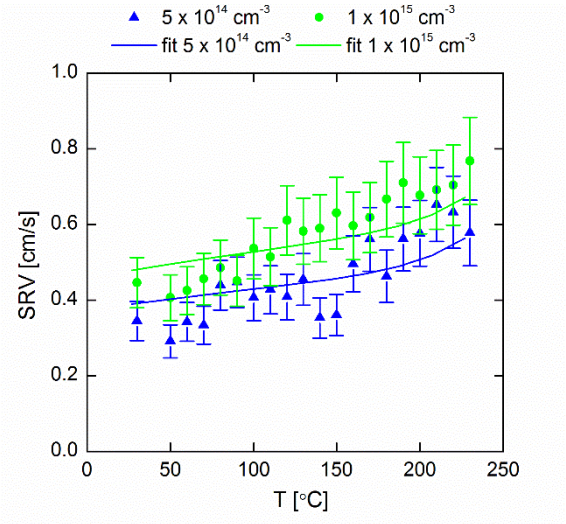


Fig. 5.15 Surface recombination velocity *T*-dependence at different injection levels for a-Si:H(i)/a-Si($n^+$)-coated samples and corresponding fit obtained from application of Olibet's model [14]. The reported error associated with SRV values is 15%.

The parameters obtained from the best fits are reported in Table 5.1.

Table 5.1 Model parameters obtained from the fitting of experimental SRV for samples coated with a-Si:H(i) and a-Si:H(i)/a-Si($n^+$) for different injection levels. $\sigma_p^0 = 10^{-16}$ and $\sigma_n^+/\sigma_n^0 = \sigma_p^-/\sigma_p^0 = 500$ are the same for all layers.

| | Injection level [$cm^{-3}$] | $N_S$ [$10^6$ $cm^{-2}$] | $\sigma_n^0/\sigma_p^0$ | $Q_S$ [$10^{10}$ $cm^{-2}$] |
|---|---|---|---|---|
| a-Si:H(i) | 5 x $10^{14}$ | 5.5 | 10 | 10.0 |
| | 1 x $10^{15}$ | 6.5 | 20 | 10.0 |
| | 1 x $10^{16}$ | 7 | 25 | 100.0 |
| a-Si:H(i)/ a-Si($n^+$) | 1 x $10^{15}$ | 4.6 | 10 | 0.5 |
| | 1 x $10^{16}$ | 4.7 | 20 | 0.5 |

From the results obtained from the best fits of the experimental SRV curves we make the following observations:

1) The interface state density, $N_S$, is orders of magnitude lower than the values reported in Ref. [14] for a-Si(i):H and decreases after the deposition of a-Si($n^+$) possibly due to the additional introduction of hydrogen at the interface.
2) The neutral capture cross-section ratio $\sigma_n^0/\sigma_p^0$ increases with increasing injection level suggesting a dependence of the recombination mechanism from the illumination level.
3) The charges at the interface are positive. The density of charges at the interface $Q_S$ increases with the injection level for samples coated with a-Si:H(i). This is due to the shift of the quasi-Fermi energy level for holes, $\Phi_p$, closer to the valence

band at high illumination levels which leads to an increment of the positively charged component of the dangling bonds $D^+$ as depicted in Fig. 5.13.

4) $Q_S$ is lower in the samples coated with an additional layer of *n*-doped a-Si:H. This is due to the shift of Fermi energy of the passivation layer towards the conduction band which results in an increment of the neutral component of the dangling bonds $D^0$ as depicted in Fig. 5.13 and thus a decrement of the positive charge density at the interface.

From these initial results, it appears that the most significant difference among samples coated with a-Si:H(i) and the stack a-Si:H(i)/a-Si($n^+$) relies on the density of charges at the interface. Thus, $Q_S$ is the parameter suspected to be responsible for the different temperature-dependent behavior seen in Fig. 5.14 and Fig. 5.15. However, note that a more in depth investigation of the model's parameter space needs to be undertaken. Experimental techniques such as corona-voltage (CV) measurements could help reduce the amount of unknowns by providing a direct measurement of the density of defect states $N_S$ and fixed charges at the interface $Q_S$.

### 5.3.4 DFT Calculations

In order to understand the experimental results shown in section 5.3.1 obtained via SPV analysis, we resolved to perform density functional theory (DFT) calculations to reveal the origin of the three defect states identified in the bandgap of the a-Si material used for passivation. The calculations were performed first by assuming an a-Si:H layer with no structural defects, i.e., neutral a-Si:H. Subsequently, a dangling bond was introduced by

removing a hydrogen atom from the system. Finally, the amphoteric nature of the dangling bond was simulated by adding a localized charge, either negative (-*e*) or positive (+*h*), on the location of the missing hydrogen. Figure 5.16 shows the resulting density of states (DOS) for these four calculations.

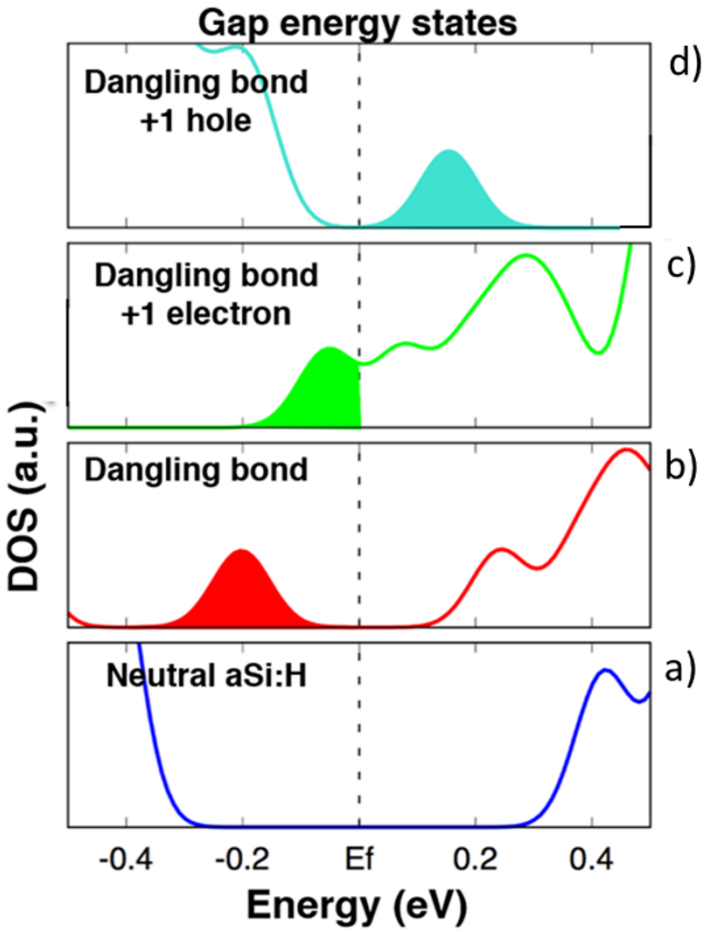


Fig. 5.16 Density of states (DOS) resulting from density functional theory (DFT) calculations for a-Si:H without dangling bonds (a), with a neutral dangling bond (b), and with a dangling bond charged either negatively (c) or positively (d). The calculations show that the presence of a dangling bond introduces a distribution of defect states in the a-Si:H bandgap depending on its charge states.

The DFT calculations show that the when a dangling bond is introduce in the a-Si:H structure, a certain density of defect states is found close to the valence band. When a

negative or a positive charge is added to the location of the dangling bond to simulate the three charge states predicted by the amphoteric model, the energy distribution of the defect states is found to change position moving below the midgap in the former case, or close to the valence band in the latter case. Thus, these results are in agreement with the experimental findings shown in section 5.3.1 and are able to explain the energy distribution of defect states in the a-Si:H bandgap as due to the presence of dangling bonds with different charge states.

### 5.3.5 Degradation Analysis

The degradation of passivation layers used for HJ devices has seen an increased interest in recent years as their market share is projected to increase from the current 2% to 15% by 2027 [74]. In particular, a-Si:H is well known to suffer from several degradation processes, e.g., Staebler-Wronski (S-W) effect [75], degradation under light [76]–[78], as well as at high temperatures [79], which significantly reduce its stability due to the formation of electronically active defects [80], most likely represented by Si dangling bonds [76], [81], [82]. Thus, reliable information on long-term stability field conditions become more and more important for the correct evaluation of the costs associated with a photovoltaic heterojunction system operation. The microscopic aspects of these mechanisms are still under debate but they are often linked to how hydrogen is bonded to Si in the a-Si:H film [83], [84]. Comprehensive studies have recently been reported which examine the degradation rates of HJ systems [85]–[87]. However, due to the intertwined nature of degradation modes, a univocal reason for the observed decay of maximum power ($P_{max}$) has been hard to identify. Results have not always been in agreement, with some reports pointing at the losses of short-

circuit current ($J_{SC}$) and fill factor ($FF$) as responsible for performance degradation [85], and others indicating the main cause for such power loss to be the degradation of $V_{OC}$ [86].

The TIDLS analysis we make use in this work is particularly suitable as it measures the effective minority carrier lifetime across a broad range of injection level, thus providing information about the recombination mechanisms affecting the device performance under different operating conditions. From the lifetime curves, in fact, the implied solar cell parameters $iV_{OC}$, and $iFF$ can be extracted [88], with the former being determined by the recombination rate at high injection level and the latter being particularly sensitive to the recombination characteristics at the injection level corresponding to the maximum power point (MPP) conditions. We then apply the thickness variation method [63] to the TIDLS data to experimentally evaluate the surface recombination velocity (SRV) temperature- and injection-dependence both before and after lifetime degradation has occurred. Finally, we fit the SRV experimental data with the same amphoteric model used in the previous section and evaluate the variation of density of defects states at the interface $N_S$ and the fixed-charge density $Q_f$. As for the results presented in the previous section, this analysis positively demonstrates that the interface-recombination model conserves its validity when applied to temperature-dependent data, which has not been previously reported.

For this part of the experiment we used the *n*-type FZ silicon samples coated with an a-Si:H(i) passivation layer as described in Section 3.2. After the initial TIDLS analysis, the samples were stored in the dark in air for a period of time of 28 months at the end of which TIDLS data were acquired once again. Finally, the samples were subjected to a second

thermal treatment equal to the first one, and then final lifetime measurement at room temperature was performed.

Figure 5.17 shows the effective lifetime curves for the 270 µm-thick sample after deposition, after the first thermal treatment, after 28 months of storage in the dark in air, and after the final annealing step. During the storage period, the samples were kept in a plastic container, placed among two layers of foam for mechanical protection, and locked in clean room cabinet. In the same graph we report the intrinsic lifetime limit due to Auger and radiative recombination mechanisms as calculated according to the Richter parameterization [19]. For each lifetime curve, *iFF* is calculated by assuming a perfect Lambertian light trapping scheme [89] giving a short-circuit current ($J_{SC}$) of 43 mA/cm$^2$. The *iFF* values are reported at the injection level corresponding to MPP conditions, whereas the $iV_{OC}$ values are reported for an injection level corresponding to a 1 sun illumination conditions.

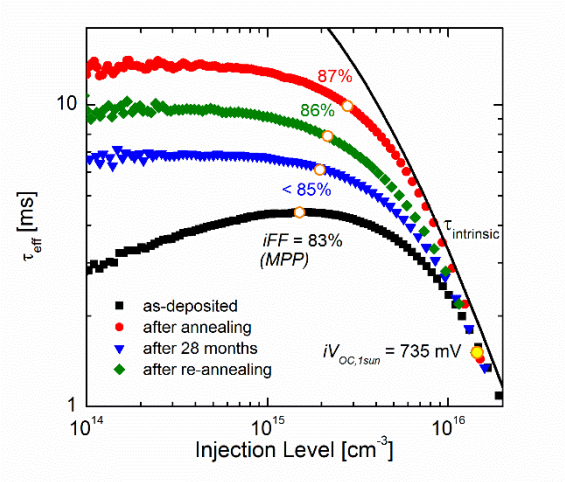


Fig. 5.17 Effective lifetime for a high-quality 270 µm-thick *n*-type sample with 50 nm-thick a-Si:H(i) layer on both sides after different processing steps and after degradation has occurred. Also shown in the graph are the values of implied fill factor (*iFF*) at each state of the sample and implied-$V_{OC}$ for an injection level corresponding to maximum power point and 1 sun illumination conditions, respectively. Intrinsic lifetime calculated according to Richter parameterization is shown for comparison.

Figure 5.17 effectively displays the effect of the first annealing treatment on the as-deposited sample with effective lifetime increasing from about 4 ms at $\Delta n$ = 1 x $10^{15}$ $cm^{-3}$ to a value above 13 ms at $\Delta n$ = 1 x $10^{15}$ $cm^{-3}$. As no variation has occurred in the substrate, this finding can be explained by two possible mechanisms affecting the passivation quality: a more effective re-distribution of hydrogen throughout the a-Si:H(i) layer [90] effectively passivating the recombination active dangling bonds, and the conversion of two DBs into a strained Si-Si bond [91], both mechanisms leading to a lower density of DBs at the a-Si:H/c-Si interface. After this first thermal treatment, the samples were stored in the dark in air for 28 months after which their lifetime was re-measured. The effective lifetime was found to substantially decrease compared to the previous measurement, especially in the lower range of injection level. The value of 6 ms at $\Delta n$ = 1 x $10^{15}$ $cm^{-3}$ is, in fact, less than half the lifetime measured right after the first annealing process. Finally, we performed a new annealing process equal to the first one and measured $\tau_{eff}$ once again. Contrary to other reports, which were able to fully reinstate their samples' initial conditions [76], [90], our samples show only a partial recovery of the effective lifetime as measured after the first annealing process with $\tau_{eff}$ being 9 ms at $\Delta n$ = 1 x $10^{15}$ $cm^{-3}$. Subsequent additional annealing processes performed on the sample proved that no further lifetime recovery was possible. This finding indicates that the passivation effect at the a-Si:H/c-Si interface has permanently decayed probably due to the partial effusion of hydrogen out of the a-Si:H(i) layer. It must be noted that these results are in disagreement with other works where it was reported than an a-Si:H(i) thickness of 50 nm would be sufficient to guarantee good temporal stability of the passivation conditions [14], [76], [92], [93].

As previously stated, Fig. 5.17 shows that the difference among effective lifetime curves is far more significant in the low injection level range, since above $\Delta n$ = 1 x $10^{16}$ $cm^{-3}$ recombination is in all cases dominated by the intrinsic Auger and radiative recombination mechanisms (black solid line). This aspect translates into a much broader variation of the calculated *iFF* compared to the $iV_{OC}$ as the former is largely influenced by the lifetime values at an injection level of 2-3 x $10^{15}$ $cm^{-3}$, corresponding to the MPP conditions, whereas the latter is determined by the intrinsically-limited lifetime at an injection level of 1-2 x $10^{16}$ $cm^{-3}$. As a result, *iFF* varies from an initial value for the as-deposited sample of 83% to a value after the first annealing process of 87%, close to the upper limit of 89% indicated by Green's empirical expression [94]. After the 28 months period of storage in the dark when degradation occurs, *iFF* goes below 85% and it is only partially recovered upon re-annealing to a value of 86%. It must be noted that the decay of *iFF*, which appears in the solar cell current-voltage (*I*-*V*) curve as an increment of the series resistance $R_S$, is in agreement with recent reports [86], [95] where increasing $R_S$ was observed even for unweathered control modules, although no clear causes could be identified [86]. Our findings thus strongly suggests that the most likely source of degradation occurs at the cell level due to loss of passivation quality. Finally, Fig. 5.17 shows that $iV_{OC}$ does not vary significantly after annealing processes or degradation and a value of about 735 mV is obtained at 1 sun illumination for any lifetime measurement, which points at the little influence of the surface recombination on this solar cell parameter.

In order to experimentally quantify the change in surface passivation as a function of degradation, SRV temperature- and injection-dependence analysis was performed on the

samples based on TIDLS data acquired right after the first annealing process and at the end of the 28-months storage period according to Eq. 20. The former set was reported in section 5.3.3 and displayed in Fig. 5.14. From these results the two major recombination parameters could be assessed: In particular, a density of interface defect states $N_S$ of (6.5 ± 0.5) x $10^6$ $cm^{-2}$ and a fixed-charge density $Q_f$ of (1.5 ± 0.5) x $10^{11}$ $cm^{-2}$ were obtained. It has to be noted that the latter value is in good agreement with previously reported results for a-Si:H(i) [14], [92], whereas the determined $N_S$ value is orders of magnitude below the commonly accepted values for a device grade a-Si:H(i) passivation layer [96], [97], which proves the extremely good level of passivation obtained in our experiments.

The SRV analysis was then repeated based on TIDLS data acquired after a 28-months storage period. Figure 5.18 shows the surface recombination velocity as a function of temperature for the same three injection levels as in Fig. 5.14, i.e., 5 x $10^{14}$ $cm^{-3}$, 1 x $10^{15}$ $cm^{-3}$, and 1 x $10^{16}$ $cm^{-3}$, along with the fits obtained by applying the recombination model at the a-Si:H/c-Si interface [14]. The same fitting parameters and ratios used for the previous results were used to model these data with the exception of the neutral dangling-bond capture cross section ratio, $\sigma_p^0/\sigma_n^0$, which was found to yield better fits by changing to a value of 10. However, it must be noted that a fit of the data shown in Fig. 5.18 is still possible by keeping $\sigma_p^0/\sigma_n^0 = 20$, just like in the non-degraded case, but it generally leads to a poor goodness of fit of the data. This is especially true towards high temperatures, which could be explained by a temperature-dependence of the hole and electron neutral capture cross sections. Although at this point this is a mere hypothesis, this finding could provide valuable information regarding

the recombination mechanism of charge carriers at the dangling bonds and should be further investigated in the future.

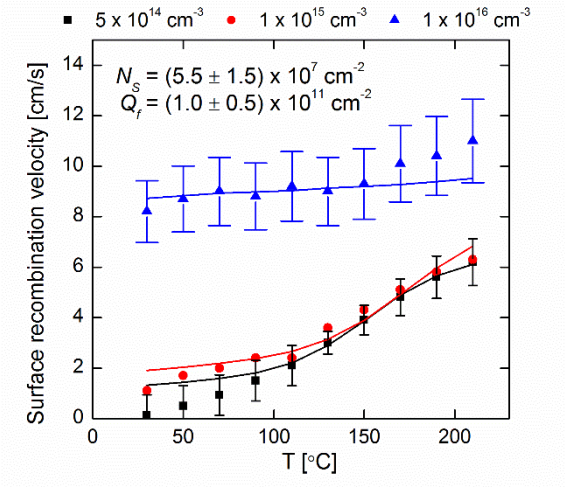


Fig. 5.18 Surface recombination velocity as a function of temperature for three different injection levels for a FZ *n*-type Si sample coated with a 50 nm-thick a-Si:H(i) layer (dots) from TIDLS data acquired after 28 months of storage in the dark along with the fits obtained by applying the model proposed by Olibet et al. [14] (solid lines). The error bars reported for the injection levels of 5 x $10^{14}$ $cm^{-3}$ and 1 x $10^{16}$ $cm^{-3}$ specify the uncertainty associated with the linear regression exemplified in Eq. 20.

As for the previous case, Fig. 5.18 shows that a good fit of the data could be obtained with a single fixed charge density, $Q_f$, of (1.0 ± 0.5) x $10^{11}$ $cm^{-2}$ for all injection levels. On the other hand, the modeling reveals that during the 28-months storage period the density of defect states at the interface, $N_S$, has increased by an order of magnitude, i.e., (5.5 ± 1.5) x $10^7$ $cm^{-2}$. This $N_S$ variation results in a strong SRV injection-dependence as, contrary to the results for the non-degraded samples shown in Figure 5.14, a strong increment of the surface recombination is found for $\Delta n$ = 1 x $10^{16}$ $cm^{-3}$ with SRV values significantly higher than in the low injection level range. However, even in this case a good fit of the data could be obtained with a single fixed charge density $Q_f$ of (1.0 ± 0.5) x $10^{11}$ $cm^{-2}$ for all injection levels. On the other hand, the modeling reveals that during the 28-months storage period the

density of defect states at the interface, $N_S$, has increased by an order of magnitude, i.e., (5.5 ± 1.5) x $10^7$ $cm^{-2}$. This result shows that, similarly to previous reports [76], [92], [98], the band bending at the interface has not changed during the degradation process, and the effective lifetime decay can be entirely ascribed to a worsening of the chemical passivation quality which led to an increased number of interface defect states. As the effective lifetime of the samples after the re-annealing process is not completely re-established but it is also higher than for the samples in the as-deposited state (see Fig. 5.17), we can attribute the increment of SRV shown in Fig. 5.18 to the concurrent partial effusion of hydrogen from the a-Si:H(i) layer and to the breakage of Si-Si bonds. The partial recovery of effective lifetime can thus be explained by the regeneration of the strained Si-Si bonds upon a new annealing process whereas the loss of hydrogen does not allow the complete re-establishment of the passivation quality. However, it must be noted that in terms of HJ technology reliability, the partial effusion of hydrogen poses a smaller threat to the performance of HJ modules over an extended period of time as it has been shown that the use of capping layers such as a-$SiN_x$:H can effectively prevent any effusion process [93]. The decay of surface passivation due to the breakage of Si-Si bonds may be more problematic as it is evidently impossible to carry out a thermal treatment of the a-Si:H(i) layer after module fabrication to regenerate the broken bonds. However, as pointed out by other authors, this effect could possibly be reduced by changing the thickness of the a-Si:H(i) layer thus reducing the amount of strain in the Si-Si bonds [14]. These findings effectively explain the results from recent reports showing a decrement of fill factor and an increasing series resistance for HJ systems [85]–[87] even for unweathered control modules [86], and firmly indicate the degradation of surface passivation

layer as a major candidate for the observed loss of solar systems performance over time. Strategies to avoid such degradation should be further investigated, including the usage of a capping layer to prevent the effusion of hydrogen, and the engineering of the a-Si:H(i) thickness to possibly reduce the strain of Si-Si bonds and avoid breakages over time.

## 5.4 Passivation by $Al_2O_3$

For the analysis of ALD deposited aluminum oxide we processed four samples with different thicknesses across the range of 190 – 265 µm using the chemical etching procedure described in section 3.2. After deposition of $Al_2O_3$ and the rapid thermal annealing processes described in sections 3.3.3 and 3.4, respectively, the samples were characterized via TIDLS measurements. The effective lifetime varying across a range of temperature from 25 ºC to 230 ºC for the 265 µm-thick sample is shown in Fig. 5.19.

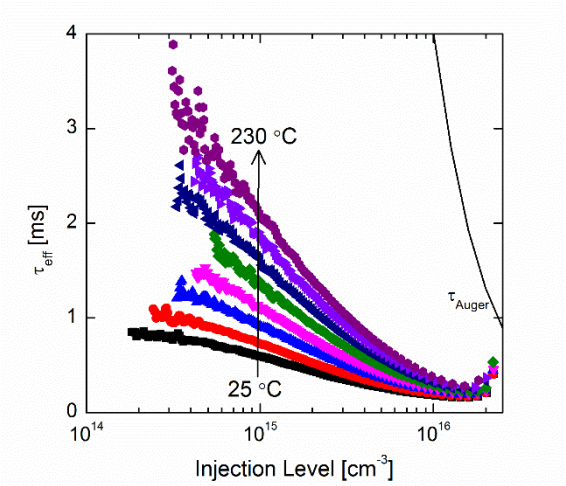


Fig. 5.19 Effective lifetime at different temperatures for the 265 µm-thick sample coated with $Al_2O_3$. Auger lifetime is reported for comparison.

To make sure that no structural variation occurred in the samples during the temperature scan, we measured the lifetime of the samples as the temperature was first increased from 25 ºC to 230 ºC and then decreased back to room temperature. The results are shown in Fig. 5.20 for three different injection levels.

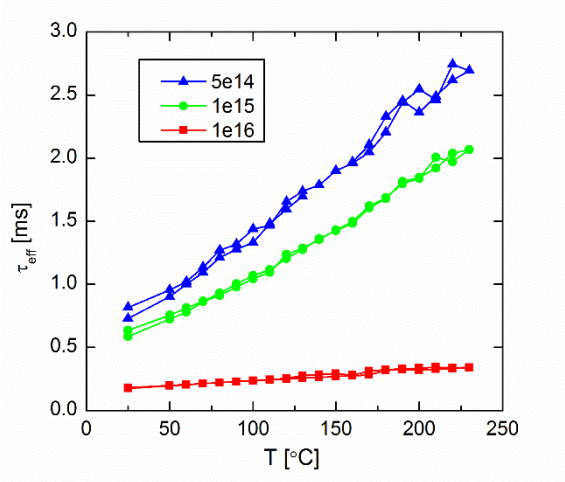


Fig. 5.20 Lifetime values for $Al_2O_3$-coated samples at three different injection levels as the temperature is first increased and then decreased in the range of 25 ºC – 230 ºC.

Clearly, no variation occurs during the entire temperature scan procedure with lifetime values perfectly matching at all injection levels as the temperature is increased and then decreased.

Following the thickness variation method described above (see Eq. 20), we were able to extract the surface recombination velocity at every injection level for each temperature. Figure 5.21 shows the SRV temperature- and injection-dependence for $Al_2O_3$-coated samples.

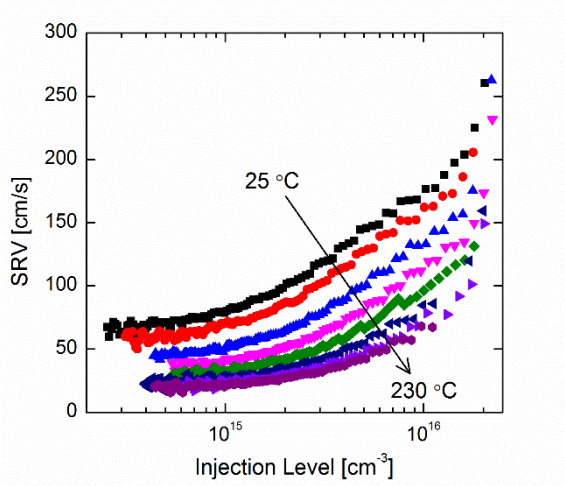


Fig. 5.21 Surface recombination velocity as function of injection level and temperature for $Al_2O_3$-coated Si samples.

SRV is found to increase with increasing injection level, a behavior which has been associated to the presence of charges in the passivation layer inducing a band bending at the interface [63]. Also, SRV is found to decrease with temperature, in accordance with the increasing effective lifetime seen in Fig. 5.19 and Fig. 5.20 for high temperatures. This trend can be better seen in Fig. 5.22 for three different injection levels.

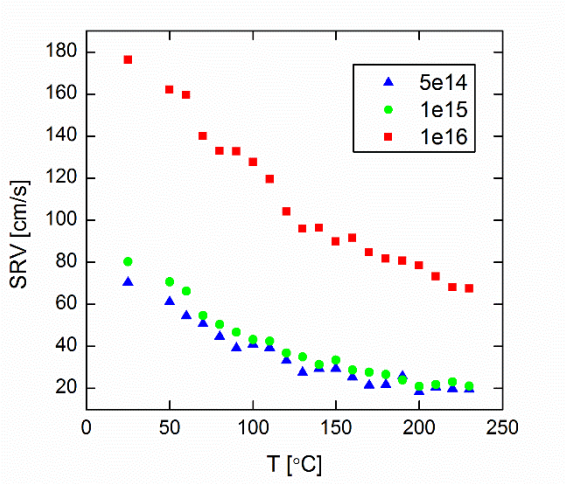


Fig. 5.22 Surface recombination velocity of $Al_2O_3$-coated samples at three different injection levels for different temperatures.

## 5.5 Passivation by $SiN_x$

### 5.5.1 Processing at ASU

For the analysis of PEVCD deposited $SiN_x$ we prepared four different samples according to the chemical etch processing described in section 3.2 with a thickness varying across the range from 170 to 260 μm. The samples were then coated on both sides according to the procedure reported in section 3.3.2 and subjected to a thermal annealing in a muffle furnace to activate the surface passivation layer.

All the samples were characterized via TIDLS technique for temperatures varying across the range from 25 ºC to 230 ºC. Figure 5.23 shows the results for the 260 μm-thick sample.

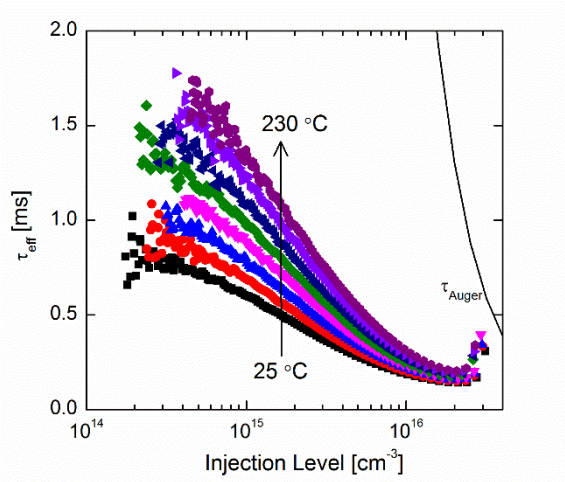


Fig. 5.23 Effective lifetime at different temperatures for the 260 μm-thick sample coated with $SiN_x$.

Similarly to the $Al_2O_3$-coated samples, lifetime was acquired as the temperature was first increased from 25 ºC to 230 ºC and subsequently decreased back to room temperature in order to assure that no permanent structural modifications were happening in the samples

because of the high temperatures. The results are shown in Fig. 5.24 for three different injection levels.

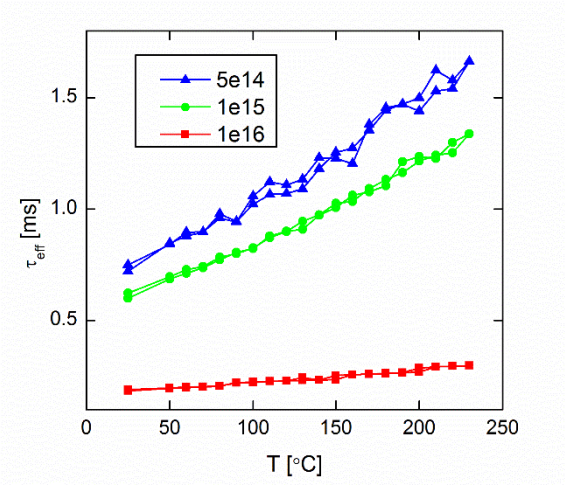


Fig. 5.24 Lifetime values for $SiN_x$-coated samples at three different injection levels as the temperature is first increased and then decreased in the range of 25 ºC – 230 ºC.

No significant variations occurred during the entire temperature scan procedure indicating that the samples were stable in the entire temperature range.

The measurement of all the four samples with different thickness allowed the extrapolation of the surface recombination velocity for these samples as exemplified by equation 20. The results are shown in Fig. 5.25.

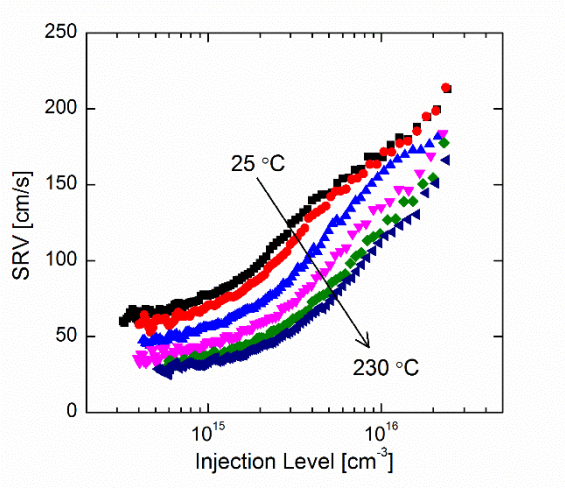


Fig. 5.25 Surface recombination velocity as function of injection level and temperature for $SiN_x$-coated Si samples.

Interestingly, $SiN_x$ presents a very similar temperature- and injection-dependence SRV as compared to the $Al_2O_3$ passivation layers. The decreasing SRV trend with increasing temperature can be better seen in Fig. 5.26 for three different injection levels.

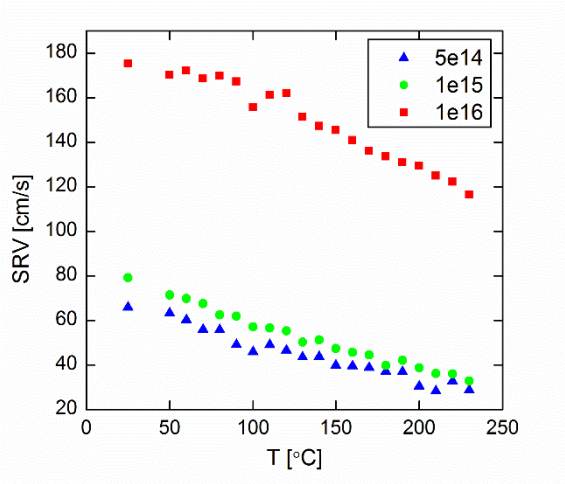


Fig. 5.26 Surface recombination velocity of $SiN_x$-coated samples at three different injection levels for different temperatures.

As previously mentioned, the strong injection dependence indicates the presence of fixed charge at the interface between c-Si and the dielectric layer [63]. As the charges contained in $SiN_x$ and $Al_2O_3$ have opposite sign, we could have expected different SRV trends with temperature among the two passivation schemes given that we are now in a regime of charges accumulation at the interface rather than inversion/depletion. However, for a more detailed analysis, the determination of the charge density at the interface for both $SiN_x$- and $Al_2O_3$-coated samples would be required.

### 5.5.2 Processing at UNSW

#### *5.5.2.1 Experimental*

The samples used in this section were processed according to the procedure described in section 3.2 to obtain a set of substrates with thicknesses ranging from 160 μm to 270 μm for both *p*- and *n*-type material. The substrates were then double-side coated with ~110 nm of $SiN_x$ via an industrial dynamic high-frequency (2.45 GHz) remote PECVD system (MAiA, Meyer Burger) at 425 °C [99]. The $SiN_x$-coated samples were then subjected to a damp heat testing in an environmental chamber (IEC 61216, 85 °C, 85% humidity) for 1000 hours in the case of *n*-type substrates, and 200 hours for *p*-type substrates.

To study the samples' electronic properties as a function of temperature and illumination conditions, the injection-dependent effective minority-carrier lifetime ($\tau_{eff}$) was measured using the Sinton Consulting WCT-120 instrument modified at the University of New South Wales (UNSW) described in Section 4.2 along with a standard version of the same tool at ASU for comparison [59]. Contactless corona C-V measurements were performed using a

PV metrology system from Semilab (PV-2000) described in Section 4.3. The fixed charge within the $SiN_x$ layer was determined to be in the range of (2-7)×$10^{12}$ $q$/$cm^2$, in agreement with values generally reported in literature for $SiN_x$ [100]–[103], whereas $D_{it}$ at midgap was found to be in the range (1.5±0.7)×$10^{12}$ $cm^{-2}$ $eV^{-1}$ at room temperature. Finally, surface photovoltage spectroscopy (SPS) is carried out on samples as-processed and after damp heat testing (IEC 61216, 85 °C, 85% humidity) for 1000 hours in the case of *n*-type substrates, and 200 hours for *p*-type substrates. The comparison of SPS results obtained from substrates coated with different passivation layers allows the identification of three different intra-gap defect states, which are univocally associated with the presence of dangling bonds at the interface. Furthermore, from the height of the peaks in the SPS, we could estimate the changes of defect density of states, $N_s$, due to different processing steps or due to the effect of damp heat testing.

*5.5.2.2 Modeling of Surface Recombination Velocity*

To reproduce the experimental results and to gain insights about the recombination mechanisms at the surface under different operating conditions, we made use of the extended version of the Shockley-Read-Hall (SRH) theory of recombination [36], [37], first proposed by Girisch *et al*. [104] and recently extended by Bonilla *et al*. [105] to account for the simultaneous variation of minority carrier injection and dielectric charge density. In these works, surface recombination ($R_s$) is expressed for an arbitrary trap level density function

$$R_s = \int_{E_v}^{E_c} \frac{(n_s p_s - n_i^2)}{\frac{[n_s + n_1(E)]}{v_{th} D_{it}(E) \sigma_p} + \frac{[p_s + p_1(E)]}{v_{th} D_{it}(E) \sigma_n}} dE \tag{24}$$

where $n_i$ is the Si intrinsic carrier density [38], [39], $v_{th}$ is the thermal velocity of both types of carriers, $\sigma_p$ ($\sigma_n$) are the capture cross sections for holes (electrons), $n_s$ and $p_s$ are the carrier concentrations at the surface defined as

$$n_s = (n_0 + \Delta n) exp\left(\frac{q\Psi_s}{kT}\right), p_s = (p_0 + \Delta p) exp\left(-\frac{q\Psi_s}{kT}\right) \quad (25)$$

where $\Delta n$ is the excess minority carrier concentration, $n_0$ ($p_0$) is the equilibrium electron (hole) carrier concentration, $k$ is the Boltzmann constant, $T$ is the temperature, and $\Psi_s$ is the surface potential that must be numerically calculated by solving the Poisson's equation in the band bending region [14], [106], [107]. To keep the model as simple as possible, we used a single defect at a single energy level $E_t$ in the midgap. Finally, $n_1$ and $p_1$ are the carrier concentrations for when the Fermi level falls to $E_t$

$$n_1 = n_i exp\left(\frac{E_t - E_i}{kT}\right),\ p_1 = p_i exp\left(\frac{E_i - E_t}{kT}\right) \quad (26)$$

By definition, the effective SRV calculated according to the Girisch model ($S_{Gir}$) is

$$S_{Gir} \equiv \frac{U_s}{\Delta n} = \frac{1}{\Delta n}\int_{E_v}^{E_c} \frac{(n_s p_s - n_i^2)}{\frac{[n_{tot}(E)]}{S_p} + \frac{[p_{tot}(E)]}{S_n}} dE \quad (27)$$

where $n_{tot}$ ($p_{tot}$) is the total density of electrons (holes) at the interface, and $S_p$ and $S_n$ are the energy dependent SRV for holes and electrons, respectively. However, as recently demonstrated by Bonilla *et al*. [105], SRV shows a marked lack of sensitivity on the energy dependence of $S_{p,n}$ and will then be considered energy independent in this work for simplicity.

As suggested by Dauwe *et al*. [100], an additional term accounting for enhanced recombination in a surface damage region (SDR) has to be included. This term can be described as a current loss over a shunt diode with a dark saturation current $J_{02}$

$$S_{J02} = \frac{J_{02}}{q\Delta n}\left[\left(\frac{\Delta n}{n_0}+1\right)^{1/m}-1\right] \tag{28}$$

where *m* is the diode ideality factor. The physical cause of the SDR is still under debate but is believed to form due to an excessive amount of hydrogen introduced during the surface preparation prior deposition and during the deposition itself [102], [108].

The effective SRV is then given by the equation

$$S_{eff} = S_{Gir} + S_{J02} \tag{29}$$

#### *5.5.2.3 TIDLS Results*

Figure 5.27 shows $\tau_{eff}$ versus injection level at different temperatures for the thickest *p*-type substrate sample ($W$ = 270 µm) passivated with $SiN_x$. Similar results were obtained for all samples in the *p*-type set with slightly lower lifetime values due to the reduced substrate thickness.

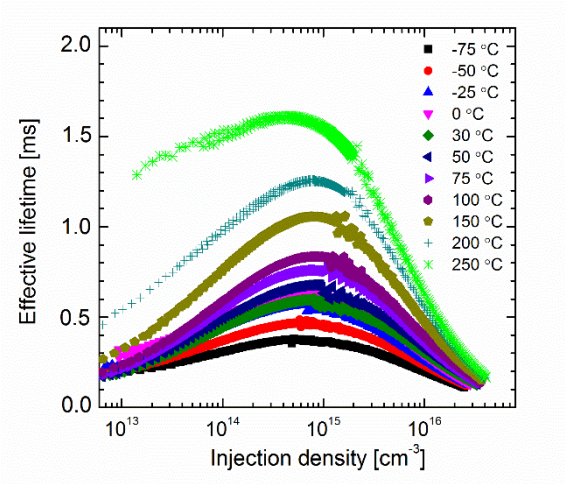


Fig. 5.27 Effective minority-carrier lifetime as a function of excess carrier concentration in a range of temperature of -75 °C – 250 °C for a high-quality *p*-type Si sample passivated with ~110 nm of $SiN_x$.

Lifetime is found to strongly decrease at low injection levels ($\Delta n < 5\times10^{14}$ cm$^{-3}$), a behavior which has previously been associated to the presence of a surface damage region [102], [109]. The impact of the SDR has been observed to be significant under an inverted or depleted c-Si surface, i.e., $SiN_x$-coated *p*-type substrates, due to the presence of a space charge region (SCR) where $n_s \approx p_s$ (assuming symmetric capture cross sections), whereas no influence was observed under accumulation conditions, i.e., $SiN_x$-coated *n*-type substrates [102], [109], [110]. However, it must be noted that the very existence of a SDR is still under debate as no experimental evidence has been reported in literature, and that other mechanisms such as recombination at the sample's edges have been proposed to explain the reduced lifetime at low injection level [110], [111].

Figure 5.28 shows the effective lifetime vs. injection level curves at different temperatures for the thickest *n*-type substrate sample ($W = 270$ µm) passivated with $SiN_x$.

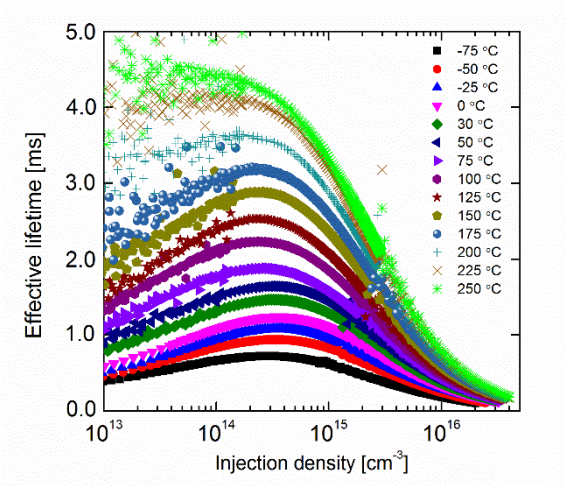


Fig. 5.28 Effective minority-carrier lifetime as a function of excess carrier concentration in a range of temperature of -75 °C – 250 °C for a high-quality *n*-type Si sample passivated with ~110 nm of $SiN_x$.

The effective lifetime values are generally higher for *n*-type samples than for the *p*-type ones, with the difference becoming more apparent at higher temperatures. Interestingly, $\tau_{eff}$ is still found to decrease towards low injection levels for temperatures below 200 °C in stark opposition with previous reports [109], [110].

In order to better understand these findings, we experimentally extrapolate the SRV in the whole temperature and injection density range from $\tau_{eff}$ measurements by applying the thickness variation method [63] according to Eq. 20. In this way, the recombination mechanisms happening in the bulk of the material can be separated from those happening at the interface c-Si/$SiN_x$.

Figure 5.29 shows the surface recombination velocity obtained using Eq. 20 for the $SiN_x$-coated *p*-type substrates at different temperatures as function of the injection level.

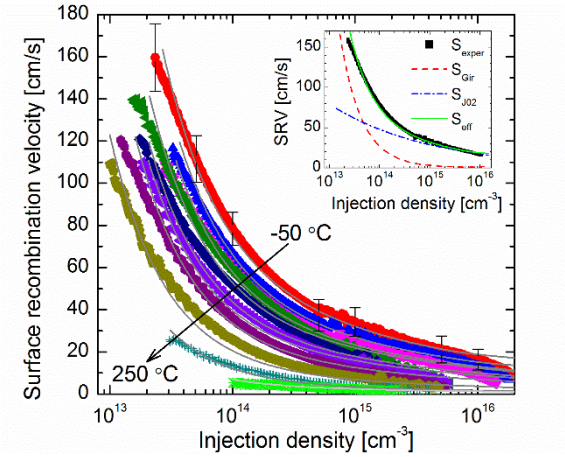


Fig. 5.29 Surface recombination velocity measurements and simulations (grey lines) as a function of excess carrier concentration at different temperatures in a range of -50 °C – 250 °C for high-quality *p*-type Si samples coated with ~110 nm of $SiN_x$. The inset depicts the curves at -50 °C calculated with the Girisch model ($S_{Gir}$, dash), the calculated contribution due to the recombination in the space charge region ($S_{J02}$, dash-dot), and the sum of the both which is the curve on top of the measured data points ($S_{eff}$, solid).

The SRV shows a strong temperature- and injection-dependence with the highest values found in the low temperature/injection level regime. As the temperature increases, SRV strongly decreases and its injection-dependence weakens significantly. The error shown for the measured data at -50 °C was estimated at each injection level from the quality of the linear fit expressed by Eq. 20 and was found to increase with excess carrier concentration from ±10% at $\Delta n = 2\times10^{13}$ cm$^{-3}$ to ±30% at $\Delta n = 1\times10^{16}$ cm$^{-3}$. As the temperature increases, the minimum injection level at which it is possible to extract the SRV shifts towards higher values due to the increasing scattering of lifetime data clearly observable in Fig. 5.28. The results shown in Fig. 5.29 correlate well with the lifetime temperature- and injection-dependence found for *p*-type $SiN_x$-passivated samples (see Fig. 5.27). Figure 5.29 also shows the simulated $S_{eff}$ (grey lines) given by Eq. 29 throughout the whole temperature range. As the inset clearly depicts for the experimental data at -50 °C, the measured data can be successfully modeled by the sum of the contribution calculated with the Girisch model given

by Eq. 27, and the contribution due to the recombination in the SDR given by Eq. 28 with the latter dominating in the high injection regime ($\Delta n > 5\times10^{15}$ cm$^{-3}$). The same holds true for the experimental data of the remaining temperature range. Remarkably, the only parameters that had to be adjusted in the model to account for the temperature variation were: $D_{it}$ in Eq. 27 and $J_{02}$ in Eq. 28. It's also worth highlighting that a satisfactory fitting of the SRV *T*-dependent data could not be achieved by mean of the Girisch model alone and that the addition of a recombination term represented by $J_{02}$ due to the presence of the SDR was crucial. Thus, on the contrary of previous studies reporting no surface damage for samples coated by mean of remote PECVD systems [112], our findings prove that a SDR is present at the c-Si/$SiN_x$ interface of these samples, in agreement with later reports [101].

Figure 5.30 shows the SRV obtained using Eq. 20 for the $SiN_x$ coated *n*-type substrates at different temperatures as function of the injection level.

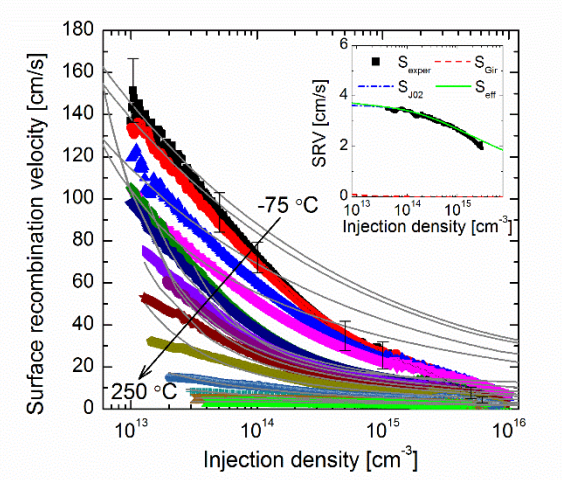


Fig. 5.30 Surface recombination velocity measurements and simulations (grey lines) as a function of excess carrier concentration at different temperatures in a range of -75 °C – 250 °C for high-quality *n*-type Si samples coated with ~110 nm of $SiN_x$. The inset depicts the curves at 250 °C calculated with the Girisch model ($S_{Gir}$, dash), the calculated contribution due to the recombination in the space charge region ($S_{J02}$, dash-dot), and the sum of the both which is the curve on top of the measured data points ($S_{eff}$, solid).

Although generally lower than the SRV results shown in Fig. 5.29 for *p*-type substrates, the measured SRV for *n*-type samples shows a similar behavior with a strong temperature- and injection-dependence. Similar to the previous case for *p*-type samples, the error associated with the measured data for *n*-type samples was found to increase with excess carrier concentration from ±10% at $\Delta n = 2\times10^{13}$ cm$^{-3}$ to ±35% at $\Delta n = 1\times10^{16}$ cm$^{-3}$. The same set of parameters used for *p*-type samples were used to fit the measured data for *n*-type substrates shown in Fig. 5.30 (grey lines). Again, only $D_{it}$ and $J_{02}$ were adjusted to account for the temperature variation. However, measured SRV data in the range of temperature of -75 °C – 0 °C showed a significantly different trend with increasing injection level when compared to the rest of the experimental results that could not be satisfactorily reproduced by our simplified model. The origin of this finding cannot be adequately interpreted at the moment and further investigation is required.

The generally lower $S_{eff}$ for *n*-type samples when compared to *p*-type substrates (see Figs. 5.29 and 5.30 for comparison) was found to be due to a lower contribution coming from the surface damage region $S_{J02}$. This could be expected as for *p*-type samples the SDR lies directly within a space charge region where according to SRH theory the recombination rate has its peak due to the electrons and holes having the same concentration. Nonetheless, as shown in the inset in Fig. 5.30 for data at $T$ = 250 °C, at high temperatures the measured SRV for *n*-type substrates is completely dominated by the $S_{J02}$ term (dash-dot line in inset of Fig. 5.30). This is due to the simultaneous strong decrement of the $S_{Gir}$ term along with the increment of holes concentration at the surface caused by thermal excitation. Under these conditions, the density of electrons and holes at the surface is almost at equilibrium and the

recombination rate in the SDR is enhanced. This result further suggests that a surface damage region is present at the c-Si/$SiN_x$ interface even for *n*-type samples but that its contribution becomes apparent only when the surface is not under strong accumulation conditions, e.g., at high temperatures.

Under most of the experimental conditions examined in this work, for both *p*- and *n*-type samples the concentration of electrons at the interface is higher than the concentration of holes due to the presence of positive fixed charges in the dielectric, and $S_{Gir}$ expressed in Eq. 27 is usually more sensitive to the variation of $S_p$ rather than of $S_n$. Thus, using the experimental $D_{it} = 1.5\times10^{12}$ $cm^{-2}$ $eV^{-1}$ obtained via C-V measurement and the expression $\sigma_p = S_p / v_{th}D_{it}$ we can directly estimate the capture cross section for holes as $\sigma_p \sim 10^{16}$ $cm^{-2}$. However, with increasing temperature the c-Si surface of the *p*-type samples goes from being under inversion conditions, i.e., $n_{tot} > p_{tot}$, to accumulation conditions, i.e., $n_{tot} < p_{tot}$, due to thermal excitation. Thus, the modeling of experimental data at high temperatures of *p*-type becomes sensitive to the variation of $\sigma_n$ which was estimated as $\sim 10^{14}$ $cm^{-2}$, corresponding to a capture cross section ratio $k \sim 100$. These values are consistent with one of the defects previously measured by Schmidt *et al*. [113] via small-pulse deep-level transient spectroscopy (DLTS) denominated defect "B" associated to the presence of dangling bonds at the interface [112]–[114]. As previously stated, the fitting of measured SRV data for *p*- and *n*-type substrates at different temperatures required the variation of only two parameters, i.e., $D_{it}$ and $J_{02}$.

Figure 5.31 shows both $D_{it}$ (full symbols) and $J_{02}$ (empty symbols) as a function of temperature for *p*- and *n*-type substrates obtained from the fitting of the experimental results.

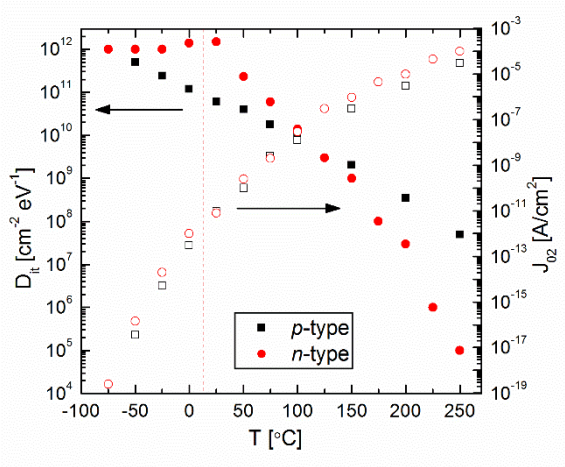


Fig. 5.31 Density of defect states at the interface $D_{it}$ and diode saturation current $J_{02}$ as function of temperature for both *p*- and *n*-type substrates. The vertical dashed line indicates the temperature range at which a good fit of the experimental SRV data for *n*-type substrates could not be obtained.

The density of defect states at the interface $D_{it}$ is generally found to decrease exponentially with increasing temperature for both types of substrate. However, while for *p*-type substrates the decreasing trend is consistent throughout the whole temperature range, for *n*-type samples a stable $D_{it}$ value of (1.0–1.5)×$10^{12}$ cm$^{-2}$ eV$^{-1}$ is obtained for temperatures across -75 °C – 0 °C (see vertical dashed line in Fig. 5.31). This temperature range corresponds to the one in which the experimental SRV data could not be properly fitted (see Fig. 5.30), possibly indicating that the simplified model adopted in this work is not adequate under these particular conditions. Despite this delayed onset, $D_{it}$ is found to be much lower for *n*-type samples at high temperatures as the rate of change vs. *T* is steeper than for *p*-type material. These findings can be explained by the shift of Fermi energy towards midgap with increasing temperature and the reported amphoteric nature of defect states at the interface [50], [115]. In fact, similarly to what other reports have suggested for the Si-$SiO_2$ interface [105], [116]–[118], we can make the reasonable assumption of considering the defect states

close to the valence band of donor-type, and those close to the conduction band of acceptor-type. In this way, the shift of Fermi energy due to the increment of intrinsic carriers density with temperature would lead to a reduction of active defect states for both *p*- and *n*-type substrates. The $D_{it}$ curves in Fig. 5.31 then provides information about the characteristic energy distribution of interface defect states in both halves of the bandgap. In order for this interpretation to be valid, we also need to assume the capture cross section for holes and electrons to be temperature-independent. This assumption has been proven true for the Si-$SiO_2$ interface [116] However, as no experimental results have been reported regarding the Si-$SiN_x$ interface, further investigation is required to confirm this hypothesis.

Figure 5.31 also shows the diode saturation current $J_{02}$ to have comparable values for *n*- and *p*-type substrates, and to strongly increase with temperature for both substrates. This behavior is expected since the saturation current depends on $n_i$ [119], which is strongly dependent on temperature due to the thermal excitation. Remarkably, despite the significantly different contribution given to the effective SRV by the $S_{J02}$ term on *p*- and *n*-type substrates for the reasons stated above, very similar $J_{02}$ values are obtained when modeling $S_{eff}$ data which suggest a similar SDR impact for both sets of samples and is in line with the idea that the origin of this region comes from the plasma source during the deposition process.

These findings indicate that, even when a high amount of defect states at the interface are present, their impact on the surface recombination decreases with temperature, thus possibly yielding some benefits to the overall device performance under field operation conditions. This is the opposite of what we showed for a-Si:H in section 5.3 and recently reported in Ref.

[18], and may represent a significant advantage for technologies adopting $SiN_x$ as a passivation layer. However, at least for industrial PECVD systems, these results demonstrates that a surface damage region is introduced at the interface c-Si/dielectric material even for remote high-frequency conditions. Its contribution to the overall surface recombination was found to be significant not only under inversion conditions, but also under accumulation conditions, especially at high temperatures. As the exact nature of this region has not been identified yet, both theoretical and experimental investigations are still required to further develop the quality of the passivation provided by $SiN_x$ layers for high-efficiency solar cells architectures.

#### *5.5.2.4 SPV Analysis*

Figure 5.32 shows the SPS spectrum for a high-quality FZ *n*-type sample passivated with $SiN_x$ before and after degradation via damp heat testing.

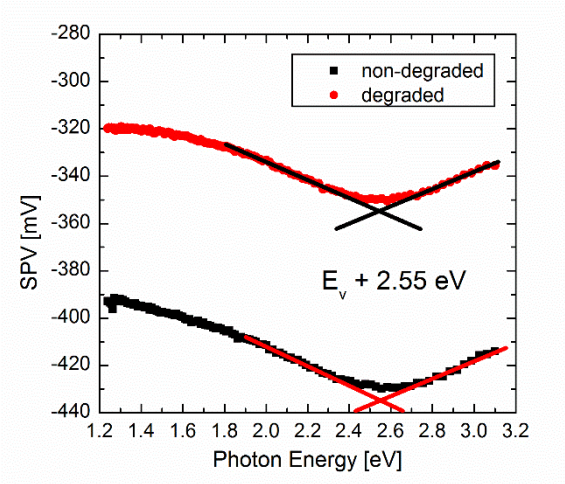


Fig. 5.32 Surface photovoltage spectroscopy results on a high-quality *n*-type sample passivated with $SiN_x$ both before and after being subjected to a damp heat testing (IEC 61216, 85 °C, 85% humidity, 1000 hours).

The SPS signal for *n*-type samples coated with $SiN_x$ does not show the same features in the low energy regime as for the samples passivated with a-Si:H (see Fig. 5.7 for comparison). Only one slope variation is observed at $E_v$ + 2.55 eV, which is associated with the bandgap of the dielectric material. This is due to the sample surface being under accumulation conditions due to the presence of positive fixed charges in the dielectric material which prevents the SPV signal to be collected as exemplified by E. Fefer and Y. Shapira [13]. Interestingly, the intensity of the signal is found to increase after the damp heat testing indicating a decrement of the defect states density at the interface. Although this finding is counterintuitive, as one would expect degradation to act the opposite way, the observation is supported by photoconductance lifetime measurements on the sample before and after damp heat testing, which confirms that the sample electrical properties have improved. However, this result is not well understood at this point and further investigation will be required.

Figure 5.33 presents the SPS spectrum for a high-quality FZ *p*-type sample passivated with $SiN_x$ before and after degradation via damp heat testing.

On the contrary of the results shown in Fig. 5.32 for *n*-type samples passivated with $SiN_x$, the SPS signal intensity strongly decreases after damp-heat testing. The analysis of *p*-type substrates reveals the presence of four slope variations in the energy region below the dielectric material bandgap which, similarly to the *n*-type samples, has an energy value of $E_v$ + 2.7 eV.

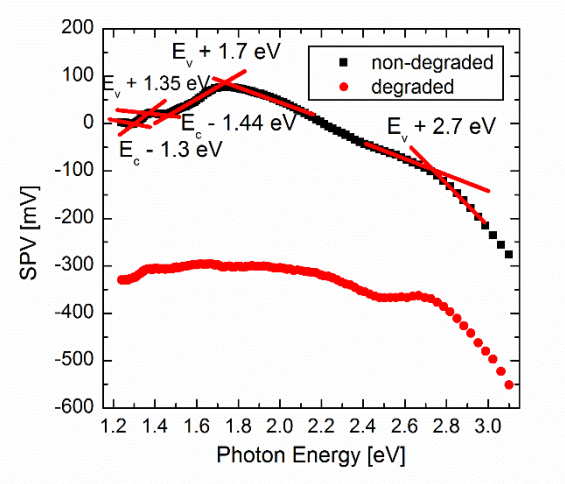


Fig. 5.33 Surface photovoltage spectroscopy results on a high-quality *p*-type sample passivated with $SiN_x$ both before and after being subjected to a damp heat testing (IEC 61216, 85 °C, 85% humidity) for 200 hours.

Remarkably, three of these four features highlighted in Fig. 5.33 were also observed for a-Si:H-coated samples shown in section 5.3.1 (see Fig. 5.7 for comparison). This finding confirms that the identified defect states are associated with the c-Si/passivation layer interface and are not due to the particular material used. However, compared to a-Si:H-coated samples, we now have the appearance of a fourth feature exactly where the transition associated with the a-Si:H bandgap was found, i.e., $E_v$ + 1.7 eV.

# 6 BULK LIFETIME ANALYSIS

## 6.1 Experimental Results

The correct assessment of the bulk lifetime of silicon material under varying experimental conditions is a major task in the photovoltaic community as invaluable information can be obtained from its analysis. However, due to the increasing quality of the silicon obtained in the crystallization process, some of the most well-established characterization technique such as deep-level transient spectroscopy (DLTS) are reaching their sensitivity limits and are not capable of detecting the metal impurities contained in the material. On the contrary, it has been shown that temperature- and injection-dependent lifetime spectroscopy (TIDLS) has the potential to detect extremely low concentrations of metal impurities but its application may be limited by other recombination mechanism overshadowing the contribution coming from the bulk.

In this work, thanks to the experimental temperature- and injection-dependent SRV results presented in Chapter 5, we demonstrate that a concentration of metal impurities down to $10^9$ $cm^{-3}$ can be detected via TIDLS measurements thus proving that this technique has the potential to investigate Si material for high-efficiency PV applications. In order to do so, we need to remove the contribution of the surface recombination velocity from the measured effective lifetime as expressed by Eq. 20. Figure 6.1 shows this procedure for samples passivated with only a-Si:H(i) (top) or with a stack of a-Si:H(i)/a-Si:H($n^+$) (bottom) described in the previous chapter.

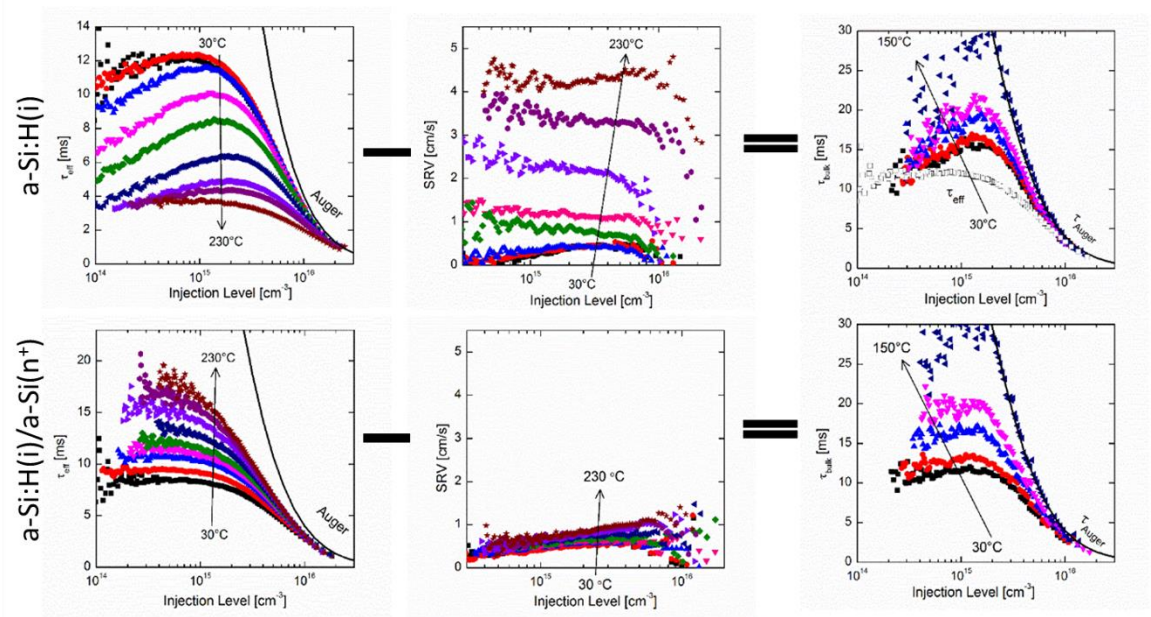


Fig. 6.1 Extrapolation of bulk lifetime from effective lifetime and SRV measurements obtained by applying Eq. 20 to samples passivated with only a-Si:H(i) (top) or with a stack of a-Si:H(i)/a-Si:H($n^+$) (bottom) presented in Chapter 5.

Figure 6.2 shows the resulting bulk lifetime vs. injection density curve for increasing temperatures obtained for a-Si:H(i)-coated FZ samples. These data are calculated starting from the TIDLS data shown in Fig. 5.4 from which we subtracted the SRV contribution shown in Fig. 5.6 according to Eq. 20. Figure 6.2 also shows the effective lifetime $\tau_{eff}$ at 30 °C to showcase the impact of the SRV on the lifetime measurement. The comparison of $\tau_{eff}$ and $\tau_{bulk}$ at 30 °C shows that the latter exhibit even a stronger injection-dependence. Furthermore and more importantly, the *T*-dependence is now completely reversed compared to the effective lifetime shown in Fig. 5.4, and $\tau_{bulk}$ is found to increase with temperature as it would be expected from the exponential temperature dependence of the SRH density $p_1$ in Eq. 11.

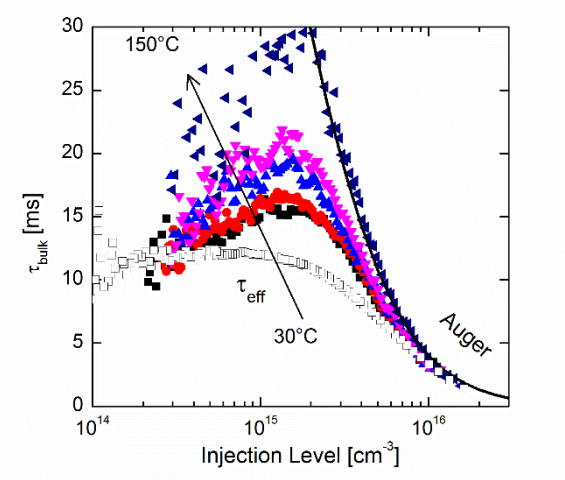


Fig. 6.2 Bulk lifetime as function of injection level at temperatures with 20 °C step size up to 150 °C for samples passivated with a-Si:H(i). $\tau_{eff}$ at room temperature (empty squares) is reproduced for comparison.

Interestingly, bulk lifetime is found to perfectly match the Auger limit at 150 °C while any curve at higher temperature (shown in Chapter 7) are found to sit beyond that limit. This is probably due to the uncertainty of the Auger recombination coefficient at high temperatures as mentioned at the beginning of this discussion. In the next section we will show that the discrepancy between $\tau_{eff}$ and $\tau_{bulk}$ is of the utmost importance for the correct identification of deleterious defects in the bulk of high-quality Si material.

Similarly to the analysis performed on a-Si:H(i)-coated samples, we experimentally evaluated the bulk lifetime on the samples after the additional deposition of *n*-doped a-Si:H. The bulk lifetime resulting from the application of Eq. 20 on the TIDLS data is shown in Fig. 6.3. As we would expect from the significantly lower SRV shown in Fig. 5.12, the resulting bulk lifetime is not as different from the $\tau_{eff}$ data shown in Fig. 5.10 as for the a-Si:H(i)-coated samples. This can be seen from a comparison with the effective lifetime at 30 °C also included in Fig. 6.3.

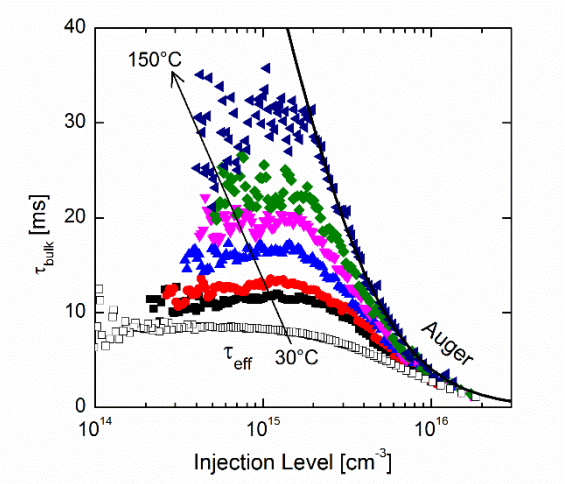


Fig. 6.3 Bulk lifetime as function of injection level at different temperatures with 20 °C step size up to 150 °C for samples passivated with a-Si:H(i)/a-Si:H($n^+$). $\tau_{eff}$ at room temperature (empty squares) is reproduced for comparison.

Remarkably, the results are very similar to those shown in Fig. 6.2 which corroborates the validity of this method for $\tau_{bulk}$ extrapolation provided that a consistent experimental approach is adopted. Again, the bulk lifetime is found to match the Auger limit at 150 °C. All curves at temperatures higher than 150 °C fall to the right side of the Auger limit shown in Fig. 6.3 and are discussed in the subsequent chapter.

## 6.2 Defect Parameters Contour Mapping

In this section we introduce a method we denominate defect parameters contour mapping (DPCM) which can be used to complement a TIDLS analysis to quickly assess the most likely lifetime-limiting defect in PV silicon samples. The DPCM method builds upon the framework presented by S. Rein [17] and provides a more general, visual, and intuitive way to analyze lifetime spectroscopy data. The main characteristics of the DPCM are: 1) it can be used with any set of LS data disregarding the experimental ranges of injection levels and

temperatures available, and 2) it allows to visually compare among defects previously reported in literature to readily identify the most likely lifetime-limiting one. This is particularly useful for the case when the source of contamination is unknown. Alongside, when applied to our experimental data, this analysis experimentally proves that the generally accepted assumption $\tau_{eff} \approx \tau_{bulk}$ doesn't hold for high-quality material and that a direct measurement of SRV as function of temperature- and injection is required if one wants to evaluate the quality of the bulk.

In this work we will make use of the advanced parameterization proposed by Richter *et al*. [19] for the intrinsic recombination in crystalline silicon. However, it must be noticed that the *T*-dependence of the parameters we will make use to model these processes have been experimentally determined for a window of injections and temperatures narrower than the one considered here. In particular, the radiative recombination coefficient $B(T)$ has only recently been evaluated to a temperature up to 90 °C [120]. The results were found to agree well with the previously established data published by Trupke *et al*. [121], on which our analysis is based, as $B(T)$ values at higher temperatures were extrapolated from a parameterization of data reported in that work. Similarly, Auger recombination *T*-dependence has not been extensively studied. Recently Wang *et al*. evaluated the ambipolar Auger coefficient $C_a$ across a temperature range from -30 to 200 °C [122] but only at a very high injection level of 5 x $10^{16}$ $cm^{-3}$. Based on this we expect some discrepancy between our modeling and the experimental results and thus higher errors at temperatures above 100 °C.

Herein, we will first apply the DPCM method to the experimental effective lifetime results obtained for a-Si:H(i) coated samples and the resulting $\tau_{bulk}$ shown in the previous

paragraph. Subsequently, we will discuss in depth these two main characteristics of the model and lay out the main advantages and limitations of the method when compared to other approaches. We use the DPCM to revisit two relevant sets of experimental data from case studies previously reported in literature – this not only demonstrates its capability to complement other analysis but it also reveals invaluable information otherwise inaccessible. Finally, we will evaluate the DPCM response to a set of data obtained by simulating the presence of a defect level in a low resistivity *p*-type silicon sample. By varying the size of injection level and temperature data ranges fed to the DPCM analysis we will identify the ideal conditions for its application.

The DPCM method makes use of the SRH theory for a single defect level along with the advanced parameterization for intrinsic recombination proposed by Richter *et al*.[20] to model the lifetime vs. injection level curves at different temperatures. The defect energy level $E_t$ and $k$ are varied across a wide range of values, i.e., the parameters space. In order to do so, our main assumption is that lifetime is dominated by just one defect level in the whole range of temperature evaluated. At the beginning, the experimental lifetime vs. injection level curve at RT is evaluated and a best fit is obtained for every ($k$, $E_t$) combination by varying the time constants $\tau_{p0}$ and $\tau_{n0}$.

The quality of the fit, represented by lighter color in the contour plot, is determined by calculating an *Average Residual Value* (%) over various injection levels according to the equation

$$Average\ Residual\ Value\ (300\ \mathrm{K}) = \left( \sum_{i=1}^{n} \frac{\left| \tau_{measured,j} - \tau_{model,j} \right|}{\tau_{measured,j}} \right) / n \qquad (30)$$

where $n$ is the number of injection level values at which the fit is evaluated, $\tau_{measured}$ can be either the effective lifetime or the bulk lifetime, and $\tau_{model}$ is obtained according to the procedure explained in Section 6.1. In Fig. 6.4 this calculation is exemplified for an experimental lifetime curve (black dots) and a simulated curve (red line). The distance between the two curves is evaluated at different injection levels indicated by the green arrows and is then averaged in the ARV calculation.

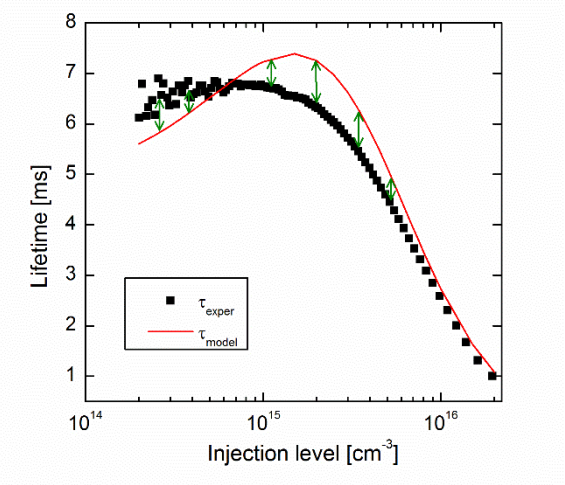


Fig. 6.4 Experimental lifetime vs injection level curve for a metal-contaminated FZ $n$-type wafer (black dots). The red curve represents the modeling obtained using the SRH theory and Richter parameterization [1]. The distance between the two is evaluated at different injection levels (green arrows) and is represented by the ARV.

Normally $\Sigma(\tau_{measured} - \tau_{model})^2$ is minimized when fitting lifetime with SRH model. However, when the lifetime crosses several orders of magnitudes this method unintentionally allocates larger weight to the higher-value lifetime data. To avoid this problem, $\Sigma[|\tau_{measured}-\tau_{model}|/\tau_{measured}]$ was used in this work. Furthermore, taking the absolute value of $\tau_{measured}-\tau_{model}$ instead of the square value enables the assessment of a true modeled-to-measured residual percentage.

### 6.2.1 DPCM Applied to Experimental Data

To apply the DPCM method to our experimental data we need first to choose the number of injection levels to be compared. Note that the values can be modified to account for characteristic features in the lifetime curve at a certain injection level which could help obtain a more univocal fit. However, as our experimental lifetime curves reported in Fig. 5.4 and Fig. 5.10 don't show any particularly relevant feature along the whole injection range, for this case we simply choose five values evenly spaced across 5 x $10^{14}$ $cm^{-3}$ – 1 x $10^{16}$ $cm^{-3}$. Once the time constants associated with the best fit have been assessed at room temperature, i.e. $\tau_{p0}$ (25 ºC) and $\tau_{n0}$ (25 ºC), they are kept fixed and subsequently employed to evaluate the fit over four more different temperatures over the range 30 °C – 150 °C. The *Average Residual Value* is calculated for each of the lifetime curve associated with a certain temperature and then averaged again as shown in Eq. 31.

$$Average\ Residual\ Value = \sum_{j=1}^{m}\left(\left(\sum_{\mathrm{i}=1}^{n}\frac{\left|\tau_{measured,j}-\tau_{model,j}\right|}{\tau_{measured,j}}\right)/n\right)/m \qquad (31)$$

where *m* is the number of temperatures taken into account.

We acknowledge that keeping the time constants fixed for different temperatures is equivalent to suggest that $\sigma_p$ and $\sigma_n$ – and thus *k* – are *T*-independent, which for many metal impurities in silicon is not the case. However, we can account for this temperature dependence by associating an error to the *k* value reported for every known defect level. In this way we can still present the results of the whole TIDLS data fitting in a single plot which is the main goal of the DPCM method. Note that in order to accurately estimate the error

associated with the temperature dependence of $k$, both $T$-dependence for $\sigma_p$ and $\sigma_n$ needs to be known – something that is available only for a very few defects. Based on the $T$-dependence of $\sigma_{n,p}$ associated with various capture mechanisms reported by S. Rein [17] and K. Graff [123], and given the limited $T$ range taken into account, we can estimate this error to be at maximum 60% for the case of iron. This number will of course vary substantially with the metal of interest.

In Fig. 6.5 and Fig. 6.6 the metal defects with well-established parameters' values taken from [17], [56], [57], [123]–[129] are depicted on the graph enabling us to readily verify which ones among these defects are the most likely to represent the source of recombination within the bulk of the material. The list of defects shown in the contour plot could be easily updated should new defects' parameters be established.

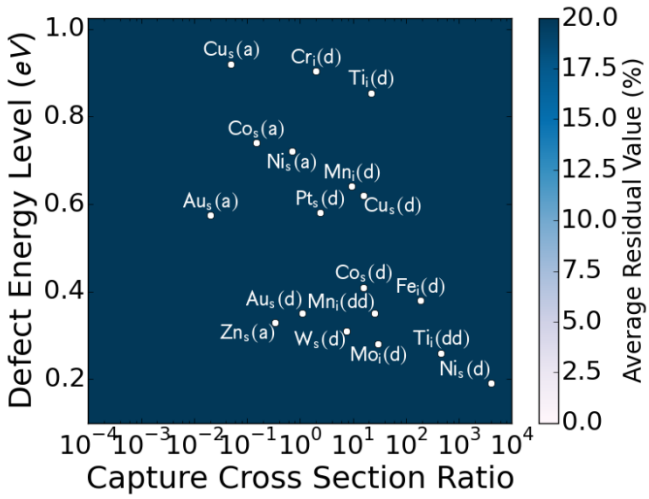


Fig. 6.5 Contour plot showing the quality of the fit for τeff data of a-Si:H(i) coated samples averaged over five different temperatures across a range from 30 °C to 150 °C.

In Fig. 6.5 we show the contour plot obtained following the procedure described above for the effective lifetime, $\tau_{eff}$, data of samples coated with a-Si:H(i) shown in Fig. 5.4. It

appears immediately that there are no $E_t$ and $k$ combinations for which a good fit quality is obtained as the *Average Residual Value* is always above the value of 18%.

The situation changes substantially when we repeat the procedure using the bulk lifetime data shown in Fig. 5.10 (or similarly data shown in Fig. 6.3). Some characteristic bright areas appear in the corresponding contour plot shown in Fig. 6.6 with an *Average Residual Value* below 11% which can be considered as an acceptable fit considering the errors associated with the measurement method [130] and uncertainties in the models employed. A 60% error is shown for the $k$ value of $Fe_i(d)$ as a representative for the uncertainty of defect levels due to its temperature dependence. It seems clear from Fig. 6.6 that even when accounting for such a high level of uncertainty associated to the $k$ value our method is still accurate enough to discriminate among different defect levels.

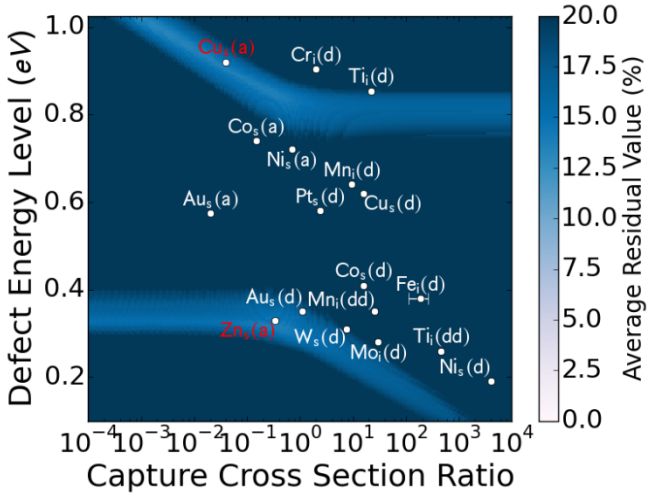


Fig. 6.6 Contour plot showing the quality of fit for $\tau_{bulk}$ averaged over five different temperatures across a range from 30 °C to 150 °C. Defects for which the best fit is obtained are shown in red. An error of 60% is shown for $Fe_i(d)$ as a representative for the uncertainty associated with the $k$ values of defect level due to its temperature dependence.

As expected, the ($k$, $E_t$) solutions resulting in a good fit are symmetric for $k$ values close to unity since defects with an energy level at the same distance from either the valence or the conduction band have virtually the same recombination strength [17]. The bright area in the upper half of the bandgap becomes $E_t$ space-independent when $k > 1$, i.e. $\sigma_n > \sigma_p$, since all the electrons accessible by the defect level are already made available and any further increment of $\sigma_n$ does not correspond to an increment in the recombination strength. The same explanation holds for the $E_t$ space-independent bright region seen in the lower half of the bandgap for holes when $k < 1$, i.e. $\sigma_n < \sigma_p$.

Given the narrowness of the bright areas, we can shrink the list of possible harmful defects among those reported on the graph to just one defect in the lower half of the bandgap and one in the upper half, respectively the single acceptor state of $Zn_s$ and the single acceptor state of $Cu_s$ (shown in red in Fig. 6.6). Thanks to the knowledge of $\tau_{p0}$ from the modeling and using the hole capture cross sections, $\sigma_p$, reported in [56] and [126] for these defects we can calculate the defect density $N_t$ from Eq. 12 using thermal velocity $v_{th}$ = 2.1 x $10^7$ cm/s. For the $Zn_s$ defect we obtained an $N_t$ of 1.4 x $10^9$ $cm^{-3}$. For the $Cu_s$ defect we obtained an $N_t$ of 1.6 x $10^{10}$ $cm^{-3}$. In an attempt to verify the $E_t$ level of the defect of interest we analyzed the samples with deep-level transient spectroscopy (DLTS) which is accepted to be one of the most sensitive methods for characterization of electrically active defects. In particular, DLTS is known to be sensitive to a concentration of defects above $10^{12}$ $cm^{-3}$ for samples with a doping level of ~$10^{15}$ $cm^{-3}$. However, no impurities were detected in our specimens which further corroborates the extraordinary sensitivity of the TIDLS method. While copper's harmful effect has been previously assessed [123], [126] and its presence in silicon would not

be surprising, zinc has been thought to be an innocuous impurity in device fabrication as its low evaporation temperature – lower than its melting temperature – makes it evaporate during heat treatments of the wafers so that it has never been found in the bulk of processed samples but only on polished surfaces of as-received material [123]. Our results suggest that a small concentration of zinc could actually be present in the bulk of high-quality c-Si and contribute to the detrimental recombination mechanisms.

It must be noticed that, although at room temperature a very good fit of the experimental bulk lifetime is obtained by modeling with only one defect's parameters, things could be different at higher temperatures where other defects can get activated due to the shift of Fermi energy in the Si bandgap resulting in a higher ARV.

Finally, we want to point out that an overall best fit of the experimental results could be obtained by replacing the Richter parameterization with a more complex model accounting for the Auger temperature dependence demonstrated in Chapter 7. Such a model, however, would probably not change the results associated with the search of the lifetime-limiting defect as every ($E_t$, $k$) combination is equally affected by the parameterization of $\tau_{Auger}$ being $T$-independent, but would simply lower the ARVs on the entire map.

### 6.2.2 DPCM Applied to IDLS Data

We first apply the DPCM method to a set of IDLS data which represents the simplest possible experimental scenario as the $T$-dependence of the physical parameters evaluated is not taken into account. In particular, we will consider the work of Sun *et al*. [15] in which the authors present a study of the aluminum-oxygen (Al-O) recombination center parameters in

*n*- and *p*-type Czochralski-grown silicon. The aluminum-oxygen center has been extensively studied via deep level transient spectroscopy (DLTS) in the past and $E_t$ has been assessed to lay in the range of $E_t = E_v + (0.38 – 0.50)$ eV whereas *k* values reported in literature span over orders of magnitudes [131], [132]. The report from Sun *et al*., however, stands out as it makes use of both control, i.e., non-contaminated, and intentionally contaminated wafers which allows to extract the lifetime contribution of Al-O complexes ($\tau_{Al\text{-}O}$) from the minority carrier effective lifetime ($\tau_{eff}$). This is obtained by applying the equation $1/\tau_{Al\text{-}O} = 1/\tau_{eff} - 1/\tau_{control}$ where $\tau_{control}$ is the lifetime measured for the control wafers. By taking this precaution, i.e., analyzing $\tau_{Al\text{-}O}$ rather than $\tau_{eff}$, Sun *et al*. revealed that a single deep level is sufficient to successfully model the experimental data for both *p*- and *n*-type samples in stark opposition with previous reports where the existence of multiple defect levels had been postulated. Furthermore, they are able to determine the optimal *k* value of this defect level being 380 and the uncertainty range associated with it as 330-460. In their study, however, the authors are able to draw these conclusions only by assuming $E_t$ to fall in the range of values previously established via DLTS. This assumption made a priori is thus fundamental to their analysis. On the contrary, the DPCM method is capable of providing the same results by analyzing the $\tau_{Al\text{-}O}$ data alone with no assumptions needed. Figure 6.7 shows the DPCM graph obtained from the modeling of $\tau_{Al\text{-}O}$ data along with the metal defects' parameters taken from Ref. [15], [56], [57], [123], [125], [127]–[129].

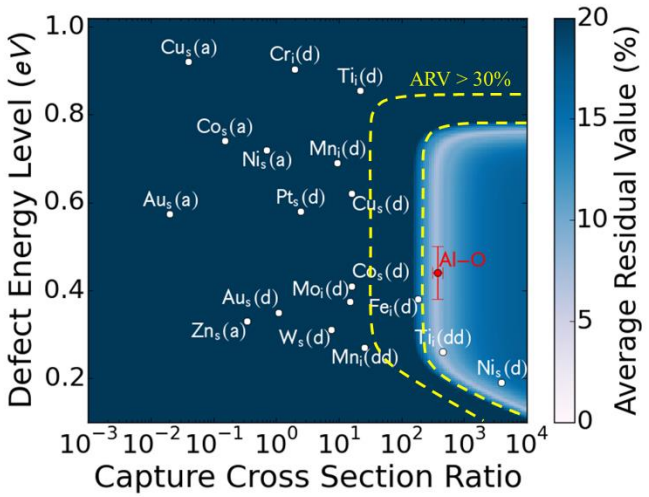


Fig. 6.7 IDLS-DPCM analysis of $\tau_{SRH}$ data reported by Sun *et al*. [15] Al-O defect is placed at $E_t = E_v + 0.44$ eV and $k = 380$. The error bars associated to $E_t$ and $k$ represent the range of values reported in literature and the uncertainty evaluated by Sun *et al*., respectively. The area contained in between the yellow dashed lines represent the portion of the parameter space where a best fit for $\tau_{eff}$ data is found.

The resulting IDLS-DPCM plot is characterized by a single bright band with ARV < 5% in the high $k$-region of the parameters space. The plot shows the Al-O defect placed at $E_t = E_v + 0.44$ eV and $k = 380$ with error bars representing the range of values assessed from DLTS analysis for the former, and the uncertainty reported in Ref. [15] for the latter. Remarkably, despite no assumptions were made on $E_t$, the DPCM method results match with those presented by Sun *et al.* with an optimal $k$ value of 380 and an equal level of accuracy associated with it, as demonstrated by the width of the best fit region (brightest area) overlapping to their estimated range of uncertainty. Additionally, the DPCM method allows to visualize the lack of unicity associated with the analysis of IDLS data as, for an optimal $k$ value of 380, the same fit quality is obtained in the entire energy level range of $E_t = E_v +$ (0.26 – 0.76) eV.

Another aspect in which the DPCM analysis proves extremely valuable is the understanding of the widely scattered $k$ values reported in literature: Previous reports had, in fact, attempted to model $\tau_{eff}$ rather than $\tau_{Al\text{-}O}$ by mean of a single defect which resulted in a general poor fit [131], [132]. These authors were then inclined to assume the presence of a second shallow defect level, which obviously led to the wrong assessment of the Al-O defect level parameters. Similarly, when $\tau_{eff}$ rather than $\tau_{Al\text{-}O}$ is used in the DPCM method, the region of best fit results shifted towards much smaller $k$ values. However, a very poor fit is obtained as indicated by the ARV being above 30%. This finding is depicted in Fig. 6.7 by the area contained in between the yellow dashed lines. Thus, the DPCM analysis effectively demonstrates in a unique plot that $\tau_{Al\text{-}O}$ is to be preferred over $\tau_{eff}$ when assessing the Al-O complex recombination parameters, and that the assumption about the presence of a second defect is incorrect.

### 6.2.3 DPCM Applied to TIDLS Data

As the presence of a control sample may not always be feasible in most industrially relevant scenarios, we can expect the analysis of IDLS data to be generally insufficient for a correct defect level assessment. Moreover, even when a control sample is available, the lack of definitive information regarding $E_t$ obtained from the IDLS-DPCM plot seen in Fig. 6.7 further demonstrates that the analysis of a second physical variable is usually necessary in order to obtain the most accurate results out of the DPCM method. As previously stated, the most effective way is to expand the IDLS technique into TIDLS by introducing the analysis of the samples' lifetime temperature-dependence. To exemplify this, we refer to the TIDLS

analysis of c-Si intentionally contaminated with Mo performed by B. B. Paudyal et al. [16] via TIDLS in a range of temperatures of -110 °C – 150 °C. In this work, the authors focus on the analysis of the *T*-dependence of capture cross section of both holes $\sigma_p(T)$ and electrons $\sigma_n(T)$, and evaluate the Mo defect energy level $E_t$ based on considerations related to the trend of these two physical quantities with temperature. In fact, if $E_t$ is assumed lower than $E_v$ + 0.375 eV, $\sigma_n(T)$ negative slope is found to vary as the temperature increases above 0 °C. However, this variation would implicate a change of the physical mechanism for the capture of electrons - an event considered unlikely by the authors - and thus Paudyal et al. assumed $E_t$ to be higher than $E_v$ + 0.375 eV. However, it must be noted that a change in the electrons capture mechanism with temperature could not be theoretically ruled out, and thus $E_t$ was not undoubtedly assessed. Furthermore, the value of $E_t = E_v + 0.375$ eV is significantly higher than any other value previously reported in literature such as the one proposed by Rein of $E_t - E_v = 0.317 \pm 0.005$ eV [17] based on a TIDLS analysis across the temperature range of 0 °C – 300 °C.

In order to determine which of the previously reported $E_t$ values is to be considered the closest to the real Mo energy level, we perform DPCM analysis using the experimental TIDLS data reported in Fig. 2 b) on Ref. [16]. However, since the Auger recombination mechanisms *T*-dependence has not been evaluated at temperatures below 0 °C, we make use of the data obtained at $T > 0$ °C only. Figure 6.8 shows the resulting map following DPCM analysis, where the defect levels suggested by Paudyal *et al*. and Rein are shown in orange and labeled with the superscript “1” and “2”, respectively.

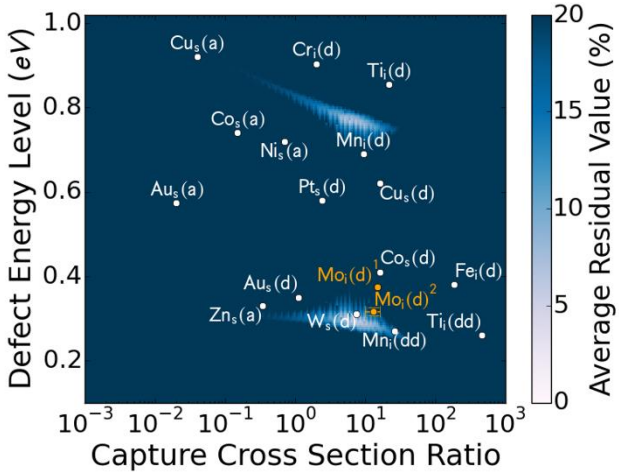


Fig. 6.8 TIDLS-DPCM image obtained from the analysis of data from Ref. [16]. Mo defect levels proposed by Paudyal et al., [16] indicated by the superscript "1", and Rein, [17] indicated by the superscript "2", are shown in orange. The errors associated with the Rein's $E_t$ and $k$ values are included in $Mo_i(d)^2$.

Compared to the results obtained from the analysis of IDLS data, the TIDLS-DPCM plot shows an extremely high capability of discriminating among different defects since only two small regions of the parameters space have an ARV below 5%, one in the upper half of the band gap and one in the lower half. More importantly, the method clearly shows that the defect parameters proposed by Rein [17], and in particular the energy defect level of $E_t$ - $E_v$ = 0.317 ± 0.005 eV, are the closest to the best combination of $E_t$ and $k$ represented in the DPCM graph by the ARV scale. The small distance among this defect level and this region of the parameters space is probably due to the method not taking into account the $T$-dependence of physical quantities like $k$ or the Auger lifetime which we will demonstrate in the next chapter to be strongly temperature dependent. Following the reasoning above, this result suggests that $\sigma_n$ $T$-dependence is changing at high temperatures as $E_t$ is lower than $E_v$ + 0.375 eV, and thus that different capture mechanisms of electrons are expected to dominate in the temperature ranges below and above 0 °C.

One aspect to take into account in the analysis of the DPCM method is the possibility of having multiple recombination-active defects at the same time which would obviously further complicates the modeling of IDLS and TIDLS data. Since different defect levels most often will dominate different portions of the lifetime vs. injection level curve depending on their $E_t$ and $k$ values [17], [57], a possible strategy for assessing the presence of multiple defects would be to accurately restrain the data to be processed through DPCM to a limited range of injection levels. An evaluation of this concept is presented in a separate study [133].

### 6.2.4 DPCM Applied to Simulated Data

As previously noticed by comparing Fig. 6.7 and 6.8, the DPCM capability of identifying univocal solutions for the parameters of a defect is very much dependent upon the amount of experimental data available for analysis. In particular we can expect variations depending on the data range of injection level and temperature. To evaluate this aspect of the DPCM method in detail we simulated a set of TIDLS data based on the SRH recombination model for a hypothetical *p*-type Si sample with $N_A = 10^{15}$ cm$^{-3}$, and a defect level with $E_t - E_v = 0.24$ eV, $k = 100$, and $\tau_{p0} = 50$ μs.

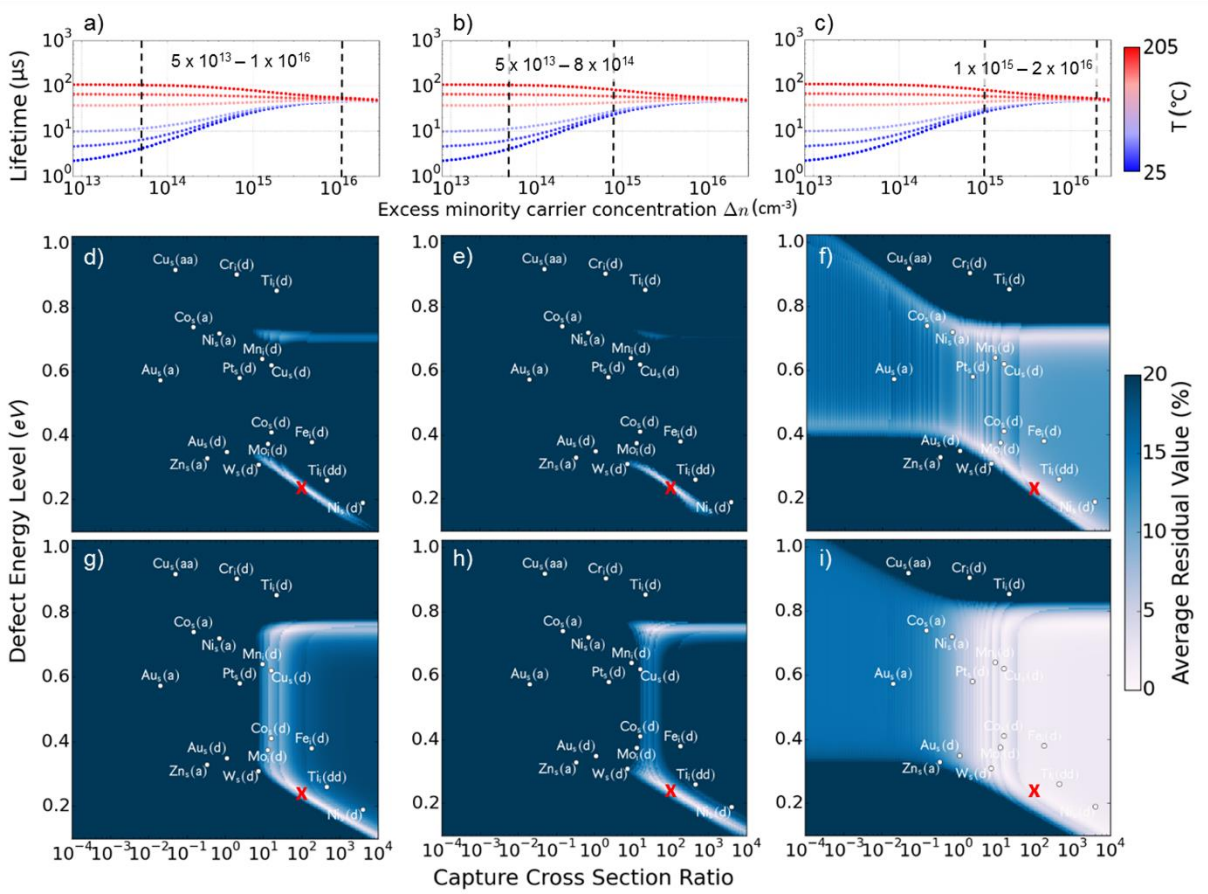


Fig. 6.9 Top row: Simulated TIDLS data obtained for a hypothetical *p*-type Si sample with $N_A = 10^{15}$ cm$^{-3}$, and a defect level with $E_t - E_v = 0.24$ eV, $k = 100$, and $\tau_{p0} = 50$ µs; lifetime data are shown in an injection level range of 5 x $10^{12}$ cm$^{-3}$ – 2 x $10^{16}$ cm$^{-3}$, and a temperature range of 25 °C – 205 °C with a 30 °C step. The injection ranges reported in between dashed lines in a), b), and c) represent the ranges of data used for the DPCM analysis underneath. Middle row: d), e), and f) show the DPCM graphs resulting from using the TIDLS data across the different injection level ranges indicated in a), b) and c), respectively, and the full range of temperatures. Bottom row: g), h), and i) show the DPCM graphs resulting from using TIDLS data across the different injection level ranges indicated in a), b), and c), respectively, and a limited range of temperatures, i.e., 25 °C – 85 °C. The red crosses represent the position of the defect level used to generate the simulated data.

The top row of Fig. 6.9 shows the simulated TIDLS curves obtained for the chosen scenario; the graphs show the data in an injection level range of 5 x $10^{12}$ cm$^{-3}$– 2 x $10^{16}$ cm$^{-3}$, and a temperature range of 25 °C – 205 °C with a 30 °C step. The dashed lines indicate the data ranges of injection levels used to generate the DPCM graphs which are shown in the middle and bottom rows. In particular, from left to right, the injection level ranges considered

are: a) 5 x $10^{13}$ $cm^{-3}$ – 1 x $10^{16}$ $cm^{-3}$, b) 5 x $10^{13}$ $cm^{-3}$ – 8 x $10^{14}$ $cm^{-3}$, i.e., low injection, and c) 1 x $10^{15}$ $cm^{-3}$ – 2 x $10^{16}$ $cm^{-3}$, i.e., high injection. In the middle row of Fig. 6.9 we show the DPCM graphs obtained when using data from the different injection level portions of the TIDLS curves indicated in a), b), and c), respectively, and the full range of temperatures. It appears immediately that the DPCM graphs d) and e) in Figure 3 provide the most unambiguous results with very small bright regions extending from the originally defined position of the defect level (represented with a red cross). Noticeably, the best outcome is obtained in the DPCM graph of Fig. 6.9 e) in which the analysis is based on the low injection portion of the lifetime curves only. In the DPCM graph of Fig. 6.9 f), only data from the high injection portion of the curves are considered and a vast area of good fit is obtained which encloses more than half the parameters space, thus making the identification of the defect level less straightforward. These findings indicate that it is not simply the extension of the range of data which determines the quality of the DPCM response, but rather the presence of characteristic features revealing the peculiar interplay among lifetime injection- and temperature-dependence, which is the true signature of any defect level. For the simulated scenario chosen here, the strongest features appear at an injection level < $10^{15}$ $cm^{-3}$ – as opposed to the rather flat and temperature-independent high injection portion of the curves – and so the analysis accounting for the data in the low injection regime provide the best outcomes. However, it must be noted that the presence of such characteristic features is strongly dependent on the energy of the defect level. This aspect is well exemplified in Fig. 1 of Ref. [133] which shows that for deep defect levels a very small TIDLS data temperature-dependence is observed in the whole injection level range, and thus we can expect the DPCM

method to be largely unaffected by the particular choice of injection levels included in their analysis. The bottom row of Fig. 6.9 shows the DPCM graphs obtained when, besides from varying the range of injection level as for graphs d), e), and f), only three temperatures are taken into account in the limited range across 25 °C – 85 °C. As now less data are provided to the DPCM analysis, all the graphs show slightly broader regions of good fit. Nonetheless, the results for graphs g) and h), i.e., those containing the low injection region, still show a good level of discrimination making the identification of the lifetime-limiting defect level still possible despite the narrow ranges of data available.

# 7 AUGER LIFETIME *T*-DEPENDENCE

In Chapter 6 we have seen how the extrapolation of $\tau_{bulk}$ from the measured effective lifetime revealed that the advanced parameterization proposed by Richter *et al*. [19] for $\tau_{int}$ does not hold for measurements at high temperatures, with experimental values exceeding the proposed intrinsic limit lifetime already at 150 °C (see Figs. 6.2 and 6.3). As crystalline silicon (c-Si) solar cells inches closer and closer to their thermodynamic and practical limit [28], [134], [135], these results prove that an accurate evaluation of the effect of temperature on a high-efficiency device is critical to fully understand the benefits of a more advanced architecture. Heterojunction (HJ) interdigitated back contact (IBC) solar cells with thin film Si technology, for example, have recently achieved an outstanding photoconversion efficiency of 26.6% [27]. These technologies are characterized by extremely high values of open-circuit voltage ($V_{OC}$) as a result of the increasing quality of the bulk material and the excellent level of surface passivation provided by the hydrogenated amorphous silicon (a-Si:H) at the interface with c-Si [18], [136], [137]. For these devices, $V_{OC}$ values above 750 mV have been recently reported [28], [32], [138] showing that high-efficiency solar cells ultimately limited by the intrinsic recombination mechanisms in the base material, i.e. radiative, and Auger recombination, are within reach. Green [139] and Tiedje *et al*. [140] independently showed that among these two recombination processes, Auger recombination places the most severe intrinsic limit on the one- sun solar cell operation since the excess energy associated with its process is entirely loss as phonons, whereas in the radiative recombination process most of the photons emitted are reabsorbed elsewhere in the silicon base. More recently, Augusto *et al*. [141] showed that Auger recombination accounts for up

to 82% of the recombination in a solar cell at open-circuit conditions at room temperature whereas the radiative recombination accounts only for 9% of the recombination. As operating conditions met by modules deployed in the field are known to differ significantly from the standard testing conditions (STC, 1000 $W \cdot m^{-2}$, 298 K, AM1.5g spectrum), an accurate modeling of the Auger injection- and temperature-dependent recombination rate is crucial not only for the correct interpretation of effective carrier lifetime data of Si material, but also for the simulation of device performance required to predict and optimize the annual yield of a solar cell in the field.

Auger recombination mechanisms have been extensively studied in the past by assuming the charge carriers involved in the processes to be non-interacting quasi-free particles [142]–[145]. Results have been reported for a broad variety of materials under different experimental conditions including lowly doped Si under high-injection conditions [146], [147], and highly doped Si under both low- and high-injection conditions [148], [149]. Furthermore, numerous studies have focused on the temperature dependence of the Auger recombination rate [122], [146], [149], [150]. Based on these studies, some very successful parameterizations have been proposed in the past [19], [122], [149], [151]. However, they all present the disadvantage of being restricted to either a limited injection level range [122], [149] or to room temperature conditions [19], [151].

In this Chapter, we experimentally evaluate the Auger lifetime ($\tau_{Auger}$) in silicon material across a range of temperatures from 30 ºC to 230 ºC and a range of injection density from 2 x $10^{15}$ $cm^{-3}$ to 1 x $10^{16}$ $cm^{-3}$. This injection density range is fundamental for the understanding of the performance of high-efficiency solar cells under different operating conditions such as

at maximum power point conditions (MPP) and open circuit conditions. The strong $\tau_{Auger}$ temperature-dependence experimentally observed in the whole injection density range is explained following the quantum mechanical approach proposed by Hangleiter and Häcker [152], [153] in which the Auger recombination rate is increased by the Coulombic interaction among charge carriers. Finally, we evaluate the impact of the experimental $\tau_{Auger}$ temperature-dependence on the limit imposed by the intrinsic lifetime on the implied voltage (*iV*) within the analyzed range of injection levels and temperatures, and compare it to the results obtained by applying the widely adopted Richter parameterization [19].

## 7.1 Experimental Results vs. Parameterization

The analysis performed in this section is based on the experimental data of the samples passivated with a stack of a-Si:H(i)/a-Si($n^+$) presented in section 6.1. Figure 7.1 shows the $\tau_{bulk}$ data as shown in Fig. 6.3 for temperatures up to 150 ºC along with the additional experimental results for temperatures up to 230 ºC. In Fig. 7.1 we also report the Auger lifetime calculated according to Richter's parameterization, $\tau_{Aug,Richter}$, at 30 ºC, 130 ºC, and 230 ºC, which effectively demonstrates that its temperature-dependence is negligible in the whole temperature range evaluated as the three curves fall on top of each other in the injection level range considered.

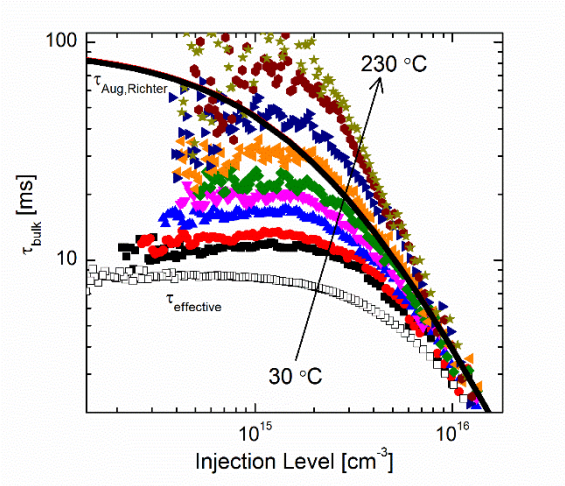


Fig. 7.1 Data from Bernardini *et al*. [18]. Bulk lifetime as function of injection level at temperatures from 30 ºC to 230 ºC with a step size of 20 ºC for samples passivated with an a-Si:H(i)/a-Si:H(n) stack. The solid lines represent the Auger lifetime calculated according to the Richter parameterization at 30 ºC, 130 ºC, and 230 ºC: As the model does not account for temperature variation, all lines fall on top of each other. Effective lifetime at room temperature (open squares) is also reproduced for comparison.

Very similar bulk lifetime results were also obtained for the samples when passivated with intrinsic a-Si:H alone, which demonstrates the consistency of the method (see Figs. 6.2 and 6.3). However, given that for the a-Si:H(i)/a-Si:H(n) stack SRV is always below 1 cm/s, and thus the error associated with it is lower than for samples passivated with a-Si:H(i), we consider these results as the most trustworthy for the data analysis presented herein.

As the temperature increases the bulk lifetime is found to rapidly approach the limit represented by the calculated $\tau_{Aug,Richter}$ and an overlap is eventually reached at 150 ºC. For temperatures above 150 ºC, the bulk lifetime is found to exceed this limit which effectively points at the inadequacy of Richter's parameterization to properly describe the Auger lifetime temperature dependence. Additionally, bulk lifetime results in Fig. 7.1 also show a decreasing trend for an injection level below 2 x $10^{15}$ cm$^{-3}$, which increases at higher temperatures. Note the slight increment in the scattering of the data observed at this low level

of injection, which origin could be related to edge recombination effects [111], [154], [155] (samples are only 5 cm x 5 cm in size), and additional recombination at the surface due to the band bending at the a-Si:H/c-Si interface [14], [156]. For this reason, the following analysis is restricted to the injection level range across 2 x $10^{15}$ $cm^{-3}$ - 1 x $10^{16}$ $cm^{-3}$ where the bulk lifetime decrement is not observed. It must be stressed that this range still includes the fundamental injection levels corresponding to both $V_{OC}$ conditions and MPP conditions of a high-performance solar cell, 1-2 x $10^{16}$ $cm^{-3}$ and 2-3 x $10^{15}$ $cm^{-3}$, respectively.

By re-ordering Eq. 9, the experimental Auger lifetime ($\tau_{Aug,exp}$) can be extrapolated at any injection level and temperature by removing the inverse of SRH and radiative lifetime terms from $1/\tau_{bulk}$. In the analysis of these samples, the identification of the lifetime-limiting defect center required for the modeling of $\tau_{SRH}$ is achieved by applying the defect parameter contour mapping (DPCM) described in the paragraph 6.2. Following the results obtained by applying this method, we decided to model $\tau_{SRH}$ using the parameters for the substitutional zinc ($Zn_s$) defect level which is the one that showed the highest fit quality to the experimental data (see Fig. 6.6). However, very similar results for $\tau_{Aug,exp}$ were obtained when using parameters from other impurities such as $Cu_s$ and $Au_s$ which also showed a good degree of fit of the experimental data. As previously mentioned, the radiative lifetime is modeled by applying the Coulomb-enhanced radiative recombination model proposed by Altermatt *et al*. [157] to the recombination coefficient measured by Nguyen *et al*. [120] according to the parameterization given in Altermatt *et al*. [158]. The uncertainty associated to $\tau_{Aug,exp}$ was estimated to be ±25% throughout the entire range of temperatures and injection levels analyzed. This value was obtained starting from the ±7.5% uncertainty reported by Blum *et*

*al*. [130] for transient lifetime measurements. As exemplified in Eq. 20, this value has to be accounted for twice in the error propagation as it affects directly the $1/\tau_{eff}$ term, and it also impacts the uncertainty associated with the SRV values along with the samples' thickness. However, as for the samples coated with the a-Si:H(i)/a-Si:H(n) stack SRV is always below 1 cm/s, the error associated with this term is very small and does not affect significantly the overall $\tau_{Aug,exp}$ extrapolation procedure. An additional source of uncertainty comes from the metal impurity chosen to model $\tau_{SRH}$ but, as previously stated, this factor does not have a significant impact on the extrapolation of $\tau_{Aug,exp}$ provided that one of the impurities resulting in the highest degree of fit of the experimental data is taken into account.

Figure 7.2 shows experimental Auger lifetime (dots) evaluated from Eq. 9 for temperatures in the range of 30 ºC - 230 ºC and injection levels across the range of 2 x $10^{15}$ $cm^{-3}$ - 1 x $10^{16}$ $cm^{-3}$. The experimental data are plotted in Arrhenius form for each injection level, which are also shown in the graph (dashed lines).

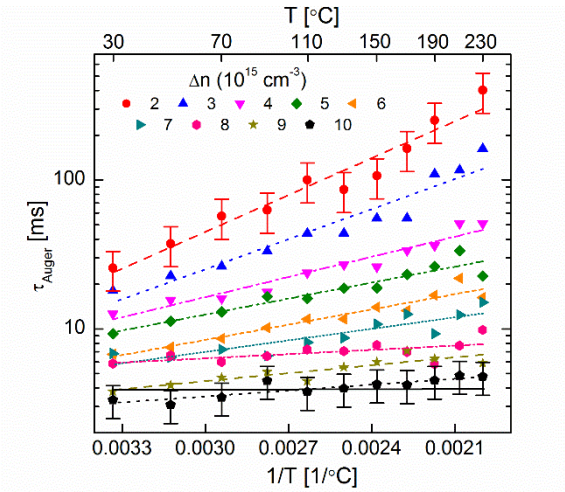


Fig. 7.2 Experimental Auger lifetime (dots) as a function of the inverse of temperature for different injection levels across the range of 2 x $10^{15}$ $cm^{-3}$ - 1 x $10^{16}$ $cm^{-3}$ along with the fits obtained from exponential curves by applying an Arrhenius equation (dashed lines). The Auger lifetime calculated according to Richter parameterization (**$\tau_{Aug,Richter}$**) at an injection level of 1 x $10^{16}$ $cm^{-3}$ **is** shown for comparison (solid black line). The experimental error for $\tau_{Aug,exp}$ shown for the curves at 2 x $10^{15}$ $cm^{-3}$ and 1 x $10^{16}$ $cm^{-3}$ was estimated as ±25%.

Figure 7.2 shows that the experimental Auger lifetime is strongly temperature dependent and increases at higher temperatures across all injection levels. The dependence is more pronounced in the lower part of the injection level range and yields $\tau_{Aug,exp}$ values above 400 ms at 230 ºC for $\Delta n$ = 2 x $10^{15}$ $cm^{-3}$, more than one order of magnitude higher than the Auger lifetime calculated according to Richter parameterization. On the contrary, for an injection level of 1 x $10^{16}$ $cm^{-3}$ the experimental *T*-dependence is significantly reduced and $\tau_{Aug,Richter}$ (solid black line in Fig. 7.2) is contained within the estimated uncertainty associated to $\tau_{Aug,exp}$ for the whole temperature range.

## 7.2 Fitting of Experimental Results

Interestingly, all the $\tau_{Aug,exp}$ vs. *T* curves can be successfully fitted using a temperature dependent Arrhenius equation of the form

$$\tau_{Aug,exp}(T;\ \Delta n) = \tau_{Auger}^{\infty}(\Delta n)e^{\frac{-E_a(\Delta n)}{kT/q}} \tag{32}$$

where the prefactor $\tau_{Auger}^{\infty}(\Delta n)$ can be interpreted as the Auger lifetime for $T \rightarrow \infty$, *k* is the Boltzmann constant, *q* is the elementary electric charge, and $E_a$ is the activation energy.

The strong Auger lifetime temperature dependence shown in Fig. 7.2 can be explained following the theory proposed by Hangleiter and Häcker [152], [153] in the late 80's. Their quantum mechanical approach described the Auger recombination in silicon as enhanced by the presence of "scattering" and "bound" states, i.e. excitons, due to the Coulombic interaction among charge carriers. This interaction is accounted for in the calculations by multiplying the traditional Auger recombination rate ($R^0$), which is obtained by assuming

charge carriers as non-interacting free particles [148], to the so-called enhancement factors, either $g_{eeh}$ or $g_{ehh}$, depending on whether the energy and momentum of the recombining electron-hole pair are transferred to another electron (*eeh*) or to another hole (*ehh*). The corresponding recombination rates, *R*, are then given by the equations

$$R_{eeh} = g_{eeh}R^0_{eeh} \text{ and } R_{ehh} = g_{ehh}R^0_{ehh} \quad (33)$$

The enhancement factors have been experimentally observed to decrease exponentially towards higher temperature due to the increasing disturbance to the *e-h* bound states introduced by the thermal energy [153]. Thus, from Eq. 33, the Auger recombination rate is also expected to decrease exponentially with increasing temperature corroborating the strong Auger lifetime increment seen in Fig. 7.2. The fact that the $\tau_{Aug,exp}$ *T*-dependent curves follow an Arrhenius behavior characterized by the activation energy, $E_a$, indicates that the dominant Auger recombination mechanism at these temperatures involves a transition of energy and momentum among charge carriers without the contribution of a phonon, i.e., phononless mechanism. These results corroborate the analysis based on extensive quantum mechanical calculations of *eeh* Auger recombination process, which is expected to dominate in *n*-type silicon, previously suggested for both undoped [150] and highly doped [159] material. The intensity variation of the experimental Auger lifetime *T*-dependence at different injection levels shown in Fig. 7.2 results into a strong $E_a$ injection-dependence which, to my best knowledge, has never been reported before. Figure 7.3 shows the activation energy $E_a$ in the range of 2 x $10^{15}$ $cm^{-3}$ - 1 x $10^{16}$ $cm^{-3}$ obtained from the fits of the experimental data shown in Fig. 7.2 with an $R^2$ value above 0.8.

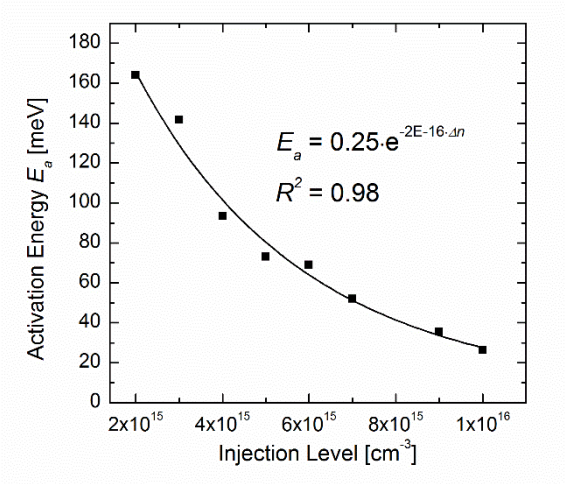


Fig. 7.3 Activation energy as function of the injection level as obtained from the fitting of the experimental data in Fig. 7.2. The activation energy $E_a$ shows an exponential trend with a strong increment towards low injection levels.

The only other activation energy previously suggested in literature for the phononless Auger recombination mechanism was calculated by Huldt *et al*. [150] for undoped/highly-injected Si - $E_a$ = 2.6 meV. Using the dependency reported in Fig. 7.3, an activation energy of 2.6 meV is found to correspond to an injection level of 2.3 x $10^{16}$ $cm^{-3}$ showing that our results are in good agreement with those reported by Huldt *et al*. [150]. Based on these observations, we suggest that for lower injection levels the impact of thermal agitation on the amount of disrupted excitons is enhanced since any single *e-h* pair represent a more significant fraction of the total amount of excitons in the material. This could in turn explain the stronger $\tau_{Aug,exp}$ increment towards high temperatures for the curves in the lower injection regime shown in Fig. 7.2 and the corresponding increment of activation energy shown in Fig. 7.3.

As previously stated, the prefactor $\tau_{Auger}^{\infty}$ in Eq. 32 can be interpreted as the Auger lifetime at infinite temperature. Figure 7.4 shows the parameter calculated from the fitting of

the experimental data in Fig. 7.2 across the range of injection level of 2 x $10^{15}$ $cm^{-3}$ - 1 x $10^{16}$ $cm^{-3}$.

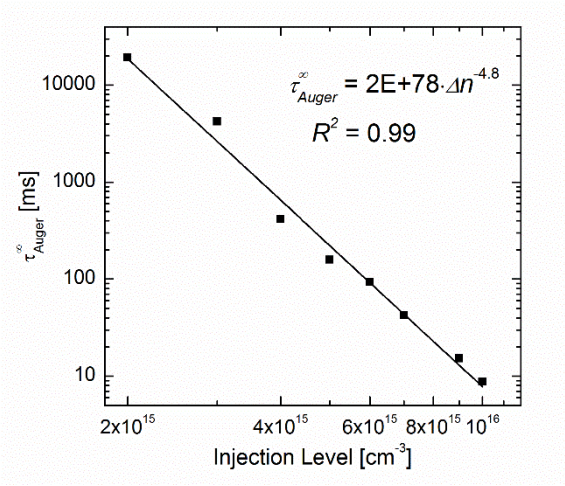


Fig. 7.4 Auger lifetime for infinite temperature as a function of the injection level. The parameter is obtained at each injection level from the fitting of the experimental data shown in Fig. 7.2.

Under these conditions, no contributions from the bound states to the Auger recombination rate are expected to occur. As a consequence, the intrinsic upper limit is greatly lifted especially in the lower range of injection levels where the low concentration of minority carriers results in a small recombination rate. Remarkably, a very good fit is obtained by using a power equation with $\Delta n^{-4.8}$ as shown in Fig. 7.4 with a strong decrement of $\tau^{\infty}_{Auger}$ for increasing injection level. However, we restrain from assigning a physical meaning to these findings as a full parameterization of the factors included in $\tau^{\infty}_{Auger}$ is necessary and requires further investigation.

## 7.3 Re-evaluation of $V_{OC}$

The experimentally determined Auger lifetime and its temperature-dependence allow the re-evaluation of the $V_{OC}$ and $V_{mpp}$ limit at different temperatures imposed by the intrinsic lifetime. For a 50 $\mu$m-thick solar cell, and assuming a maximum photogeneration current density $J_{ph}$ given by the Lambertian light trapping limit of 43 mA/cm$^2$ [89], we calculate $V_{OC}$ thanks to the equation valid for high-injection conditions [141]

$$V_{OC} = \frac{kT}{q} ln\left(\frac{J_{ph} \cdot \tau_{int} \cdot \Delta p}{q \cdot w \cdot n_{i,eff}^2}\right) \tag{34}$$

where $k$ is the Boltzmann constant, $q$ is the elementary charge, $w$ is the cell thickness, and $n_{i,eff}$ is the effective intrinsic carrier concentration. The ideality factor $n$ is assumed to be equal to 1 even though, when Auger recombination is dominating as it is for high-injection conditions, the local ideality factor is known to decrease below unity [160]. This assumption was made for the sake of simplicity since any variation of the ideality factor would equally affect all the calculated implied-voltage curves shown in Fig. 7.5 and thus would not add any information to the following discussion.

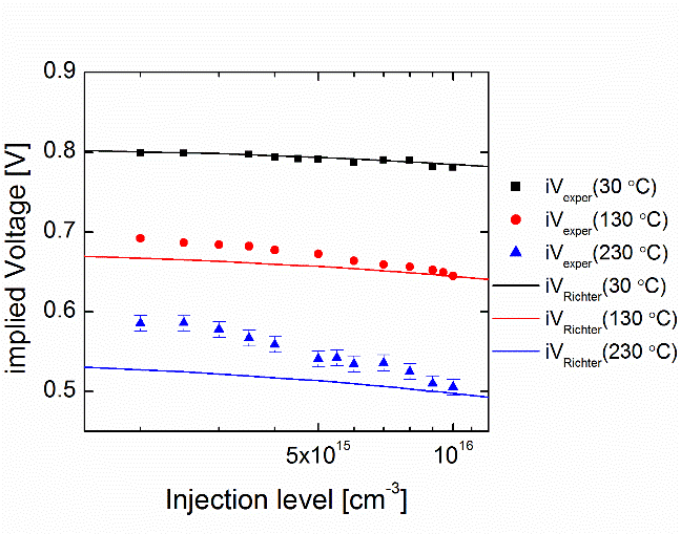


Fig. 7.5 Temperature-dependence of implied voltage (*iV*) limited by intrinsic recombination. The *iV* curves are obtained from Eq. 34 by either using the parameterization for intrinsic lifetime proposed by Richter [19] (solid lines) or the experimentally determined Auger lifetime (symbols). As the temperature increases, the discrepancy in the mid-injection range increases due to the strong increment of Auger lifetime shown in Fig. 7.2. The error shown for $iV_{exper}(T = 230\ ^{o}C)$ was calculated by accounting for the ±20% uncertainty on $\tau_{Aug,exp}$.

As expected from the very good agreement among $\tau_{Aug,exp}$ and $\tau_{Aug,Richter}$ at high injection level seen in Fig. 7.2, the implied-voltage as calculated using the former (dots) or the latter (lines) at 1 x $10^{16}$ $cm^{-3}$ have very similar values at all temperatures. However, at an injection level of 2 x $10^{15}$ $cm^{-3}$ the discrepancy among $iV_{exper}$ and $iV_{Richter}$ increases substantially at high temperatures due to the strong increment of the experimental Auger lifetime. Figure 7.6 shows the implied-voltage as calculated using $\tau_{Aug,exp}$ (dots) or $\tau_{Aug,Richter}$ (lines) at different temperatures for these two specific injection levels.

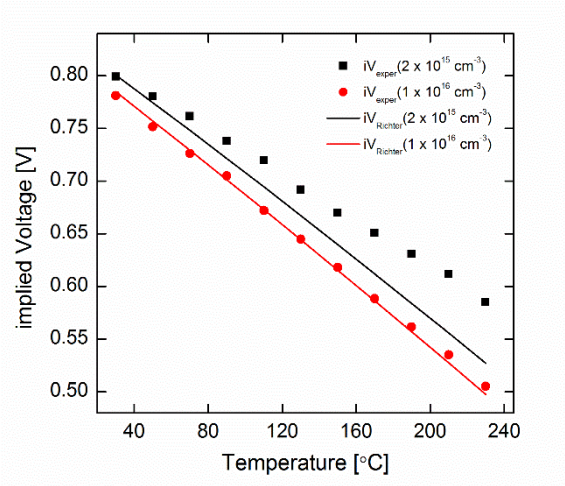


Fig. 7.6 Implied voltage (*iV*) temperature-dependence for two injection levels as calculated according to Eq. 34 using either the experimental Auger lifetime ($iV_{exper}$) or the Richter parameterization ($iV_{Richter}$). At an injection level of 1 x $10^{16}$ $cm^{-3}$ $iV_{exper}$ and $iV_{Richter}$ match very well whereas for an injection level of 2 x $10^{15}$ $cm^{-3}$ the strong increment of Auger lifetime with temperature partially counteracts the decrease of $iV_{exper}$.

As previously stated, $iV_{exper}$ and $iV_{Richter}$ show little discrepancy for an injection level of 1 x $10^{16}$ $cm^{-3}$ in the whole temperature range. On the contrary, for an injection level of 2 x $10^{15}$ $cm^{-3}$, the decrement rate for $iV_{exper}$ is found to be significantly lower than for $iV_{Richter}$ as the strong temperature-dependence of Auger lifetime mitigates its decrease. This discrepancy leads to an $iV_{exper}$ absolute value ~ 1% higher than the expected $iV_{Richter}$ at a standard module operating condition of 55 ºC, ~ 3% higher at the temperature often encountered by modules on the field of 90 ºC [30], and ~ 11% higher at 230 ºC. This finding is particularly important as it has been observed that for high-efficiency architectures, lifetime in this injection level range is critical for the cell performance at maximum power point [161], [162]. A high lifetime is, in fact, fundamental to obtain a high value of the voltage at the MPP and thus a high fill factor (FF). These results thus indicate that for intrinsically limited advanced solar cells, the loss of performance at high temperatures is significantly lower than what previous

reports suggested, as the limits imposed by Auger recombination becomes less severe under real operating conditions, especially in the fundamental range of MPP operation conditions.

It must be noted that a lifetime exceeding the intrinsic limit by Richter *et al* [19] has previously been reported already at room temperature [163]–[166] for *n*-type silicon material which points to the need of an overall re-evaluation of the accepted empirical parameterization similarly to what recently proposed by Veith-Wolf *et al*. [167]. However, these findings do not contradict the temperature-dependent results presented herein since a higher $\tau_{Auger}$ limit would simply indicate that a partial reallocation of the recombination mechanisms strength is required to model the experimental data with a heavier contribution assigned to the SRH recombination, i.e., a higher metal impurities density, and a lower contribution assigned to the Auger recombination rate. Finally, this newly reported Auger lifetime *T*-dependence will allow a more accurate modeling of high efficiency solar cells required to predict and optimize the annual yield of a module when deployed in the field and may significantly contribute to the bankability and market share increase of high efficiency architectures.

# 8 CONCLUSIONS

The main goal of this work was to provide a thorough understanding of the recombination mechanisms affecting photovoltaic devices in order to help achieving the highest possible photoconversion efficiency. By accurately applying the thickness variation method, we have shown the potential of temperature- and injection-dependence lifetime spectroscopy (TIDLS) technique for characterization of both high-quality c-Si material and surface passivation layers under different experimental conditions. We demonstrated that a thorough analysis of the surface recombination velocity temperature- and injection-dependence not only allows to gain insights on the dielectric layer material and the recombination mechanisms happening at the interface, but it is also strictly required for the proper modeling of TIDLS data, and thus the correct identification of the lifetime-limiting defect in the bulk of the material. With this regard, we developed a tool denominated defect parameter contour mapping (DPCM) to help visualize and identify lifetime limiting impurities in an immediate and less convoluted way.

Experimental SRV data were obtained for samples passivated with several passivation materials and various modeling frameworks were applied to extrapolate invaluable information. In particular, a-Si:H(i) and a-Si:H(i)/a-Si($n^+$) passivation layers were investigated by adopting the model proposed by Olibet *et al*. [14]. The most important interface parameters were evaluated with the results indicating the density of charges at the interface $Q_S$ as the responsible for the two passivation schemes different temperature response shown herein. The degradation of this passivation layers over time is also evaluated and possible strategies to overcome this issue are discussed. For $SiN_x$-coated samples, the

SRV analysis revealed the presence of a surface damage region between the substrate and the passivation layer likely caused by the excessive amount of hydrogen.

The correct extrapolation of the bulk lifetime temperature-dependence further allowed the re-evaluation of the Auger lifetime *T*-dependence. The results were compared to the widely accepted advanced parameterization proposed by Richter *et al*. [19]. At room temperature a very good correlation among experimental data and parameterization was found which corroborates the experimental method consistency, whereas a strong discrepancy was obtained at higher temperatures. The strong $\tau_{Auger}$ temperature-dependence experimentally observed in the whole injection density range was explained following a quantum mechanical approach accounting for the increased Auger recombination rate due the Coulombic interaction among charge carriers. Finally, we evaluated the impact of the experimental $\tau_{Auger}$ temperature-dependence on the limit of the implied voltage (*iV*) for a theoretical intrinsic-limited solar cell and showed that such a device would significantly benefit from the increased lifetime under real operation conditions compared to an extrinsic-limited one.

# 9 FUTURE WORK

The work presented in this dissertation aimed at providing a thorough understanding of the difference recombination mechanisms of charge carriers that affect a solar cell and limit its efficiency to a level well below the theoretical full potential under varying operation conditions.

Despite the many results obtained and the knowledge gained on a number of aspects related to the performance of materials used either as absorber layers or surface passivation layers, there are still many questions that need to be addressed and that, if answered, may further help the solar community achieving the highest efficiency possible. In particular, I identify the following questions as the most pressing for the continuation of the work presented herein:

1. Can we provide an improved parameterization of the Auger lifetime to account for its temperature-dependence?

2. What's the most promising surface passivation material when taking into account its SRV temperature-dependence?

3. Can we further improve the performance of the surface passivation materials analyzed by including additional processing steps such as hydrogenation or Corona charging?

As demonstrated in this dissertation, the recombination mechanisms temperature-dependence is generally an extremely important aspect for the correct evaluation of the final device performance as their relative weight can be completely overturned when moving from the lab to the field conditions. Given the current trend towards higher quality material and high-performance architectures, answering the first question is thus crucial to be able to

correctly predict the final solar cell efficiency at high temperatures. A comparison will be made among our experimental results and the parameterization proposed by Altermatt *et al*. [149] which, to the author's knowledge, is the only attempt reported in literature at providing a parameterization of the Auger lifetime that takes into account its temperature-dependence.

Addressing the question contained in item 2 is a very broad task given the multitude of proposed materials in literature for surface passivation purposes. However, given the consistency and reliability of the method established in this dissertation, we believe that many more materials could be characterized in the future without an excessive waste of resources. As an example, we recently established a collaboration with the Energy Research Center of The Netherlands (ECN) in order to evaluate the SRV temperature- and injection-dependence of poly-Si. The collaboration will make use of both *p*- and *n*-type high-quality material initially prepared at ASU according to the procedure described above and will be subsequently coated at ECN with two different poly-Si recipes before being sent back to ASU for testing in the DEfECT laboratory.

Finally, the question contained in item 3 points at the possibility to explore the impact of several processing steps on the surface recombination velocity of different materials. Some of these additional steps such as hydrogenation and Corona charging have already been proven to yield a positive impact on the passivation properties of some surface passivation materials but their contribution has not been thoroughly evaluated at different operation conditions. Furthermore, the effects of these treatments have not been proven to be permanent and may be lost due to varying operation conditions. Thus, a full SRV

temperature- and injection-dependence analysis would provide invaluable information on the passivation mechanisms and help achieving the materials full potential.

# 10 SUMMARY OF ACCOMPLISHMENTS

The following is a summary of the papers/proceedings and presentations that have resulted from the work described in this dissertation.

**Peer-Reviewed Publications**

1. **S. Bernardini**, S. Nie, Y. Zhu, Z. Hameiri, and M. I. Bertoni, "Analysis of $SiN_x$ SRV Injection- and Temperature-Dependence via TIDLS Measurements," *IEEE Journal of Photovoltaics*, submitted for publication (July, 2018).
2. **S. Bernardini**, A. Augusto, and M. I. Bertoni, "Revisiting the Auger Limit for High-Efficiency Solar Cells," *Progress in Photovoltaics: Research and Applications*, under review (April, 2018).
3. **S. Bernardini**, and M. I. Bertoni, "Insights into the Degradation of Amorphous Silicon Passivation Layer for Heterojunction Solar Cells," *Physica Status Solidi (a)*, accepted for publication (October, 2018).
4. **S. Bernardini** *et al.*, "Defect Parameter Contour Mapping: A Powerful Tool for Lifetime Spectroscopy Data Analysis," *Physica Status Solidi (b)*, 1800082 (2018), "Editor's choice".
5. **S. Bernardini** *et al.*, "Unraveling bulk defects in high-quality c-Si materials via TIDLS," *Progress in Photovoltaics: Research and Applications* **25**, pp. 209-217 (2017).
6. **S. Bernardini** *et al.*, "Nano-XRF Analysis of Metal Impurities Distribution at PL Active Grain Boundaries During mc-Silicon Solar Cell Processing," *IEEE Journal of Photovoltaics* **7**, pp. 244-249 (2017).
7. T. U. Naerland, **S. Bernardini**, M. S. Wiig, and M. I. Bertoni, "Is it possible to unambiguously assess the presence of two defect by temperature and injection dependent lifetime spectroscopy?," *Journal of Photovoltaics* **8**, pp. 465-472 (2018).
8. T. U. Naerland, **S. Bernardini**, N. Stoddard, E. Good, A. Augusto, M. I. Bertoni, "Comparison of iron-related recombination centers in boron, gallium, and indium doped silicon analyzed by defect parameter contour mapping," *Energy Procedia* **124**, pp. 138-145 (2017).
9. T. U. Naerland, **S. Bernardini**, H. Haug, S. Grini, L. Vines, N. Stoddard, and M. I. Bertoni, "On the Recombination Centers of Iron-Gallium pairs in Ga-doped Silicon," *Journal of Applied Physics* **122**, 085703 (2017).

## Conference Proceedings

1. **S. Bernardini** *et al.*, "Surface Photovoltage Spectroscopy as a Characterization Technique for Surface Passivation Quality Assessment," *WCPEC-7 Proceedings*, Waikoloa (2018).
2. **S. Bernardini** *et al.*, "Unraveling of Bulk and Surface Behavior in High-Quality c-Si Material via TIDLS," *IEEE PVSC Proceedings*, Portland (2016).
3. **S. Bernardini** *et al.*, "Nano-XRF Analysis of Metal Impurities Distribution at Grain Boundaries During mc-Silicon Solar Cell Processing," *IEEE PVSC Proceedings*, Portland (2016).
4. **S. Bernardini** *et al.*, "Defects Assessment and Modeling in High-Quality c-Si Material," *Workshop on Crystalline Silicon Solar Cells and Modules: Materials and Processes Proceedings*, Keystone (2015).
5. **S. Bernardini** *et al.*, "Evaluation of Passivation Layers via Temperature-Dependent Lifetime Measurements," *IEEE PVSC Proceedings*, Denver (2014).

## Conference Presentations

1. **S. Bernardini** *et al.*, "Analysis of $SiN_x$ SRV Temperature- and Injection-dependence via TIDLS Measurements," *WCPEC-7*, Waikoloa (2018).
2. **S. Bernardini** *et al*., "Surface Photovoltage Spectroscopy as a Characterization Technique for Surface Passivation Quality Assessment," *WCPEC-7*, Waikoloa (2018).
3. **S. Bernardini**, and M. I. Bertoni, "Degradation Analysis of Carrier Selective Contacts for SHJ Solar Cells", *MRS Fall Meeting & Exhibit*, Boston (2017).
4. **S. Bernardini** *et al*., "Nano-XRF Analysis of Metal Distribution at Grain Boundaries During mc-Silicon Solar Cell Processing," *IEEE PVSC*, Portland (2016).
5. **S. Bernardini** *et al*., "a-Si:H/c-Si Interface Passivation Characterization via TIDLS Analysis," *MRS Spring Meeting & Exhibit*, Phoenix (2016).

## Honors & Awards

1. **Best student paper award WCPEC-7 2018 Finalist**, Area 4, "Analysis of $SiN_x$ SRV Temperature- and Injection-dependence via TIDLS Measurements."
2. **Poster session co-chair at WCPEC-7 2018**, Area 4, Silicon Material: Feedstock, Wafers and Films.
3. **Best student paper award IEEE PVSC 2016**, Area 4, "Nano-XRF Analysis of Metal Impurities Distribution at Grain Boundaries During mc-Silicon Solar Cell Processing."
4. **Best poster award IEEE PVSC 2016**, Area 4, "Unraveling of Bulk and Surface Behavior in High-Quality c-Si Material via TIDLS."

# REFERENCES


[1] U.S. Global Change Research Program, “Climate Science Special Report,” 2017.

[2] “www.soulofamerica.com/blog/interstate-high-speed-rail-energy-sources/.” .

[3] Fraunhofer ISE, “Photovoltaics Report,” Freiburg, 2018.

[4] M. Shiao, “US Solar PV System Prices Continue to Decline in Q3 2015,” *GreenTech Media*, 2015.

[5] International Technology Roadmap for Photovoltaic (ITRPV) 9th ed., “International Technology Roadmap for Photovoltaic,” no. March. p. [Available Online], 2018.

[6] “www.pveducation.org/pvcdrom/solar-cell-structure.” .

[7] A. Richter, F. Werner, A. Cuevas, J. Schmidt, and S. W. Glunz, “Improved parameterization of Auger recombination in silicon,” in *Energy Procedia*, 2012.

[8] “www.pveducation.org/pvcdrom/surface-recombination.” .

[9] “www.azonano.com.”

[10] “www.avem.org.” .

[11] “www.semilab.com.” .

[12] “www.kelvinprobe.com.” .

[13] E. Fefer, Y. Shapira, and I. Balberg, “Direct determination of the band-gap states in hydrogenated amorphous silicon using surface photovoltage spectroscopy,” *Appl. Phys. Lett.*, vol. 67, p. 371, 1995.

[14] S. Olibet, E. Vallat-Sauvain, and C. Ballif, “Model for a-Si:H/c-Si interface recombination based on the amphoteric nature of silicon dangling bonds,” *Phys. Rev. B*, vol. 76, p. 035326, 2007.

[15] C. Sun, F. E. Rougieux, J. Degoulange, R. Einhaus, and D. Macdonald, “Reassessment of the recombination properties of aluminium–oxygen complexes in n- and p-type Czochralski-grown silicon,” *Phys. Status Solidi*, vol. 10, pp. 2079–2084, 2016.

[16] B. B. Paudyal, K. R. McIntosh, D. H. Macdonald, and G. Coletti, “Temperature dependent carrier lifetime studies of Mo in crystalline silicon,” *J. Appl. Phys.*, vol. 107, p. 054511, 2010.

[17] S. Rein, *Lifetime Spectroscopy: A Method for Defect Characterization in Silicon for Photovoltaic Applications*. Berlin: Springer, 2005.

[18] S. Bernardini, T. U. Naerland, A. L. Blum, G. Coletti, and M. I. Bertoni, “Unraveling bulk defects in high-quality c-Si material via TIDLS,” *Prog. Photovoltaics Res. Appl.*, vol. 25, pp. 209–217, 2017.

[19] A. Richter, S. W. Glunz, F. Werner, J. Schmidt, and A. Cuevas, “Improved quantitative description of Auger recombination in crystalline silicon,” *Phys. Rev. B*, vol. 86, p. 165202, 2012.

[20] “www.worldometers.info/world-population/.” .

[21] “http://www.un.org/en/development/desa/news/population/2015-report.html.” .

[22] United Nations, “Framework Convention on Climate Change,” Paris, 2015.

[23] D. M. Powell, M. T. Winkler, H. J. Choi, C. B. Simmons, D. B. Needleman, and T. Buonassisi, “Crystalline silicon photovoltaics: A cost analysis framework for determining technology pathways to reach baseload electricity costs,” *Energy Environ. Sci.*, vol. 5, no. 3, pp. 5874–5883, 2012.

[24] Fraunhofer Institute, “Photovoltaics Report,” 2017.

[25] D. M. Chapin, C. S. Fuller, and G. L. Pearson, “A new silicon p-n junction photocell for converting solar radiation into electrical power,” *J. Appl. Phys.*, vol. 25, no. 5, pp. 676–677, 1954.

[26] C. E. Chan *et al.*, “Rapid Stabilization of High-Performance Multicrystalline P-type Silicon PERC Cells,” *IEEE J. Photovoltaics*, vol. 6, no. 6, pp. 1473–1479, 2016.

[27] K. Yoshikawa *et al.*, “Exceeding conversion efficiency of 26% by heterojunction interdigitated back contact solar cell with thin film Si technology,” *Sol. Energy Mater. Sol. Cells*, vol. 173, pp. 37–42, 2017.

[28] K. Yoshikawa *et al.*, “Silicon heterojunction solar cell with interdigitated back contacts for a photoconversion efficiency over 26%,” *Nat. Energy*, vol. 2, p. 17032, 2017.

[29] U. S. D. of Energy, “The SunShot Initiative’s 2030 Goal: 3¢ per Kilowatt Hour for Solar Electricity.” pp. 18–20, 2016.

[30] S. Kurtz *et al.*, “Evaluation of high-temperature exposure of photovoltaic modules,” *Prog. Photovoltaics Res. Appl.*, vol. 19, no. 8, pp. 954–965, 2011.

[31] S. De Wolf, A. Descoeudres, Z. C. Holman, and C. Ballif, “High-efficiency Silicon Heterojunction Solar Cells: A Review,” *Green*, vol. 2, no. 1, pp. 7–24, 2012.

[32] T. Mishima, M. Taguchi, H. Sakata, and E. Maruyama, “Development status of high-efficiency HIT solar cells,” *Sol. Energy Mater. Sol. Cells*, vol. 95, pp. 18–21, 2011.

[33] J. Peter Seif *et al.*, “Amorphous silicon oxide window layers for high-efficiency silicon heterojunction solar cells,” *J. Appl. Phys.*, vol. 115, no. 2, 2014.

[34] D. D. Smith *et al.*, “Generation III high efficiency lower cost technology: Transition to

full scale manufacturing," in *Proceedings of the 38th IEEE Photovoltaic Specialists Conference*, 2012, pp. 1594–1597.

[35] D. C. Jordan, T. J. Silverman, J. H. Wohlgemuth, S. R. Kurtz, and K. T. VanSant, "Photovoltaic failure and degradation modes," *Prog. Photovoltaics Res. Appl.*, vol. 25, pp. 318–326, 2017.

[36] W. Shockley and W. T. Read, "Statistics of the Recombinations of Holes and Electrons," *Phys. Rev. Vol.*, vol. 87, pp. 835–842, 1952.

[37] R. N. Hall, "Electron-hole recombination in germanium," *Phys. Rev.*, vol. 87, p. 387, 1952.

[38] M. A. Green, "Intrinsic concentration, effective densities of states, and effective mass in silicon," *J. Appl. Phys.*, vol. 67, no. 6, pp. 2944–2954, 1990.

[39] P. P. Altermatt, "Models for numerical device simulations of crystalline silicon solar cells - A review," *J. Comput. Electron.*, vol. 10, pp. 314–330, 2011.

[40] M. J. Stocks, A. S. Cuevas, and A. W. Blakers, "Minority carrier lifetimes of multicrystalline silicon during solar cells processing," in *Proceedings of the 14th EUPVSEC*, 1997.

[41] C. Leguijt *et al.*, "Low temperature surface passivation for silicon solar cells," *Sol. Energy Mater. Sol. Cells*, vol. 40, pp. 297–345, 1996.

[42] R. Hezel and K. Jaeger, "Low-Temperature Surface Passivation of Silicon for Solar Cells," *J. Electrochem. Soc*, vol. 136, no. 2, pp. 518–523, 1989.

[43] J. I. Pankove and M. L. Tarng, "Amorphous silicon as a passivant for crystalline silicon," *Appl. Phys. Lett.*, vol. 34, p. 156, 1979.

[44] M. Tanaka *et al.*, "Development of New a-Si C-Si Heterojunction Solar-Cells - Acj-Hit (Artificially Constructed Junction-Heterojunction With Intrinsic Thin-Layer)," *Jpn. J. Appl. Phys.*, vol. 31, no. 11, pp. 3518–3522, 1992.

[45] C. Battaglia, A. Cuevas, and S. De Wolf, "High-efficiency crystalline silicon solar cells: status and perspectives," *Energy Environ. Sci.*, vol. 9, pp. 1552–1576, 2016.

[46] A. G. Aberle, M. B. Boreland, B. Hoex, and T. Mueller, "Industrial silicon wafer solar cells-status and trendsIndustrial silicon wafer solar cells-status and trends," *Green*, vol. 2, pp. 135–148, 2012.

[47] A. Goodrich *et al.*, "A wafer-based monocrystalline silicon photovoltaics road map: Utilizing known technology improvement opportunities for further reductions in manufacturing costs," *Sol. Energy Mater. Sol. Cells*, vol. 114, pp. 110–135, 2013.

[48] H. Mäckel and R. Lüdemann, "Detailed study of the composition of hydrogenated SiNx layers for high-quality silicon surface passivation," *J. Appl. Phys.*, vol. 92, no. 5, pp. 2602–2609, 2002.

[49] A. G. Aberle, "Overview on SiN surface passivation of crystalline silicon solar cells," *Sol. Energy Mater. Sol. Cells*, vol. 65, pp. 239–248, 2001.

[50] R. S. Bonilla, B. Hoex, P. Hamer, and P. R. Wilshaw, "Dielectric surface passivation for silicon solar cells: A review," *Phys. status solidi*, vol. 214, p. 1700293, 2017.

[51] P. Saint-Cast, D. Kania, M. Hofmann, J. Benick, J. Rentsch, and R. Preu, "Very low surface recombination velocity on p-type c-Si by high-rate plasma-deposited aluminum oxide," *Appl. Phys. Lett.*, vol. 95, no. 15, p. 151502, 2009.

[52] J. Schmidt, A. Merkle, R. Brendel, B. Hoex, M. C. M. Van De Sanden, and W. M. M.

Kessels, “Surface passivation of high-efficiency silicon solar cells by atomic-layer-deposited Al2O3,” *Prog. Photovoltaics Res. Appl.*, vol. 16, pp. 461–466, 2008.

[53] J. Benick, B. Hoex, M. C. M. Van De Sanden, W. M. M. Kessels, O. Schultz, and S. W. Glunz, “High efficiency n-type Si solar cells on Al2O3-passivated boron emitters,” *Appl. Phys. Lett.*, vol. 92, p. 253504, 2008.

[54] T. Dullweber and J. Schmidt, “Industrial Silicon Solar Cells Applying the Passivated Emitter and Rear Cell (PERC) Concept-A Review,” *IEEE J. Photovoltaics*, vol. 6, pp. 1366–1381, 2016.

[55] S. Duttagupta, “Advanced Surface Passivation of Crystalline Silicon for Solar Cell Applications,” National University of Singapore, 2014.

[56] D. Macdonald and L. J. Geerligs, “Recombination activity of interstitial iron and other transition metal point defects in p- and n-type crystalline silicon,” *Appl. Phys. Lett.*, 2004.

[57] S. Diez, S. Rein, T. Roth, and S. W. Glunz, “Cobalt related defect levels in silicon analyzed by temperature- and injection-dependent lifetime spectroscopy,” *J. Appl. Phys.*, 2007.

[58] B. B. Paudyal, K. R. Mcintosh, and D. H. Macdonald, “Temperature dependent carrier lifetime studies on Ti-doped multicrystalline silicon,” *J. Appl. Phys.*, vol. 105, p. 124510, 2009.

[59] R. A. Sinton and A. Cuevas, “Contactless determination of current–voltage characteristics and minority- carrier lifetimes in semiconductors from quasi- steady- state photoconductance data,” *Appl. Phys. Lett.*, vol. 69, p. 2510, 1996.

[60] M. Wilson, “COCOS (corona oxide characterization of semiconductor) non-contact metrology for gate dielectrics,” *AIP Conf. Proc.*, vol. 550, pp. 220–225, 2001.

[61] P. Edelman *et al.*, “Non-contact charge-voltage method for dielectric characterization on small test areas of IC product wafers,” *Mater. Sci. Semicond. Process.*, vol. 9, no. 1–3, pp. 252–256, 2006.

[62] H. Li *et al.*, “Determination of the Interface States in Amorphous/Crystalline Silicon Using Surface Photovoltage Spectroscopy,” *IEEE Electron Device Lett.*, vol. 34, no. 9, pp. 1079–1081, 2013.

[63] E. Yablonovitch, D. L. Allara, C. C. Chang, T. Gmitter, and T. B. Bright, “Unusually low surface-recombination velocity on silicon and germanium surfaces,” *Phys. Rev. Lett.*, vol. 57, pp. 249–252, 1986.

[64] A. B. Sproul, “Dimensionless solution of the equation describing the effect of surface recombination on carrier decay in semiconductors,” *J. Appl. Phys.*, vol. 76, no. 5, pp. 2851–2854, 1994.

[65] J. P. Seif, G. Krishnamani, B. Demaurex, C. Ballif, and S. De Wolf, “Amorphous/Crystalline Silicon Interface Passivation: Ambient-Temperature Dependence and Implications for Solar Cell Performance,” *IEEE J. Photovoltaics*, vol. 5, pp. 718–724, 2015.

[66] S. Y. Herasimenka, C. J. Tracy, V. Sharma, N. Vulic, W. J. Dauksher, and S. G. Bowden, “Surface passivation of n-type c-Si wafers by a-Si/SiO 2 /SiN x stack with <1 cm/s effective surface recombination velocity,” *Appl. Phys. Lett.*, vol. 103, p. 183903, 2013.

[67] L. Zhao, C. L. Zhou, H. L. Li, H. W. Diao, and W. J. Wang, “Design optimization of bifacial HIT solar cells on p-type silicon substrates by simulation,” *Sol. Energy Mater. Sol. Cells*, vol. 92, no. 6, pp. 673–681, 2008.

[68] G. Courtois, B. Bruneau, I. P. Sobkowicz, A. Salomon, and P. Roca Cabarrocas, “Carrier Lifetime Measurements by Photoconductance at Low Temperature on Passivated Crystalline Silicon Wafers,” *MRS Proc.*, vol. 1536, pp. 119–125, 2013.

[69] R. A. Sinton, A. L. Blum, and J. S. Swirhun, “Overview and Latest Developments in Photoconductance Lifetime Measurements in Silicon,” *Solid State Phenom.*, vol. 205–206, pp. 103–109, 2014.

[70] J. Hubin, A. V. Shah, and E. Sauvain, “Effects of dangling bonds on the recombination function in amorphous semiconductors,” *Philos. Mag. Lett.*, vol. 66, no. 3, pp. 115–125, 1992.

[71] S. M. Sze, *Semiconductor Devices: Physics and Technology*. New York: Wiley, 2001.

[72] J. Hubin, A. V. Shah, E. Sauvain, and P. Pipoz, “Consistency between experimental data for ambipolar diffusion length and for photoconductivity when incorporated into the ‘“standard”’ defect model for a-Si:H,” *J. Appl. Phys.*, vol. 78, no. 10, pp. 6050–6059, 1995.

[73] R. Meaudre and M. Meaudre, “Method for the determination of the capture cross sections of electrons from space-charge-limited conduction in the dark and under illumination in amorphous semiconductors,” *Appl. Phys. Lett.*, vol. 85, no. 2, pp. 245–247, 2004.

[74] International Technology Roadmap for Photovoltaic (ITRPV) 8th ed., “International

Technology Roadmap for Photovoltaic," no. September. p. [Available Online], 2017.

[75] C. R. Staebler, D.L. and Wronski, "Reversible conductivity changes in discharge-produced amorphous Si," *Appl. Phys. Lett.*, vol. 31, no. 1977, pp. 292–294, 1977.

[76] S. De Wolf, B. Demaurex, A. Descoeudres, and C. Ballif, "Very fast light-induced degradation of a-Si:H/c-Si(100) interfaces," *Phys. Rev. B*, vol. 83, p. 233301, 2011.

[77] P. Mahtani, R. Varache, B. Jovet, C. Longeaud, J.-P. Kleider, and N. P. Kherani, "Light induced changes in the amorphous—crystalline silicon heterointerface," *J. Appl. Phys.*, vol. 114, no. 12, p. 124503, 2013.

[78] R. Vasudevan, I. Poli, D. Deligiannis, M. Zeman, and A. H. M. Smets, "Light-Induced Effects on the a-Si:H/c-Si Heterointerface," *IEEE J. Photovoltaics*, vol. 7, pp. 656–664, 2017.

[79] R. Vasudevan, I. Poli, D. Deligiannis, M. Zeman, and A. H. M. Smets, "Temperature dependency of the silicon heterojunction lifetime model based on the amphoteric nature of dangling bonds," *AIP Adv.*, vol. 6, p. 115118, 2016.

[80] M. Stutzmann, W. B. Jackson, and C. C. Tsai, "Light-induced metastable defects in hydrogenated amorphous silicon: A systematic study," *Phys. Rev. B*, vol. 32, no. 1, pp. 23–47, 1985.

[81] I. Hirabayashi, K. Morigaki, and S. Nitta, "New evidence for defect creation by high optical excitation in glow discharge amorphous silicon," *Jpn. J. Appl. Phys.*, vol. 19, no. 7, pp. L357–L360, 1980.

[82] H. Dersch, J. Stuke, and J. Beichler, "Light-induced dangling bonds in hydrogenated amorphous silicon," *Appl. Phys. Lett.*, vol. 38, no. 6, pp. 456–458, 1981.

[83] D. E. Carlson, “Hydrogenated microvoids and light-induced degradation of amorphous-silicon solar cells,” *Appl. Phys. A Solids Surfaces*, vol. 41, no. 4, pp. 305–309, 1986.

[84] E. Bhattacharya and A. H. Mahan, “Microstructure and the light-induced metastability in hydrogenated amorphous silicon,” *Appl. Phys. Lett.*, vol. 52, no. 19, pp. 1587–1589, 1988.

[85] D. C. Jordan, J. H. Wohlgemuth, and S. R. Kurtz, “Technology and climate trends in pv module degradation,” *27th Eur. Photovolt. Sol. Energy Conf. Exhib.*, no. October, pp. 3118–3124, 2012.

[86] D. C. Jordan *et al.*, “Silicon Heterojunction System Field Performance,” *IEEE J. Photovoltaics*, vol. 8, no. 1, pp. 177–182, 2017.

[87] D. C. Jordan, T. J. Silverman, B. Sekulic, and S. R. Kurtz, “PV degradation curves: non-linearities and failure modes,” *Prog. Photovoltaics Res. Appl.*, vol. 25, no. 7, pp. 583–591, 2017.

[88] R. A. Sinton and A. Cuevas, “A Quasi-Steady-State Open-Circuit Voltage Method for Solar Cell Characterization,” in *16th European Photovoltaic Solar Energy Conference*, 2000.

[89] L. C. Andreani, A. Bozzola, and M. Liscidini, “Light trapping in thin-film solar cells: towards the Lambertian limit,” in *Proceedings of SPIE 8438*, 2012, p. 84380C.

[90] H. Plagwitz, B. Terheiden, and R. Brendel, “Staebler-Wronski-like formation of defects at the amorphous-silicon- crystalline silicon interface during illumination,” *J. Appl. Phys.*, vol. 103, no. 9, p. 094506, 2008.

[91] T. F. Schulze, H. N. Beushausen, C. Leendertz, A. Dobrich, B. Rech, and L. Korte, "Interplay of amorphous silicon disorder and hydrogen content with interface defects in amorphous/crystalline silicon heterojunctions," *Appl. Phys. Lett.*, vol. 96, no. 25, p. 252102, 2010.

[92] S. De Wolf, C. Ballif, and M. Kondo, "Kinetics of a-Si:H bulk defect and a-Si:H/c-Si interface-state reduction," *Phys. Rev. B - Condens. Matter Mater. Phys.*, vol. 85, p. 113302, 2012.

[93] X. Cheng, E. S. Marstein, C. C. You, H. Haug, and M. Di Sabatino, "Temporal stability of a-Si : H and a-SiN x : H on crystalline silicon Temporal stability of a-Si:H and a-SiNx:H on crystalline silicon wafers," *Energy Procedia*, vol. 124, pp. 275–281, 2017.

[94] M. A. Green, "Solar cell fill factors: General graph and empirical expressions," *Solid State Electron.*, vol. 24, no. 8, pp. 788–789, 1981.

[95] D. C. Jordan, B. Sekulic, B. Marion, and S. R. Kurtz, "Performance and Aging of a 20-Year-Old Silicon PV System," *IEEE J. Photovoltaics*, vol. 5, no. 3, pp. 744–751, 2015.

[96] C. Longeaud, J. A. Schmidt, and J. P. Kleider, "Determination of semiconductor band gap state parameters from photoconductivity measurements. I. Theoretical developments," *Phys. Rev. B - Condens. Matter Mater. Phys.*, vol. 73, p. 235317, 2006.

[97] A. Eray, G. Nobile, and F. Palma, "Evaluation of the density of states parameters of a-Si:H by AC photoconductivity measurements and numerical simulation," *Mater. Sci.*

*Eng. B Solid-State Mater. Adv. Technol.*, vol. 102, no. 1–3, pp. 398–402, 2003.

[98] S. De Wolf, S. Olibet, and C. Ballif, "Stretched-exponential a -Si: H / c -Si interface recombination decay," *Appl. Phys. Lett.*, vol. 93, p. 032101, 2008.

[99] "www.meyerburger.com/jp/en." .

[100] S. Dauwe, J. Schmidt, A. Metz, and R. Hezel, "Fixed charge density in silicon nitride films on crystalline silicon surfaces under illumination," in *Proceedings of the 29th IEEE Photovoltaic Specialists Conference*, 2002, pp. 162–165.

[101] J. Schmidt, J. D. Moschner, J. Henze, S. Dauwe, and R. Hezel, "Recent progress in the surface passivation of silicon solar cells using silicon nitride," in *19th European Solar Energy Conference*, 2004, pp. 391–396.

[102] S. Steingrube, P. P. Altermatt, D. S. Steingrube, J. Schmidt, and R. Brendel, "Interpretation of recombination at c-Si/SiNx interfaces by surface damage," *J. Appl. Phys.*, vol. 108, no. 1, p. 014506, 2010.

[103] S. Duttagupta, F. Lin, M. Wilson, M. B. Boreland, B. Hoex, and A. G. Aberle, "Extremely low surface recombination velocities on low-resistivities n-type and p-type crystalline silicon using dynamically deposited remote plasma silicon nitride films," *Prog. Photovoltaics Res. Appl.*, vol. 22, pp. 641–647, 2014.

[104] R. B. M. Girisch, R. P. Mertens, and R. F. De Keersmaecker, "Determination of Si-SiO2 Interface Recombination Parameters Using a Gate-Controlled Point-Junction Diode Under Illumination," *IEEE Trans. Electron Devices*, vol. 35, pp. 203–222, 1988.

[105] R. S. Bonilla and P. R. Wilshaw, "On the c-Si/SiO2 interface recombination

parameters from photo-conductance decay measurements," *J. Appl. Phys.*, vol. 121, p. 135301, 2017.

[106] A. G. Aberle, S. Glunz, and W. Warta, "Impact of illumination level and oxide parameters on Shockley-Read-Hall recombination at the Si-SiO2 interface," *J. Appl. Phys.*, vol. 71, pp. 4422–4431, 1992.

[107] Y. Y. Chen *et al.*, "Field-effect passivation and degradation analyzed with photoconductance decay measurements," *Appl. Phys. Lett.*, vol. 104, p. 193504, 2014.

[108] D. E. Kotecki and J. D. Chapple-Sokol, "Hydrogen incorporation in silicon nitride films deposited by remote electron-cyclotron-resonance chemical vapor deposition," *J. Appl. Phys.*, vol. 77, no. 3, pp. 1284–1293, 1995.

[109] M. J. Kerr and A. Cuevas, "Recombination at the interface between silicon and stoichiometric plasma silicon nitride," *Semicond. Sci. Technol.*, vol. 17, no. 1702, pp. 166–172, 2002.

[110] Z. Hameiri and F. J. Ma, "The impact of surface damage region and edge recombination on the effective lifetime of silicon wafers at low illumination conditions," *J. Appl. Phys.*, vol. 117, p. 085705, 2015.

[111] P. P. Altermatt, G. Heiser, and M. A. Green, "Numerical quantification and minimization of perimeter losses in high-efficiency silicon solar cells," *Prog. Photovoltaics Res. Appl.*, vol. 4, no. 5, pp. 355–367, 1996.

[112] J. Schmidt and A. G. Aberle, "Carrier recombination at silicon-silicon nitride interfaces fabricated by plasma-enhanced chemical vapor deposition," *J. Appl. Phys.*, vol. 85, pp. 3626–3633, 1999.

[113] J. Schmidt, F. M. Schuurmans, W. C. Sinke, S. W. Glunz, and A. G. Aberle, "Observation of multiple defect states at silicon-silicon nitride interfaces fabricated by low-frequency plasma-enhanced chemical vapor deposition," *Appl. Phys. Lett.*, vol. 71, no. 2, pp. 252–254, 1997.

[114] Y. Wan, K. McIntosh, A. Thomson, and A. Cuevas, "Low surface recombination velocity by low-absorption silicon nitride on c-Si," *IEEE J. Photovoltaics*, vol. 3, no. 1, pp. 554–559, 2013.

[115] W. Walukiewicz, "Mechanism of Schottky barrier formation: The role of amphoteric native defects," *J. Vac. Sci. Technol. B Microelectron. Nanom. Struct.*, vol. 5, no. 4, p. 1062, 1987.

[116] H. Deuling, E. Klausmann, and A. Goetzberger, "Interface States in Si-SiO2 Interfaces," *Solid. State. Electron.*, vol. 15, no. 3, pp. 559–571, 1972.

[117] P. V. Gray and D. M. Brown, "Density of SiO2-Si interface states," *Appl. Phys. Lett.*, vol. 8, no. 2, pp. 31–33, 1966.

[118] H. Sakaki, K. Hoh, and T. Sugano, "Determination of Interface-State Density," *IEEE Trans. Electron Devices*, vol. 17, pp. 892–896, 1970.

[119] A. Cuevas, "The recombination parameter J0," *Energy Procedia*, vol. 55, pp. 53–62, 2014.

[120] H. T. Nguyen, S. C. Baker-Finch, and D. Macdonald, "Temperature dependence of the radiative recombination coefficient in crystalline silicon from spectral photoluminescence," vol. 104, p. 112105, 2014.

[121] T. Trupke *et al.*, "Temperature dependence of the radiative recombination coefficient

of intrinsic crystalline silicon," *J. Appl. Phys.*, vol. 94, no. 8, pp. 4930–4937, 2003.

[122] S. Wang and D. MacDonald, "Temperature dependence of Auger recombination in highly injected crystalline silicon," *J. Appl. Phys.*, vol. 112, p. 113708, 2012.

[123] K. Graff, *Metal Impurities in Silicon-Device Fabrication*. Berlin: Springer, 1999.

[124] A. C. Wang and C. T. Sah, "Complete electrical characterization of recombination properties of titanium in silicon," *J. Appl. Phys.*, vol. 56, p. 1021, 1984.

[125] A. Fazzio, M. J. Caldas, and A. Zunger, "Electronic structure of copper, silver, and gold impurities in silicon," *Phys. Rev. B*, vol. 32, no. 2, pp. 934–954, 1985.

[126] D. H. Macdonald, W. Brendle, A. Cuevas, and A. A. Istratov, "Injection-dependent lifetime studies of copper precipitates in silicon," in *Proceedings of the 12th Workshop Crystalline Silicon Solar Cell Materials and Processes*, 2002.

[127] T. Roth *et al.*, "Electronic properties and dopant pairing behavior of manganese in boron-doped silicon," *J. Appl. Phys.*, vol. 102, p. 103716, 2007.

[128] Y. K. Kwon, T. Ishikawa, and H. Kuwano, "Properties of platinum- associated deep levels in silicon," *Appl. Phys. Lett.*, vol. 61, p. 1055, 1987.

[129] K. Mishra, "Identification of Cr in p- type silicon using the minority carrier lifetime measurement by the surface photovoltage method," *Appl. Phys. Lett.*, vol. 66, p. 3281, 1996.

[130] A. L. Blum *et al.*, "Interlaboratory study of eddy-current measurement of excess-carrier recombination lifetime," *IEEE J. Photovoltaics*, vol. 4, pp. 525–531, 2014.

[131] J. Schmidt, "Temperature-and injection-dependent lifetime spectroscopy for the characterization of defect centers in semiconductors," *Appl. Phys. Lett.*, vol. 82, p.

2178, 2003.

[132] P. Rosenits, T. Roth, S. W. Glunz, and S. Beljakowa, “Determining the defect parameters of the deep aluminum-related defect center in silicon,” *Appl. Phys. Lett.*, 2007.

[133] T. U. Naerland, S. Bernardini, M. S. Wiig, and M. I. Bertoni, “Is It Possible to Unambiguously Assess the Presence of Two Defects by Temperature-and Injection-Dependent Lifetime Spectroscopy?,” *IEEE J. Photovoltaics*, vol. 8, no. 2, pp. 465–472, 2018.

[134] M. J. Kerr, A. Cuevas, and P. Campbell, “Limiting efficiency of crystalline silicon solar cells due to Coulomb-enhanced Auger recombination,” *Prog. Photovoltaics Res. Appl.*, vol. 11, pp. 97–104, 2003.

[135] A. Richter, M. Hermle, and S. W. Glunz, “Reassessment of the limiting efficiency for crystalline silicon solar cells,” *IEEE J. Photovoltaics*, vol. 3, pp. 1184–1191, 2013.

[136] M. Taguchi *et al.*, “HITTM cells—High- Efficiency Crystalline Si Cells with Novel Structure,” *Prog. Photovoltaics Res. Appl.*, vol. 8, pp. 503–513, 2000.

[137] S. Y. Herasimenka, C. J. Tracy, V. Sharma, N. Vulic, W. J. Dauksher, and S. G. Bowden, “Surface passivation of n-type c-Si wafers by a-Si/SiO2/SiN x stack with <1 cm/s effective surface recombination velocity,” *Appl. Phys. Lett.*, vol. 103, p. 183903, 2013.

[138] K. Masuko *et al.*, “Achievement of More Than 25% Conversion Efficiency With Crystalline Silicon Heterojunction Solar Cell,” *IEEE J. Photovoltaics*, vol. 4, pp. 1433–1435, 2014.

[139] M. A. Green, “Limits on the Open-circuit Voltage and Efficiency of Silicon Solar Cells Imposed by Intrinsic Auger Processes,” *IEEE Trans. Electron Devices*, vol. 31, pp. 671–678, 1984.

[140] T. Tiedje, E. Yablonovitch, G. D. Cody, and B. G. Brooks 71, “Limiting Efficiency of Silicon Solar Cells,” *IEEE Trans. Electron Devices*, vol. 31, no. 5, pp. 711–716, 1984.

[141] A. Augusto, S. Y. Herasimenka, R. R. King, S. G. Bowden, and C. Honsberg, “Analysis of the recombination mechanisms of a silicon solar cell with low bandgap-voltage offset,” *J. Appl. Phys.*, vol. 121, p. 205704, 2017.

[142] A. Beattie and P. Landsberg, “Auger Effect in Semiconductor,” *Proc. R. Soc. London, Ser. A*, vol. 249, no. 1256, pp. 16–29, 1958.

[143] L. Huldt, “Band- to- band Auger recombination in indirect gap semiconductors,” *Phys. Status Solidi Appl. Mater. Sci.*, vol. 8, p. 173, 1971.

[144] A. Haug, “Carrier density dependence of Auger recombination,” *Solid. State. Electron.*, vol. 21, no. 11–12, pp. 1281–1284, 1978.

[145] P. T. Landsberg, “The band-band Auger effect in semiconductors,” *Solid State Electron.*, vol. 30, no. 11, pp. 1107–1115, 1987.

[146] K. G. Svantesson and N. G. Nilsson, “The temperature dependence of the Auger recombination coefficient of undoped silicon,” *J. Phys. C Solid State Phys*, vol. 12, pp. 5111–5120, 1979.

[147] E. Yablonovitch and T. Gmitter, “Auger recombination in silicon at low carrier densities,” *Appl. Phys. Lett.*, vol. 49, p. 587, 1986.

[148] M. S. Tyagi and R. Van Overstraeten, “Minority carrier recombination in heavily-

doped silicon," *Solid State Electron.*, vol. 26, no. 6, pp. 577–597, 1983.

[149] P. P. Altermatt, J. Schmidt, G. Heiser, and A. G. Aberle, "Assessment and parameterisation of Coulomb-enhanced Auger recombination coefficients in lowly injected crystalline silicon," *J. Appl. Phys.*, vol. 82, no. 10, p. 4938, 1997.

[150] L. Huldt, N. G. Nilsson, and K. G. Svantesson, "The temperature dependence of band-to-band Auger recombination in silicon," *Appl. Phys. Lett.*, vol. 35, no. 10, pp. 776–777, 1979.

[151] M. J. Kerr and A. Cuevas, "General parameterization of Auger recombination in crystalline silicon," *J. Appl. Phys.*, vol. 88, p. 1494, 2002.

[152] A. Hangleiter, "Nonradiative recombination via deep impurity levels in semiconductors: The excitonic Auger mechanism," *Phys. Rev. B*, vol. 37, no. 5, pp. 2594–2604, 1988.

[153] A. Hangleiter and R. Hacker, "Enhancement of band-to-band Auger recombination by electron-hole correlations," *Phys. Rev. Lett.*, vol. 65, no. 2, pp. 215–218, 1990.

[154] K. R. Mcintosh and C. B. Honsberg, "The influence of edge recombination on a solar cell's I-V curve," in *Proceedings of the 16th EUPVSEC*, 2000, no. August, pp. 1651–1654.

[155] R. Kühn, P. Fath, and E. Bücher, "Effects of pn-junctions bordering on surfaces investigated by means of 2D-modeling," *Conf. Rec. IEEE Photovolt. Spec. Conf.*, pp. 116–119, 2000.

[156] M. J. Kerr, "Ph.D. Thesis," The Australian National University, 2002.

[157] P. P. Altermatt, F. Geelhaar, T. Trupke, X. Dai, A. Neisser, and E. Daub, "Injection

dependence of spontaneous radiative recombination in crystalline silicon: Experimental verification and theoretical analysis," *Appl. Phys. Lett.*, vol. 88, p. 261901, 2006.

[158] P. P. Altermatt, F. Geelhaar, T. Trupke, X. Dai, A. Neisser, and E. Daub, "Injection dependence of spontaneous radiative recombination in c-Si: Experiment, theoretical analysis, and simulation," in *NUSOD '05 - Proceedings of the 5th International Conference on Numerical Simulation of Optoelectronic Devices*, 2005.

[159] D. B. Laks, G. F. Neumark, A. Hangleiter, and S. T. Pantelides, "Theory of interband auger recombination in n-type silicon," *Phys. Rev. Lett.*, vol. 61, no. 10, pp. 1229–1232, 1988.

[160] F. Chern, "Ph.D. Thesis," The Australian National University, 2012.

[161] A. Descoeudres, Z. C. Holman, L. Barraud, S. Morel, S. De Wolf, and C. Ballif, "21% Efficient Silicon Heterojunction Solar Cells on n- and p-Type Wafers Compared," *IEEE J. Photovoltaics*, vol. 3, pp. 83–89, 2013.

[162] J. Haschke *et al.*, "The impact of silicon solar cell architecture and cell interconnection on energy yield in hot & sunny climates," *Energy Environ. Sci.*, vol. 10, no. 5, pp. 1196–1206, 2017.

[163] Y. Wan, K. R. McIntosh, A. F. Thomson, and A. Cuevas, "Low Surface Recombination Velocity by Low-Absorption Silicon Nitride on c-Si," *IEEE J. Photovoltaics*, vol. 3, no. 1, pp. 554–559, 2013.

[164] T. Niewelt, W. Kwapil, M. Selinger, A. Richter, and C. Martin, "Stability of effective lifetime of float-zone silicon wafers with AlOx surface passivation schemes under

illumination at elevated temperature," *Energy Procedia*, vol. 124, pp. 146–151, 2017.

[165] B. A. Veith-Wolf and J. Schmidt, "Unexpectedly High Minority-Carrier Lifetimes Exceeding 20 ms Measured on 1.4-Ω cm n -Type Silicon Wafers," *Phys. status solidi - Rapid Res. Lett.*, vol. 11, p. 1700235, 2017.

[166] B. Steinhauser, J. Polzin, F. Feldmann, M. Hermle, and S. W. Glunz, "Excellent Surface Passivation Quality on Crystalline Silicon Using Industrial-Scale Direct-Plasma TOPCon Deposition Technology," *Sol. RRL*, vol. 1800068, pp. 1–5, 2018.

[167] B. A. Veith-Wolf, S. Schäfer, R. Brendel, and J. Schmidt, "Reassessment of intrinsic lifetime limit in n -type crystalline silicon and implication on maximum solar cell efficiency," *Sol. Energy Mater. Sol. Cells*, vol. 186, pp. 194–199, 2018.